

NASA/CR-97-206260

W-33
076546

P. 88



Three-Centimeter Doppler Radar Observations of Wingtip-Generated Wake Vortices in Clear Air

Robert E. Marshall, Ashok Mudukutore, Vicki L. H. Wissel, and Theodore Myers

December 1997

The NASA STI Program Office ... in Profile

Since its founding, NASA has been dedicated to the advancement of aeronautics and space science. The NASA Scientific and Technical Information (STI) Program Office plays a key part in helping NASA maintain this important role.

The NASA STI Program Office is operated by Langley Research Center, the lead center for NASA's scientific and technical information. The NASA STI Program Office provides access to the NASA STI Database, the largest collection of aeronautical and space science STI in the world. The Program Office is also NASA's institutional mechanism for disseminating the results of its research and development activities. These results are published by NASA in the NASA STI Report Series, which includes the following report types:

- **TECHNICAL PUBLICATION.** Reports of completed research or a major significant phase of research that present the results of NASA programs and include extensive data or theoretical analysis. Includes compilations of significant scientific and technical data and information deemed to be of continuing reference value. NASA counter-part of peer reviewed formal professional papers, but having less stringent limitations on manuscript length and extent of graphic presentations.
- **TECHNICAL MEMORANDUM.** Scientific and technical findings that are preliminary or of specialized interest, e.g., quick release reports, working papers, and bibliographies that contain minimal annotation. Does not contain extensive analysis.
- **CONTRACTOR REPORT.** Scientific and technical findings by NASA-sponsored contractors and grantees.
- **CONFERENCE PUBLICATION.** Collected papers from scientific and technical conferences, symposia, seminars, or other meetings sponsored or co-sponsored by NASA.
- **SPECIAL PUBLICATION.** Scientific, technical, or historical information from NASA programs, projects, and missions, often concerned with subjects having substantial public interest.
- **TECHNICAL TRANSLATION.** English-language translations of foreign scientific and technical material pertinent to NASA's mission.

Specialized services that help round out the STI Program Office's diverse offerings include creating custom thesauri, building customized databases, organizing and publishing research results ... even providing videos.

For more information about the NASA STI Program Office, you can:

- Access the NASA STI Program Home Page at <http://www.sti.nasa.gov/STI-homepage.html>
- E-mail your question via the Internet to help@sti.nasa.gov
- Fax your question to the NASA Access Help Desk at (301) 621-0134
- Phone the NASA Access Help Desk at (301) 621-0390
- Write to:
NASA Access Help Desk
NASA Center for AeroSpace Information
800 Elkrige Landing Road
Linthicum Heights, MD 21090-2934

NASA /CR-97-206260



Three-Centimeter Doppler Radar Observations of Wingtip-Generated Wake Vortices in Clear Air

Robert E. Marshall, Ashok Mudukutore, and Vicki L. H. Wissel
Center for Aerospace Technology, Research Triangle Institute, Hampton, VA

and

Theodore Myers
Virginia Polytechnic Institute and State University, Blacksburg, VA

National Aeronautics and
Space Administration

Langley Research Center
Hampton, Virginia 23681-2199

Prepared for Langley Research Center
under Contract NAS1-18925

December 1997

Available from the following:

NASA Center for AeroSpace Information (CASI)
800 Elkridge Landing Road
Linthicum Heights, MD 21090-2934
(301) 621-0390

National Technical Information Service (NTIS)
5285 Port Royal Road
Springfield, VA 22161-2171
(703) 487-4650

CONTENTS

LIST OF FIGURES	iv
LIST OF TABLES	v
EXECUTIVE SUMMARY	vi
1.0 INTRODUCTION	1
2.0 description of the experiment.....	4
2.1 <u>Summary of Experimental Procedure</u>	4
2.2 <u>Radar Instrumentation</u>	6
2.2.1 The C-band Radar	6
2.2.2 The X-band Radar	7
3.0 SMOKE VIDEO ANALYSIS.....	10
3.1 <u>Smoke Video Analysis Methodology</u>	10
3.2 <u>Smoke Video Analysis Results</u>	13
4.0 METEOROLOGICAL DATA ANALYSIS.....	18
4.1 <u>Meteorological Data for Pass 44</u>	19
4.2 <u>Meteorological Data for Pass 55</u>	21
4.3 <u>Meteorological Data for Pass 97</u>	23
4.4 <u>Meteorological Data for Passes 116, 122, and 124</u>	25
4.5 <u>Meteorological Data for Pass 135</u>	27
5.0 X-BAND RADAR DATA ANALYSIS.....	29
5.1 <u>Data Analysis Procedure</u>	29
5.1.1 Estimation of Power Spectrum.....	29
5.1.2 Clutter Suppression	30
5.1.3 Noise Suppression	32
5.1.4 Moments Estimation	32
5.2 <u>Data Analysis</u>	33
5.3 <u>X-band Radar Performance Analysis</u>	33
6.0 CONCLUSIONS	38
REFERENCES.....	41
GLOSSARY	43
APPENDIX	44

LIST OF FIGURES

Figure 2–1. Experimental setup for the X-band radar wake vortex detection experiment.....	5
Figure 2–6. Schematic Diagram of X-band Doppler Radar.....	8
Figure 4–1. Characteristic decay time (Brunt-Vaisala Period) for wake vortices at 1800 UTC on January 9, 1995. (The wake was generated at 490 meters AGL.).....	19
Figure 4–2. Atmospheric humidity for wake vortices at 1800 UTC on January 9, 1995. (The wake was generated at 490 meters AGL.)	20
Figure 4–3. Cross aircraft bearing wind speed for wake vortices at 1800 UTC on January 9, 1995. (The wake was generated at 490 meters AGL.)	20
Figure 4–4. Characteristic decay time (Brunt-Vaisala Period) for wake vortices at 2000 UTC on January 9, 1995. (The wake was generated at 400 meters AGL.).....	21
Figure 4–5. Atmospheric humidity for wake vortices at 2000 UTC on January 9, 1995. (The wake was generated at 400 meters AGL.)	22
Figure 4–6. Cross aircraft bearing wind speed for wake vortices at 2000 UTC on January 9, 1995. (The wake was generated at 400 meters AGL.)	22
Figure 4–7. Characteristic decay time (Brunt-Vaisala Period) for wake vortices at 1800 UTC on January 10, 1995. (The wake was generated at 610 meters AGL.)....	23
Figure 4–8. Atmospheric humidity for wake vortices at 1800 UTC on January 10, 1995. (The wake was generated at 610 meters AGL.)	24
Figure 4–9. Cross aircraft bearing wind speed for wake vortices at 1800 UTC on January 10, 1995. (The wake was generated at 610 meters AGL.)	24
Figure 4–10. Characteristic decay time (Brunt-Vaisala Period) for wake vortices at 1600 UTC on January 11, 1995. (The wakes were generated below 500 meters where the atmosphere is near neutral.).....	25
Figure 4–11. Atmospheric humidity for wake vortices at 1600 UTC on January 11, 1995. (The wakes were generated below 500 meters AGL.)	26
Figure 4–12. Cross aircraft bearing wind speed for wake vortices at 1600 UTC on January 11, 1995. (The wakes were generated below 500 meters AGL.)	26
Figure 4–13. Characteristic decay time (Brunt-Vaisala Period) for wake vortices at 1800 UTC on January 11, 1995. (The wake was generated at 610 meters AGL.)....	27
Figure 4–14. Atmospheric humidity for wake vortices at 1800 UTC on January 11, 1995. (The wake was generated at 610 meters AGL.)	28
Figure 4–15. Cross aircraft bearing wind speed for wake vortices at 1800 UTC on January 11, 1995. (The wake was generated at 610 meters AGL.)	28
Figure 5–1. Schematic of Clutter Filtering Algorithm.....	31
Figure 5–2. Minimum Volume Reflectivity Required for Detection of Wake Vortices in Clear Air for the Wallops Island X-band Doppler Radar. ($\tau \equiv$ pulse width)....	36

LIST OF TABLES

Table 1. Previous Clear Air Radar Wake Vortex Detection Experiments	2
Table 2-1. Characteristics of the C-band Radar.....	7
Table 2-2. Characteristics of the X-band Radar	9
Table 3-1. Smoke Analysis Results for Pass 44	13
Table 3-2. Smoke Analysis Results for Pass 55	14
Table 3-3. Smoke Analysis Results for Pass 97	14
Table 3-4. Smoke Analysis Results for Pass 116	15
Table 3-5. Smoke Analysis Results for Pass 122	16
Table 3-6. Smoke Analysis Results for Pass 124	17
Table 3-7. Smoke Analysis Results for Pass 135	17
Table 5-1. Component Noise Temperatures and Gains for Wallops X-band Radar	34
Table 5-2. Correlation of Meteorological Data with Radar Parameters	37
Table A-1. Index to Figures in Appendix A	45

EXECUTIVE SUMMARY

An objective of the NASA Aircraft Vortex Separation System (AVOSS) is to increase the terminal area productivity by reducing the wake vortex separation distance imposed on aircraft landing at airports (Hinton, 1995). The purpose of AVOSS is to dynamically adjust the separation distance between aircraft by predicting the transport and decay characteristics of wake vortices generated by landing aircraft. The transport and decay characteristics of wake vortices are currently being modeled; these characteristics depend upon the meteorological conditions in proximity to the aircraft glideslopes. As part of AVOSS, the accuracy of the prediction model would be monitored in real time by remote sensors. Two remote sensors, Lidar (Light Detection And Ranging) and conventional radar, are being considered as part of the overall program to provide empirical data to validate the analytical model.

AVOSS would operate under both visible and instrument flight rules—in clear air, haze, fog, drizzle, rain and snow. Lidar is known to measure effectively under atmospheric conditions of high visibility, while radar is known to measure effectively under atmospheric conditions of limited visibility, such as heavy fog, drizzle, rain, and snow. At the time of this experiment, it was unclear how effective X-band radar would be in making quantitative measurements under clear air conditions.

Simulation studies of radar reflectivity under clear air conditions indicated that the potential existed for a conventional X-band radar to detect and locate wake vortices generated by a large aircraft transport in clear air. Therefore, a series of field experiments was conducted in January 1995 at the Wallops Flight Facility (WFF) to demonstrate, for the first time, the ability of an X-band radar at 9.33 GHz ($\lambda = 3$ cm) to locate and detect wake vortices generated by a C-130 aircraft under clear air conditions. The 9.33 GHz radar was assembled by integrating an existing nine-meter parabolic antenna reflector at the Wallops Flight Facility with the receiver / transmitter from the NASA Airborne Windshear Radar Program (Schaffner, et al, 1992).

The C-130 used in the field experiments was equipped with wingtip smoke generators to create a visual image of the wake vortices. The wake vortices were then recorded by five video cameras. A C-band radar located 500 meters to the North of the

X-band radar was used to detect wake vortices at the same time as they were being observed with the X-band system. Rawinsonde data was used to calculate vertical soundings of vortex decay time, cross aircraft bearing wind speed, and water vapor mixing ratio for the aircraft passes over the measurement range of the radars.

Despite a lengthy analysis of selected data received from the field measurements from WFF, the experiment did not show any conclusive information that the X-band radar was locating or detecting the presence of the wake vortices generated by the C-130 in clear air conditions. Yet, the C-band (6 GHz) radar was successful in detecting the presence of the C-130 wake vortices. However, it should not be concluded from this series of experiments that an X-band radar is incapable of detecting wake vortices in clear air for several reasons:

- A Doppler radar, such as the Wallops X-band Doppler radar, with a sample volume of similar size to the wake of the C-130, needs a capability of measuring radar reflectivities of approximately -135 dB m^{-1} . Under the conditions originally planned for this experiment, the X-band radar should have been able to locate the wake vortices in clear air. These plans assumed that the full radar output power of 2 kW would be used; however, due to a component failure during the field deployment, output power was only 700 W.
- The parabolic antenna used in the experiment was not designed to detect distributed targets. The combination of inadequate surface tolerance and UHF feed blockage resulted in high antenna sidelobes and signal contamination from ground clutter, which further complicated the measurements.

After the experiment was completed, the single pulse signal-to-noise ratio (SNR) for distributed targets was computed for the actual performance parameters of the X-band radar. The volume reflectivity (dB m^{-1}) was computed for three values of the transmitter pulse width that were used in the experiments. In general, after accounting for the actual instrument parameters of the X-band radar during the WFF experiment, the detection, location, and quantification of wake vortices was highly improbable.

However, the researchers obtained several “lessons learned” which will be useful in planning and executing future field experiments.

1. Although the experiment was well conceived and well planned, a “dry run” should have been conducted prior to launching the major campaign. The results from the “dry run” should have been analyzed to verify the calibration, transmitter power, and SNR of the X-band (9.3 GHz) radar.
2. Real-time processing can be invaluable in assisting the experimenters in making appropriate changes in the experiment to optimize success of the experiment. In lieu of real-time processing, intervals of time should be provided to analyze the available data in detail prior to taking the next step in the experiment.
3. In this type of experiment, automated alignment of the radar antenna is extremely important. Every attempt should be made in future experiments to ensure precise alignment of the antenna boresight in the core of the wake vortex.

This experiment was a high risk, high payoff experiment; the objective was to detect, for the first time, the presence of wake vortices in clear air with an X-band radar. In addition, the experiment was a pathfinder in predicting, in real time, the location and persistence of the wake vortices generated by the C-130, and setting the flight path of the aircraft to optimize the measurement by the X-band radar of the wake vortex core in real time. This procedure was required in order to coordinate the passes of the aircraft which would maximize the interaction of the radar pulse with the spatial and temporal evolution of the wake vortices in post-processing data analysis.

1.0 INTRODUCTION

An objective of the NASA Aircraft Vortex Separation System (AVOSS) is to increase the terminal area productivity by reducing the wake vortex separation distance imposed on aircraft landing at airports (Hinton, 1995). The purpose of AVOSS is to dynamically adjust the separation distance between aircraft by predicting the transport and decay characteristics of wake vortices generated by landing aircraft. The transport and decay characteristics of wake vortices are currently being modeled; these characteristics depend upon the meteorological conditions in proximity to the aircraft glideslopes. As part of AVOSS, the accuracy of the prediction model would be monitored in real time by remote sensors. Two remote sensors, Lidar (Light Detection And Ranging) and conventional radar, are being considered as part of the overall program to provide empirical data to validate the analytical model.

AVOSS would operate under both visible and instrument flight rules—in clear air, haze, fog, drizzle, rain and snow. Lidar is known to measure effectively under atmospheric conditions of high visibility, while radar is known to measure effectively under atmospheric conditions of limited visibility, such as heavy fog, drizzle, rain, and snow. At the time of this experiment, it was unclear how effective X-band radar would be in making quantitative measurements under clear air conditions.

There exists a high frequency cutoff for radar detection of wingtip-generated wake vortices in clear air (Marshall, et al., 1997). At the time of the experiment described in this report, this maximum frequency was known to be between 6 and 35 GHz. Prior to this experiment, three experiments were conducted to detect wingtip-generated wake vortices in clear air with radar (Chadwick et al., 1983, Gilson, 1992, Nespor, et al., 1991). Table 1 provides a description of these previous experiments. All of the radars described in Table 1 were designed for purposes other than aircraft wake detection. The results from these experiments showed that radars with wavelengths up to 5 cm (6 GHz) successfully detected wake vortices; however, the single millimeter wave radar (34 GHz; $\lambda = 0.9$ cm) failed to detect the aircraft wake.

Table 1. Previous Clear Air Radar Wake Vortex Detection Experiments

Descriptive Parameter	Experiment		
	Chadwick, et al	Gilson	Nespor, et al
Experiment Location	Stapleton, Denver	Kwajalein, RMI	White Sands, NM
Experiment Date(s)	Nov.– Dec., 1981	June, 1990	Feb., 1991
Vortex Generating Aircraft	DC-8	C-5A Learjet (not detected)	A-7
Radar Type	S-band FM-CW	VHF, UHF, L,S,C & Ka-bands pulsed Doppler	C-band pulsed Doppler
Antenna Type	Bistatic, 2.4 m parabolic reflector	parabolic reflectors	phased array
Range	100 and 600 meters	15 km	2.7 km
Look Angle	ortho-axial ¹	ortho-axial ¹	axial ortho-axial ¹ (not detected)
Wavelength(s), λ, tested	10 cm	3m, 1m, 15cm, 10cm, 5cm, 0.9cm	5 cm
Wavelength(s), λ, detected	10 cm	3m, 1m, 15cm, 10cm, 5cm	5 cm
Measured Reflectivity (dB m⁻¹)	$-144 \leq \eta \geq -122$	$-139 \leq \eta \geq -119$ (S-band) $-151 \leq \eta \geq -123$ (C-band)	$-135 \leq \eta \geq -116$
Conclusions	<ul style="list-style-type: none"> • Increased reflectivity above ambient atmosphere. • Vortex not detected until 15 seconds after aircraft 	<ul style="list-style-type: none"> • Reflectivity increases with time up to 10 km behind aircraft. • Reflectivity is flat with decreasing wavelength down to 5 cm. • Reflectivity decreases with height. 	<ul style="list-style-type: none"> • Increased reflectivity above ambient atmosphere.

¹ The term "axial," under look angle in Table 1, refers to pointing the radar along the generating aircraft bearing and observing the lingering wake. "Ortho-axial" refers to observing the wake by pointing the radar orthogonal to the generating aircraft bearing.

Simulation studies of radar reflectivity under clear air conditions indicated that the potential existed for a conventional X-band radar to detect and locate wake vortices generated by a large aircraft transport in clear air. Therefore, a series of field experiments

was conducted in January 1995 at the Wallops Flight Facility (WFF) to demonstrate, for the first time, the ability of an X-band radar at 9.33 GHz ($\lambda = 3$ cm) to locate and detect wake vortices generated by a C-130 aircraft under clear air conditions.

Section 2.0 of this report describes the experimental approach and the radar instrumentation used in the field experiments. The C-130 was equipped with wingtip smoke generators, and a visual image of the wake vortices was captured on video. Section 3.0 provides the analysis methodology and results from these videos, which were used to focus the post-processing of the X-band radar data. Section 4.0 describes the meteorological and wind speed data used to analyze vortex transport and decay during the experiments to assist in experiment execution, while Section 5.0 describes the procedure used to analyze the X-band radar data and the results of the analysis. The last section of this report presents the conclusions and “lessons learned” that were obtained as a result of conducting this set of field experiments.

2.0 DESCRIPTION OF THE EXPERIMENT

Approximately 200 passes of a C-130 aircraft over the Wallops Flight Facility took place during the X-band wake vortex detection experiment in January 1995. All of these passes were conducted in clear air. The experiment was tailored to test for detection of Bragg scatter from the turbulent intensity within the wake vortices of the C-130. The experimental equipment included meteorological instrumentation, a C-band radar, an X-band radar, and five video cameras to record experimental procedure, visualize the vortices, and to provide an independent means of locating the vortices in space.

This section of the report describes the experimental procedure and the platforms that were involved in generating experimental data. Section 2.1 provides an overall description of the experimental procedure. Section 2.2 describes the characteristics of the C-band and X-band radars used in the field tests. The characteristics for the X-band radar are described both as expected prior to the experimental tests and as the radar actually performed in the field environment. There was significant degradation in the performance of the X-band radar in the field versus the expected performance, which was a significant factor in the outcome of the experiment.

2.1 Summary of Experimental Procedure

Balloon-launched rawinsondes took observations of the vertical structure of the atmospheric parameters every two hours. The balloon site was located on the coastal side of the island, 3 km southeast of the X-band radar. The rawinsonde data provided vertical profiles of pressure, temperature, dew point, and winds, which were faxed in real time to the experiment director. The raw data were converted into vertical profiles of cross aircraft bearing wind speed, potential temperature, Brunt-Vaisala period (Sorjan, 1989), and water vapor mixing ratio, and the director used these products to define the flight path and altitude of the next C-130 pass, in order to optimize the interaction of the radar pulse with the wake vortex core. This use of meteorological sounding data was a reliable tool for defining radar scan strategies and the placement of the wake generating aircraft.

The NASA C-130 was equipped with wingtip smokers. The smoke was ingested into the wake vortices, which made the vortices optically visible for an extended period. The resulting wake with imbedded vortices was initially estimated to be 60 meters across, descending at 0.5 m sec^{-1} .

Boresight cameras were located on the C-band and X-band radar antennas to directly record what those radars were viewing at any time. On the island, Camera Station 5 and Camera Station 2 housed cameras that were aimed toward the radars and provided a wide, reverse view of the aircraft flight paths (see figure 2-1). Camera Station 4, located between the radar sites, was used to observe interesting vortex behavior; Camera 4 did not necessarily look at the portion of the vortices that the radars were viewing, and its sole purpose was observing vortex behavior.

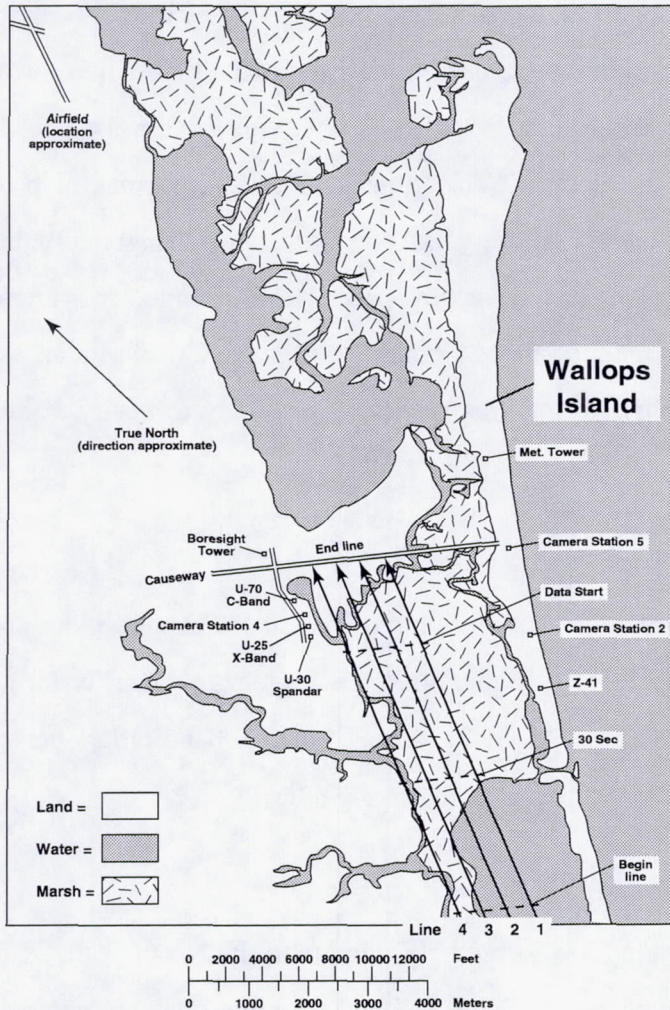


Figure 2-1. Experimental setup for the X-band radar wake vortex detection experiment.

During some of the C-130 passes, the X-band radar was manually aimed using the antenna boresight camera to align the radar with the smoke trail. This procedure was ineffective because, as researchers discovered in post-experiment analysis, the boresight camera was poorly mounted, which caused misalignment. As part of the smoke video analysis, a correction factor, consisting of a fixed offset at the beginning of each pass, was implemented to compensate for the misalignment; however, the data could not be fully corrected because of an unpredictably varying component of the error. The effect of this residual boresight error on determining the period of time during which the radar was observing the target vortices was believed to be insignificant.

The most important function of the video data provided a means for locating the vortices in space and time. Observations of the smoke marking the vortices in the views provided by Cameras 2 and 5 provided azimuth and elevation information. The boresight cameras on the two radars were used to find the exact time when a vortex was in view of a radar (a hit), while the data from Cameras 2 and 5 were used to determine the range from the radar to the vortex. This time and range information provided a means for identifying which portions of the voluminous radar data might contain a vortex detection and, hence, should be selected for post-processing. Range accuracy for the cameras was on the order of 100 meters (about a range gate for the C-band radar, and 2 or 3 range bins for the X-band radar), which was sufficient accuracy to verify vortex detections in the radar data.

2.2 Radar Instrumentation

The experimental radar equipment included a C-band radar and an X-band radar. As indicated in Table 1, the highest frequency radar to detect wake vortices prior to this experiment was at C-band (6 GHz). The C- and X-band radars performed simultaneous observations of wake vortices.

2.2.1 The C-band Radar

A C-band radar was located 500 meters to the North of the X-band at the Wallops Flight Facility (figure 2-1). Table 2-1 contains the characteristics of the C-band radar

(Mackenzie, 1997). The C-band radar contained only one range bin, and the vortices could only be seen occasionally as they drifted through the range cell.

Table 2–1. Characteristics of the C-band Radar

Parameter	Value
Frequency	5.765 GHz
Peak Power	2.2 MW
PRF	640 Hz
Range Resolution	112.5 meter
Range Gate Length	0.75 μ sec
Noise Bandwidth	4.36 MHz
Receiver Noise Floor	-100.6 dBm
Number of Range Gates	1
Data Recording Rate	10 Hz
Antenna Beamwidth	0.4 °
Antenna Diameter	8.84 meter
Antenna Gain	51 dB
Antenna First Sidelobe	-16.5 dB
Antenna Polarization	vertical
Antenna Scan Rate	2 ° sec ⁻¹
Scanning Axes	az or el
Antenna Tower Height	14.98 meter
2-way Waveguide Loss	4.9 dB

2.2.2 The X-band Radar

The purpose of the experiment described in this report was to demonstrate the existence of radar volume reflectivity in wingtip generated wake vortices at 9.33 GHz. The microwave band between 8.2 and 12.4 GHz is referred to as X-band, and the 9.33 GHz, X-band radar was the primary instrument for the Wallops Island experiment. This radar was fabricated by combining the Rockwell-Collins receiver / transmitter from the NASA Airborne Windshear Radar program (Schaffner, et al., 1992) and a ground based nine meter diameter antenna located at Wallops Island, Virginia. The Collins R/T unit and high power amplifier unit were mounted on the antenna positioner and connected to the antenna by a 25 ft. length of rectangular waveguide (WR-112). The intermediate frequency received signal from the Collins R/T unit was connected to the signal

processor, located in an electronics van at the base of the antenna positioner, by a coaxial cable (RG-214). Figure 2–6 is a schematic diagram of the X-band Doppler radar.

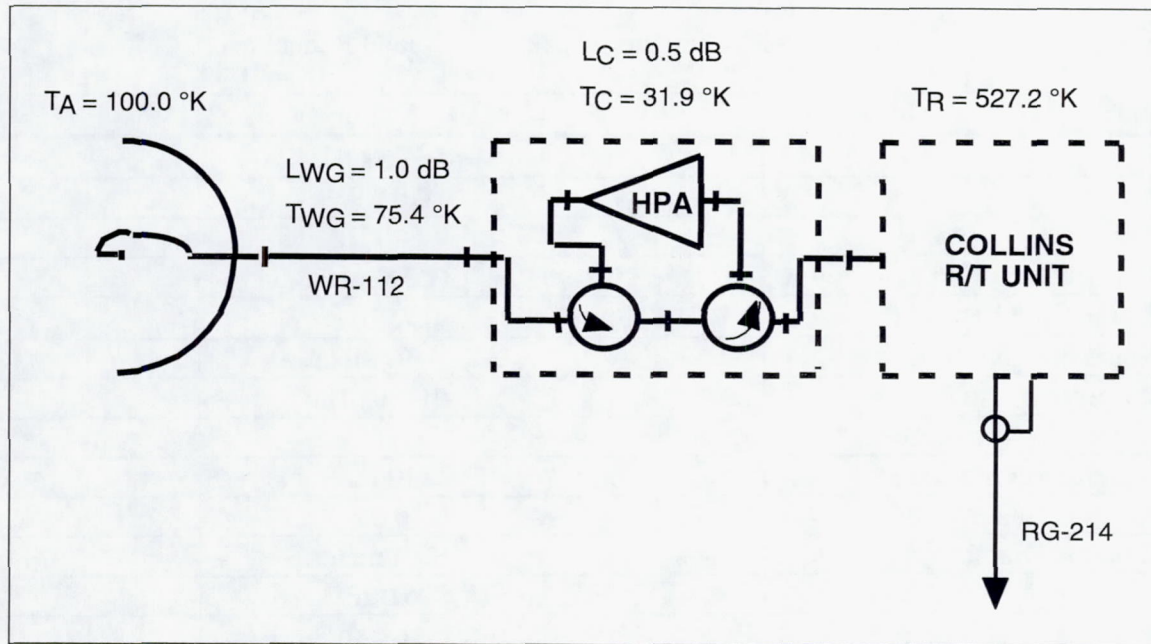


Figure 2–6. Schematic Diagram of X-band Doppler Radar.

Equation (2.1) is the single pulse signal-to-noise ratio radar equation for distributed clear air targets. This equation is used to predict the performance of a radar, given the volume reflectivity and range to a target. A signal-to-noise ratio of 1.0, or 0 dB, is required for detection of a distributed target.

$$\frac{S}{N} = \frac{\eta P_t G^2 \lambda^2 \theta^2 \frac{c\tau}{2} B_f}{R^2 (256\pi^2) k T_s B L_{wg}} \quad (2.1)$$

where η ≡ radar volume reflectivity (dB m^{-1}), and R is the range to the distributed target.

Radar volume reflectivity in wake vortices has been reported in the literature to be between -116 and -151 dB m^{-1} for clear air. (See Table 1.) Recent work indicates that higher values of volume reflectivity are found at the boundaries of the wake containing both vortices, and lower values are found around individual vortex cores (Marshall, et al., 1997). A Doppler radar such as the Wallops X-band Doppler radar, with sample volume of similar size to an aircraft wake, would require sensitivity to -135 dB m^{-1} before the wake would be detected.

Table 2-2. Characteristics of the X-band Radar

Radar Parameter	Design Value	Actual Value, if different
Transmitter power, P_t	2 kW	700 W
Antenna gain, G	55.1 dB	
Wavelength, λ	0.032 m (-14.95 dB m)	
Antenna beamwidth, θ	0.25 ° (-23.6 dB rad)	
Speed of light, c	3×10^8 m sec ⁻¹ (84.8 dB c)	
Pulse Width, τ	0.25 μsec (-66.0 dB sec) 0.50 μsec (-63.0 dB sec) 1.0 μsec (-60.0 dB sec)	
Beam fill factor, B_f	≤ 1.0 (0 dB)	
Boltzman's constant, k	1.38×10^{-23} (-228.6 dBW °K ⁻¹ Hz ⁻¹)	
System noise temperature, T_s	666 °K	755.1 °K (28.8 dB °K)
B	$1.5\tau^{-1}$ 0.25 μsec 0.50 μsec 1.0 μsec	67.8 dB Hz 64.8 dB Hz 61.8 dB Hz
L_{wg}	2.0 dB	4.3 dB

The pre-experiment performance specification for the high power amplifier was 2 kW; however, field tests during the experiment indicated that the transmitter was only providing 700 watts. This translates to a loss of 4.6 dB in equation (2.1).

The antenna used at Wallops Island was a dual frequency antenna with two reflectors and two feeds. The primary reflector was a 20-meter diameter mesh antenna for UHF frequencies. The UHF feed was a rectangular waveguide, about the size of an air conditioning duct, which provided substantial blockage for the X-band illumination. The X-band reflector consisted of a set of metal plates forming an inner, 9-meter diameter parabolic reflector that was illuminated by a separate, X-band rectangular waveguide feed. Unfortunately, the metal plates were separated by gaps of at least one-wavelength, and adjoining plates provided discontinuities of at least one wavelength in the parabolic surface. The combination of poor surface tolerance and UHF feed blockage resulted in high antenna sidelobes and signal contamination from clutter.

3.0 SMOKE VIDEO ANALYSIS

The following two sections describe the smoke video analysis methodology used to obtain the range of the wake vortices as a function of time after the vortices were generated and the results of the analysis for the seven passes analyzed in post-experimental data processing. A major product of the smoke video analysis was to obtain the range of the wake vortices, so that they could be correlated with the range data of the X-band radar measurements. This correlation was used to restrict post-processing of the X-band radar data to those C-130 passes where the range to the wake vortices determined by the smoke video data and the radar data overlapped. The methodology for the smoke video analysis uses information from an Informix database that was developed and maintained by NASA with data from this experiment.

After collecting the radar and video data during the experiment, the researchers discovered two problems with the video cameras: 1) the boresight camera data was not time synchronized with the radar data; and 2) the boresight camera on the X-band radar was misaligned. The effect of these deficiencies was minimized through use of data from the tracking radar; however, these problems contributed to the following errors in the experimental data.

- During some of the C-130 passes, the X-band radar was manually aimed using the boresight camera to align the radar with the smoke trail. Because of the misalignment, the radar was not actually aimed at the wake vortex, and the desired radar data was not acquired.
- The compensation for the misalignment consisted of a fixed offset at the beginning of each pass. However, this compensation did not account for a varying error during a pass.

3.1 Smoke Video Analysis Methodology

This section outlines the procedure in annotated form for the use of other researchers interested in conducting a further analysis of the data sets. This procedure was used to determine the relevant time interval and range information for post-processing of the X-band radar data.

1. Synchronize time between the X-band radar and the boresight video camera by determining the difference in between the video time and IRIG time, which is used by the X-band radar.
 - a) Find a C-130 pass that occurs on the same day as the pass of interest. Since the equipment is not turned off during the day, synchronization need only be performed once for all passes occurring during that day. The selected pass should show the C-130 apparently switching direction on the video tape, i.e., the camera switches scanning direction while the aircraft is in the field-of-view.
 - b) Using the time stamp on the video and the single frame advance feature of the video cassette recorder (VCR), note the time at which the aircraft apparently changes direction. The video time stamp provides accuracy to 1 second, while the frame advance occurs at one-thirtieth of a second.
 - c) From the *wake.xposition* table in the Informix data base containing scanning angle as a function of IRIG time, find the time of the change in radar scan direction—the time when the angle (either azimuth or elevation depending on the type of scan) changes from increasing to decreasing, or vice versa. This corresponds to the apparent change in aircraft direction on the video tape.
 - d) Subtract the time noted in a) from the time noted in c) to obtain the time synchronization between the boresight video camera and the X-band radar for that particular day.
 2. Perform a boresight correction for each C-130 pass.
 - a) From tracking radar data, note the azimuth, elevation, and time when the C-130 would appear on the boresight camera video tape.
 - b) Move to the location on the video tape corresponding to this time, as determined by the time stamp and the synchronization offset found in 1d).
 - c) On a template that has azimuth and elevation tick marks, annotate the location of the aircraft from the tracking radar information.

- d) Place the template so that the annotation is over the C-130 on the video. The cross-hairs on the template now denote boresight; thus, the misalignment error is manifested by the cross-hairs not being in the exact center of the TV screen. This template, which now accounts for the misalignment error, may be used directly to determine time intervals in the X-band radar data for wake vortex analysis..
3. Make list of smoke "hits."
 - a) Record the range of times that the cross-hair from the template is directly over a smoke trail.
 - b) Enter these times into the spreadsheet, categorized by left, right, upper, or lower trail. The spreadsheet is devised so that these values are entered in the right-most columns, and time synchronization is calculated and entered into the left-most columns automatically.
4. Record positioning information from Camera 2 or Camera 5.
 - a) Move to the pass of interest in either the Camera 2 or Camera 5 videotape, whichever has the better image. Remembering to include the azimuth and/or elevation offsets that are obtained from the log book, note the azimuth and elevation of two points on the smoke trail.
 - b) Using MATLAB¹, calculate the range of the C-130 from the 2 points in 4a) and the azimuth/elevation of the smoke trail from the boresight camera, which can be obtained from the table *wake.xposition*.

¹ A MATLAB program, written by NASA, calculates the radar range to the vortex based on video location of the smoke via camera sightings and camera locations. From either Camera 2 or Camera 5, two sightings (azimuth plus elevation for points on the smoke trail) and the surveyed location of the camera define a plane containing the smoke trail in 3-D. The boresight camera azimuth, elevation, and location defines a line that pierces the plane at the point where the smoke is observed by the radar. This intersection, which defines the range to the target, is then calculated.

3.2 Smoke Video Analysis Results

Seven C-130 passes were selected using the methodology in Section 3.1 to restrict post-processing of the X-band radar data to those passes where the range to the wake vortices as determined by the smoke video data and the radar data overlapped. The passes meeting this criterion are: 44, 55, 97, 116, 122, 124, and 135. The location and duration of radar observation of the vortices from the smoke analysis are shown in Tables 3–1 through 3–7. Range accuracy for the cameras was on the order of 100 meters (about a range gate for the C-band radar, and 2 or 3 range bins for the X-band radar), which was sufficient accuracy to verify vortex detections in the radar data.

Table 3–1. Smoke Analysis Results for Pass 44

Upper Vortex at Boresight				
IRIG Time		Boresight Pointing (Point 3)		MATLAB Results
Begin	End	Azimuth	Elevation	Range (m)
18:42:51.7	18:42:58.7	115.94	18.64	1563.40
18:42:59.2	18:42:59.4	115.94	17.78	1599.20
18:43:35.7	18:43:37.2	115.94	17.27	1621.50
Lower Vortex at Boresight				
18:42:41.7	18:42:44.7	115.94	18.64	1563.40
18:43:00.2	18:43:05.7	115.94	18.07	1586.90
18:43:07.7	18:43:07.9	115.94	16.99	1634.00
18:43:21.7	18:43:28.7	115.94	17.28	1621.00
18:43:37.2	18:43:37.3	115.94	15.97	1681.70
18:43:49.7	18:43:56.7	115.94	16.36	1663.10
18:44:03.1	18:44:03.2	115.94	14.92	1734.30
18:44:17.7	18:44:31.7	115.94	15.41	1709.30

Table 3–2. Smoke Analysis Results for Pass 55

Left Vortex at Boresight				
IRIG Time		Boresight Pointing (Point 3)		MATLAB Results
Begin	End	Azimuth	Elevation	Range (m)
20:05:13.0	20:05:13.1	33.05	20.00	994.64
20:05:22.1	20:05:22.2	33.15	20.00	994.16
20:05:32.9	20:05:33.0	31.17	20.00	1003.70
20:05:40.9	20:05:41.1	30.89	20.00	1005.10
20:05:48.1	20:05:48.3	29.26	20.00	1013.20
20:06:01.6	20:06:02.8	29.24	20.00	1013.30
20:06:08.4	20:06:08.6	28.25	19.98	1019.20

Right Vortex at Boresight				
IRIG Time		Boresight Pointing		MATLAB Results
Begin	End	Azimuth	Elevation	Range (m)
20:05:14.0	20:05:14.2	34.63	20.00	987.22
20:05:21.0	20:05:21.1	34.79	20.00	986.48
20:05:34.0	20:05:34.2	33.02	20.00	994.78
20:05:39.2	20:05:39.4	33.33	20.00	993.31
20:05:49.6	20:05:49.8	31.62	20.00	1001.50
20:06:01.0	20:06:01.2	30.84	19.99	1005.80
20:06:09.2	20:06:09.4	29.64	19.98	1012.20
20:06:14.4	20:06:14.6	29.97	20.00	1009.70
20:06:26.8	20:06:27.4	28.11	20.02	1018.20
20:06:32.4	20:06:33.2	28.80	20.00	1015.60

Table 3–3. Smoke Analysis Results for Pass 97

Lower Vortex at Boresight				
IRIG Time		Boresight Pointing (POINT 3)		MATLAB Results
Begin	End	Azimuth	Elevation	Range (m)
19:32:23.2	19:32:27.0	115.96	29.28	1229.20
19:32:43.0	19:32:48.0	115.96	27.77	1263.90
19:32:54.7	19:32:56.3	115.96	26.74	1289.10

Upper Vortex at Boresight				
19:32:57.9		19:32:59.9	115.96	26.74
Note: The radar was apparently steered with a misaligned boresight camera; thus, smoke hits were rare.				

Table 3–4. Smoke Analysis Results for Pass 116

Left Vortex at Boresight		Boresight Pointing (Point 3)		MATLAB Results
IRIG Time	IRIG Time	Azimuth	Elevation	Range (m)
Begin	End			
16:47:49.5	16:47:49.7	33.10	19.97	1246.10
16:47:53.7	16:47:54.0	31.64	19.96	1258.00
16:47:59.8	16:48:00.1	30.06	19.95	1271.20
16:48:04.4	16:48:04.8	28.66	19.96	1281.90
16:48:09.6	16:48:09.8	27.14	19.97	1293.90
16:48:14.8	16:48:15.1	25.44	19.96	1308.80
16:48:19.7	16:48:19.9	23.97	19.97	1320.80
16:48:28.7	16:48:29.1	21.18	19.96	1346.10
16:48:34.3	16:48:34.7	19.15	19.97	1363.80
16:48:41.4	16:48:41.9	16.97	19.96	1384.70
16:48:46.9	16:48:47.2	15.15	19.97	1401.20
16:48:53.8	16:48:54.6	12.30	19.96	1429.60
16:48:59.9	16:49:00.2	9.69	19.97	1454.70
16:49:10.8	16:49:11.5	4.55	19.96	1508.10
16:49:17.3	16:49:17.6	1.63	19.97	1537.90
16:49:29.3	16:49:29.9	357.40	19.98	1582.20
16:49:35.4	16:49:35.8	355.25	19.93	1610.30
Right Vortex at Boresight				
16:47:50.3	16:47:50.5	34.43	19.97	1235.90
16:47:52.4	16:47:52.6	33.87	19.95	1241.30
16:48:00.9	16:48:01.1	31.65	19.97	1257.40
16:48:03.0	16:48:03.2	30.93	19.96	1263.60
16:48:10.6	16:48:10.8	28.70	19.95	1282.20
16:48:13.2	16:48:13.5	27.79	19.96	1289.10
16:48:20.6	16:48:20.9	25.44	19.97	1308.20
16:48:27.3	16:48:27.6	23.40	19.96	1326.50
16:48:35.5	16:48:35.9	20.93	19.96	1348.40
16:48:39.6	16:48:40.0	19.65	19.96	1359.90
16:48:48.0	16:48:48.3	16.83	19.95	1386.80
16:48:51.9	16:48:52.3	15.50	19.95	1399.40
16:49:00.9	16:49:01.5	11.41	19.95	1439.10
16:49:08.4	16:49:09.0	8.32	19.95	1470.10
16:49:18.2	16:49:18.5	3.11	19.95	1524.10
16:49:27.9	16:49:28.2	0.01	19.93	1557.00
16:49:36.7	16:49:36.9	na	na	na

Table 3–5. Smoke Analysis Results for Pass 122

Left Vortex at Boresight				
IRIG Time		Boresight Pointing (Point 3)		MATLAB Results
Begin	End	Azimuth	Elevation	Range (m)
17:21:50.5	17:21:50.6	23.77	14.90	1773.60
17:21:53.1	17:21:53.3	23.31	14.91	1779.80
17:21:59.7	17:22:00.0	21.96	14.90	1803.10
17:22:02.4	17:22:02.5	21.23	14.91	1813.90
17:22:07.7	17:22:07.9	20.48	14.90	1827.80
17:22:10.1	17:22:10.3	19.92	14.89	1838.60
17:22:16.2	17:22:16.4	18.81	14.90	1856.40
17:22:18.8	17:22:19.0	17.87	14.90	1872.80
17:22:25.1	17:22:25.4	16.34	14.90	1900.00
17:22:28.1	17:22:28.2	15.91	14.92	1904.90
17:22:34.7	17:22:34.9	14.73	14.91	1927.80
17:22:37.7	17:22:37.8	14.25	14.92	1935.20
17:22:44.5	17:22:44.8	12.78	14.90	1965.60
17:22:47.5	17:22:47.7	11.85	14.92	1980.20
17:22:54.9	17:22:55.1	10.47	14.90	2010.00
17:23:03.5	17:23:05.5	8.77	14.90	2043.50
Right Vortex at Boresight				
Begin	End	Azimuth	Elevation	Range (m)
17:21:49.6	17:21:49.7	25.06	14.90	1753.20
17:21:53.7	17:21:53.8	24.33	14.89	1765.90
17:21:58.8	17:21:59.1	23.40	14.90	1779.60
17:22:02.9	17:22:03.1	22.45	14.90	1795.00
17:22:06.9	17:22:07.1	21.67	14.90	1807.90
17:22:10.7	17:22:10.9	21.12	14.90	1817.10
17:22:15.1	17:22:15.2	20.45	14.90	1828.30
17:22:19.6	17:22:19.8	19.42	14.90	1845.90
17:22:24.0	17:22:24.2	18.26	14.89	1867.30
17:22:29.0	17:22:29.1	17.39	14.91	1879.90
17:22:33.4	17:22:33.6	16.93	14.90	1889.40
17:22:38.6	17:22:39.0	15.96	14.89	1908.30
17:22:43.6	17:22:43.8	14.31	14.90	1937.00
17:22:48.5	17:22:48.6	13.47	14.91	1951.20
17:22:53.5	17:22:53.7	12.66	14.90	1967.90

Table 3–6. Smoke Analysis Results for Pass 124

Left Vortex at Boresight				
IRIG Time		Boresight Pointing (Point 3)		MATLAB Results
Begin	End	Azimuth	Elevation	Range (m)
17:33:43.5	17:33:43.6	26.88	14.90	1719.90
17:33:48.5	17:33:50.0	25.88	14.90	1735.20
17:34:06.3	17:34:06.5	23.36	14.90	1774.90
17:34:17.5	17:34:19.0	21.21	14.90	1810.20
17:34:46.0	17:34:46.3	14.94	14.91	1919.40
17:34:47.1	17:34:47.6	14.36	14.89	1933.00
Right Vortex at Boresight				
IRIG Time		Boresight Pointing (Point 3)		MATLAB Results
Begin	End	Azimuth	Elevation	Range (m)
17:33:42.7	17:33:42.8	28.10	14.90	1701.70
17:33:55.5	17:33:57.0	25.88	14.90	1735.20
17:34:05.6	17:34:05.8	24.64	14.90	1754.50
17:34:23.0	17:34:24.5	21.21	14.90	1810.20
17:34:33.3	17:34:33.5	18.82	14.90	1851.00
17:34:34.5	17:34:34.7	18.31	14.90	1860.00
17:34:45.1	17:34:45.8	16.14	14.90	1898.80
17:34:50.0	17:34:52.0	no pointing info		

Table 3–7. Smoke Analysis Results for Pass 135

Lower Vortex at Boresight				
IRIG Time		Boresight Pointing (Point 3)		MATLAB Results
Begin	End	Azimuth	Elevation	Range (m)
18:56:02.0	18:56:02.1	115.96	28.55	1005.50
18:56:10.5	18:56:10.6	115.97	29.02	995.72
18:56:35.8	18:57:15.5	115.96	27.71	1023.70
18:57:26.5	18:57:41.5	115.98	27.72	1023.40
Right Vortex at Boresight				
IRIG Time		Boresight Pointing (Point 3)		MATLAB Results
Begin	End	Azimuth	Elevation	Range (m)
18:56:02.3	18:56:02.4	115.96	27.78	1022.10
18:56:10.2	18:56:10.3	115.97	28.38	1009.10
18:56:11.6	18:56:17.2	115.97	28.67	1003.00
18:56:34.4	18:56:34.7	115.97	28.39	1008.90

4.0 METEOROLOGICAL DATA ANALYSIS

Rawinsonde data for the aircraft passes were used to calculate vertical soundings of vortex decay time, cross aircraft bearing wind speed, and water vapor mixing ratio. These products of the meteorological sounding data were a reliable tool for defining radar scan strategies and the placement of wake generating aircraft.

Cross aircraft bearing wind speed, the component of wind orthogonal to the wake axis, is a good predictor of the horizontal transport of the vortices after they are generated by the C-130. Analysis of this component of wind aids in proper placement of the generating aircraft upwind of the X-band radar.

The Brunt-Vaisala period is a crude, but experimentally effective, predictor of vortex decay time (Sorbian, 1989). In atmospheric layers where this parameter exceeded 100 seconds, the vortices persisted for periods much longer than 100 seconds.

Water vapor mixing ratio is typically conserved in the neutral boundary layer and is a necessary atmospheric constituent for the production of small scale variations in refractive index. Discontinuities in water vapor mixing ratio on the order of one-half the radar wavelength contribute to clear air radar volume reflectivity.

This section presents the characteristic decay time (Brunt-Vaisala period), water vapor mixing ratio, and cross aircraft bearing wind speed for the seven C-130 passes that were selected for further analysis by the methodology in Section 3. A description of the meteorological conditions present during each pass is also provided. The figures showing cross aircraft bearing wind speed are also annotated with the symbols “St” and “Se,” which indicate “upwind vortex stall” and “vortex separation,” respectively.

For passes 97 and 135, the wake was released above the top of the atmospheric boundary layer. A discontinuity in potential temperature marks the top of the daytime atmospheric boundary layer; this discontinuity may interact with the descending aircraft wake. Since potential temperature is conserved in a well-mixed atmospheric boundary layer, a wake generated above this level would descend through the boundary with associated entrainment and turbulence that may influence persistence of the vortex structure.

4.1 Meteorological Data for Pass 44

Pass 44 occurred at 1842 UTC on January 9, 1995. The radar was in a cross-wake axis staring mode and used a 0.96 μ sec pulse length. The wake was generated at 490 m above ground level (AGL) in the near neutral planetary boundary layer where the wakes are predicted to persist for several minutes, as shown in figure 4-1. Figure 4-2 shows that the descending vortices would be in a layer with relatively high water vapor—2.5 to 3.0 g kg^{-1} . Figure 4-3 shows the component of wind orthogonal to the aircraft bearing. The vortices were predicted to stall or separate slowly and should have had, at most, a very slow drift towards the radar.

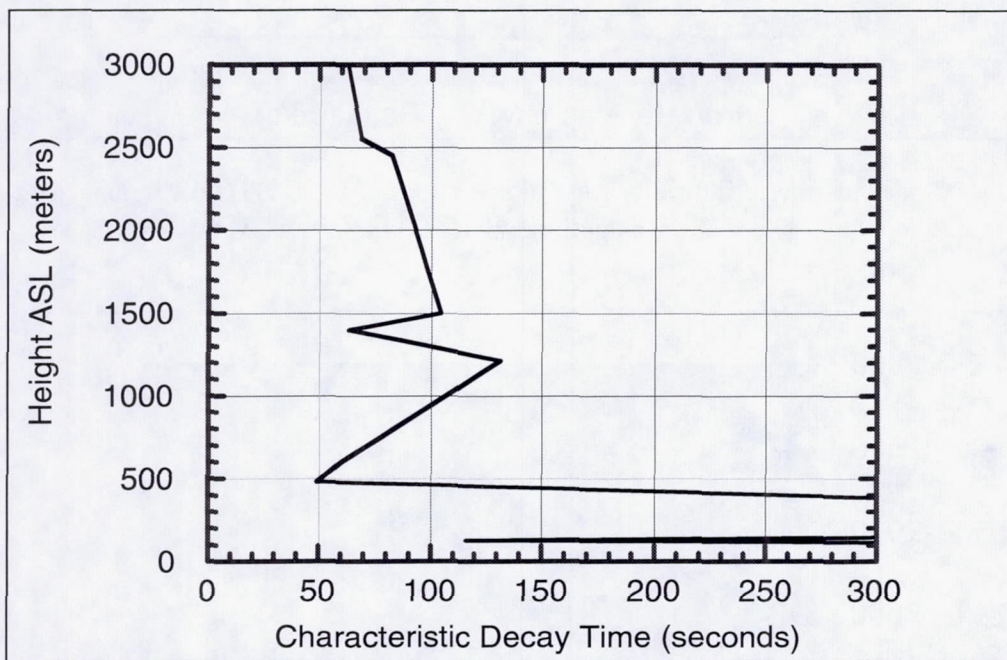


Figure 4-1. Characteristic decay time (Brunt-Vaisala Period) for wake vortices at 1800 UTC on January 9, 1995. (The wake was generated at 490 meters AGL.)

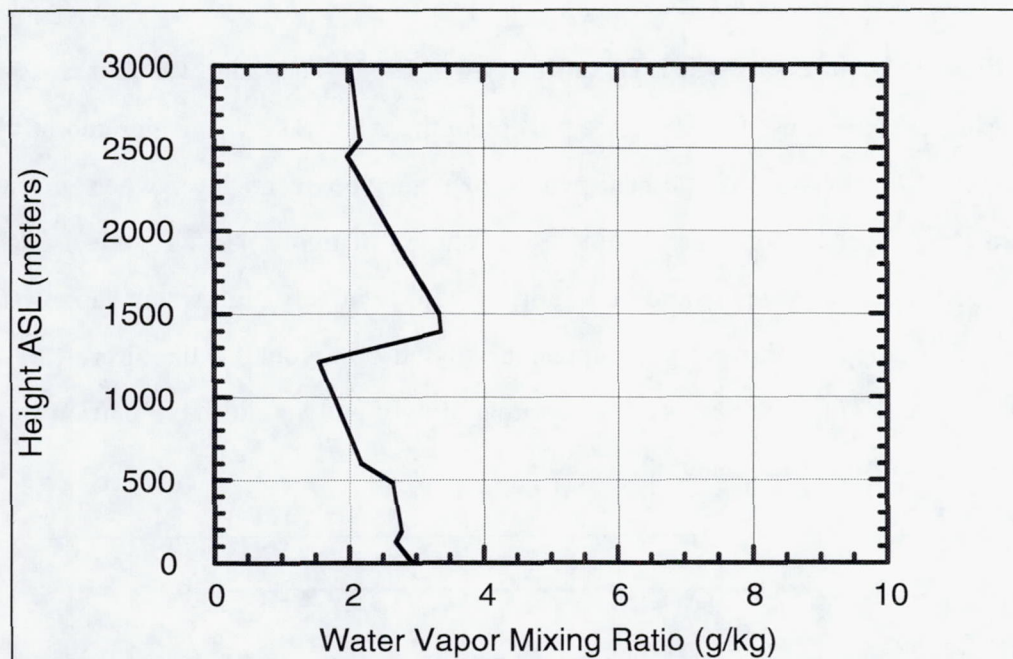


Figure 4-2. Atmospheric humidity for wake vortices at 1800 UTC on January 9, 1995.
(The wake was generated at 490 meters AGL.)

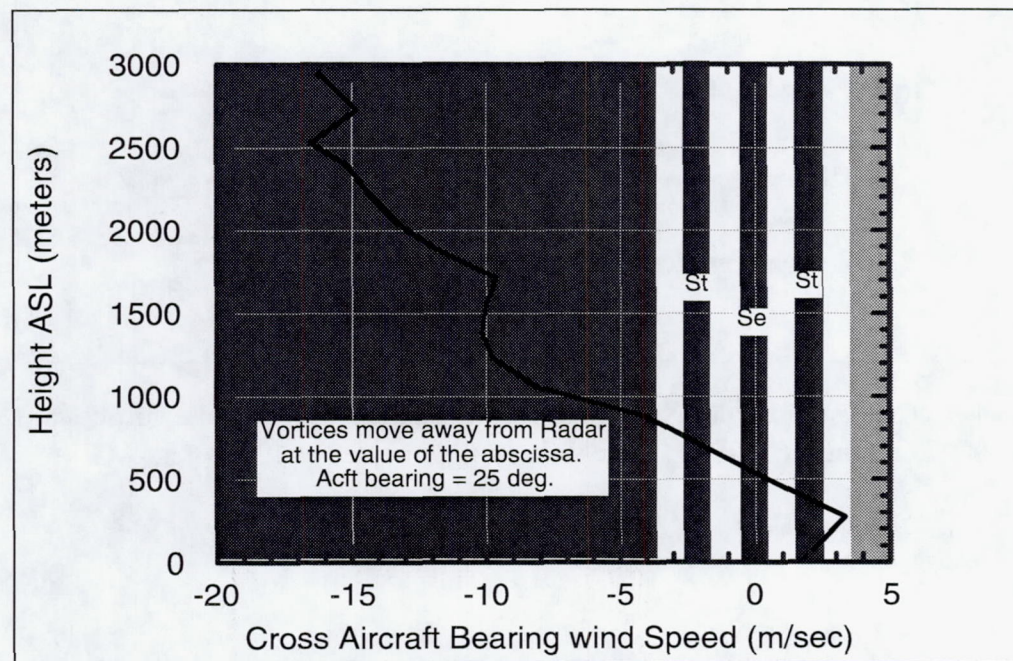


Figure 4-3. Cross aircraft bearing wind speed for wake vortices at 1800 UTC on January 9, 1995. (The wake was generated at 490 meters AGL.)

4.2 Meteorological Data for Pass 55

Pass 55 occurred at 2005 UTC on January 9, 1995. The radar was in an along-the-wake axis staring mode and used a 0.22 μ sec pulse length. This sounding occurred approximately two hours after the sounding used for Pass 44, described in figures 4-1 through 4-3. The boundary layer has grown in height by 100 meters, but the atmosphere experienced by the wake retains the same wind, stability, and humidity characteristics.

The aircraft generated the wake at 400 meters AGL. At this altitude, figure 4-4 predicted that the descending vortices would persist for approximately 2 minutes. The descending vortices were in a layer with 2.8 g kg^{-1} of water vapor (figure 4-5), and were predicted to stall or separate slowly (figure 4-6).

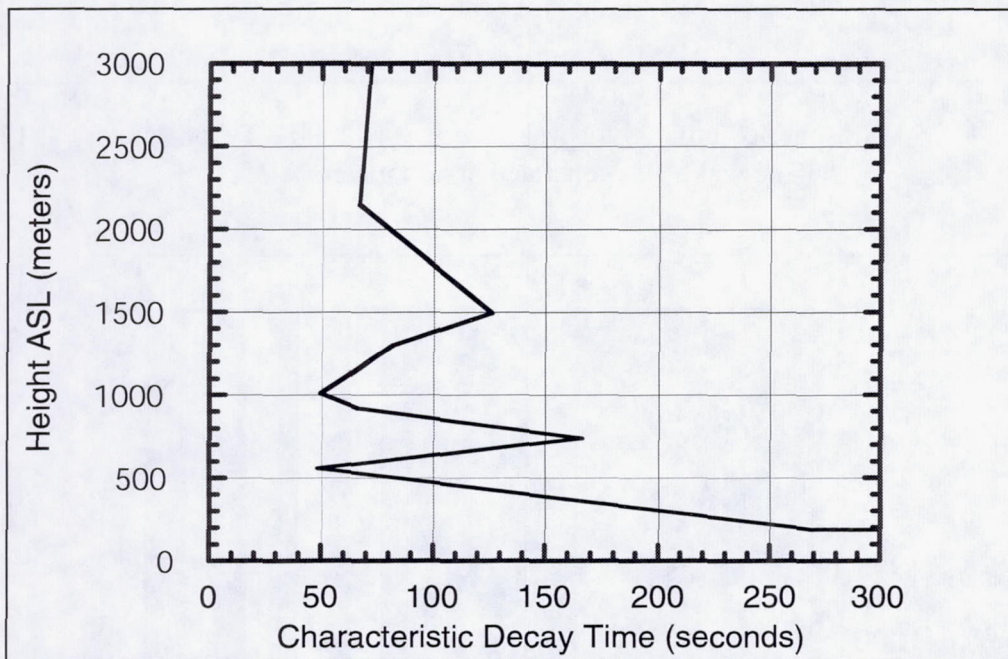


Figure 4-4. Characteristic decay time (Brunt-Vaisala Period) for wake vortices at 2000 UTC on January 9, 1995. (The wake was generated at 400 meters AGL.)

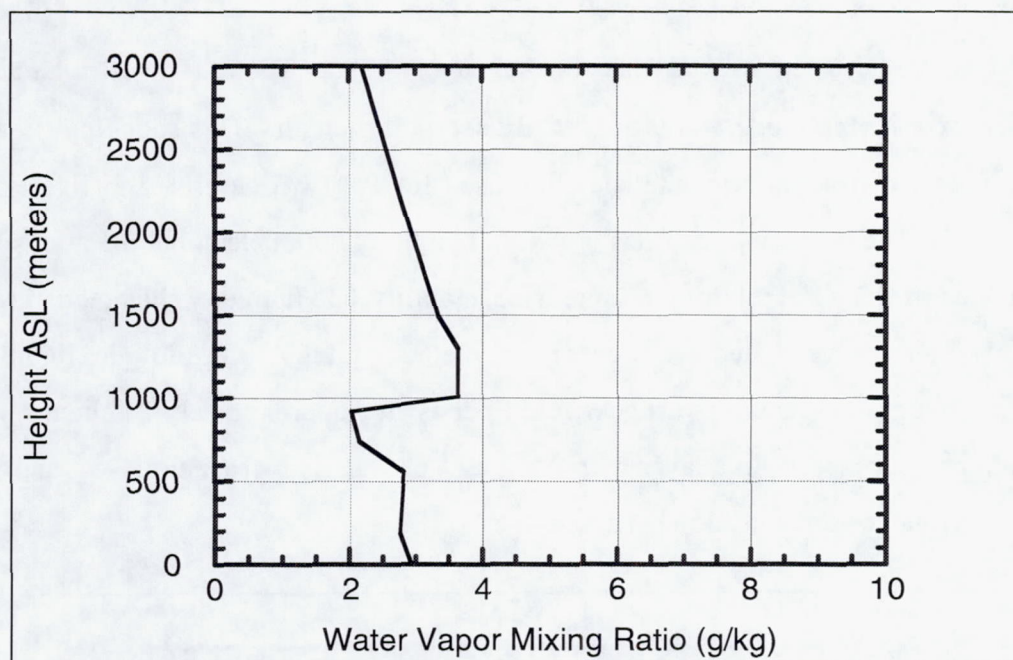


Figure 4-5. Atmospheric humidity for wake vortices at 2000 UTC on January 9, 1995.
(The wake was generated at 400 meters AGL.)

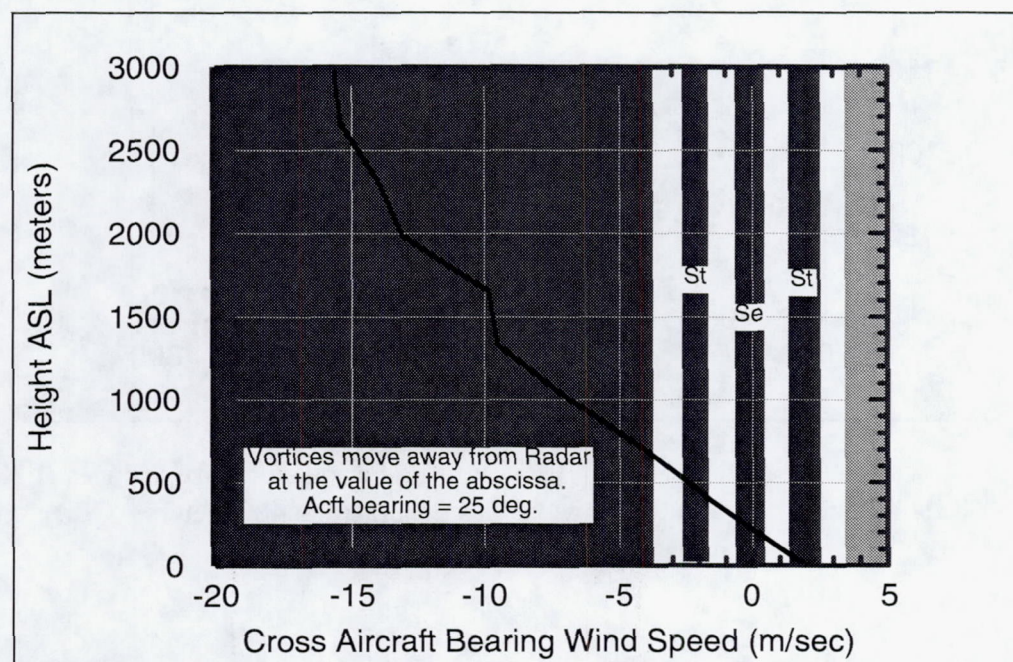


Figure 4-6. Cross aircraft bearing wind speed for wake vortices at 2000 UTC on January 9, 1995. (The wake was generated at 400 meters AGL.)

4.3 Meteorological Data for Pass 97

Pass 97 occurred at 1932 UTC on January 10, 1995. The radar was in an across-the-wake axis staring mode and used a 0.48 μ sec pulse length. This sounding indicated that the top of the atmospheric boundary layer was approximately 500 meters above ground level. The wake was generated at 610 m AGL, 110 meters above the boundary layer, where the wake was predicted to persist for 70 seconds (figure 4-7). The descending vortices were released in a layer with 2.6 g kg^{-1} of water vapor (figure 4-8) and were predicted to stall or separate slowly (figure 4-9).



Figure 4-7. Characteristic decay time (Brunt-Vaisala Period) for wake vortices at 1800 UTC on January 10, 1995. (The wake was generated at 610 meters AGL.)

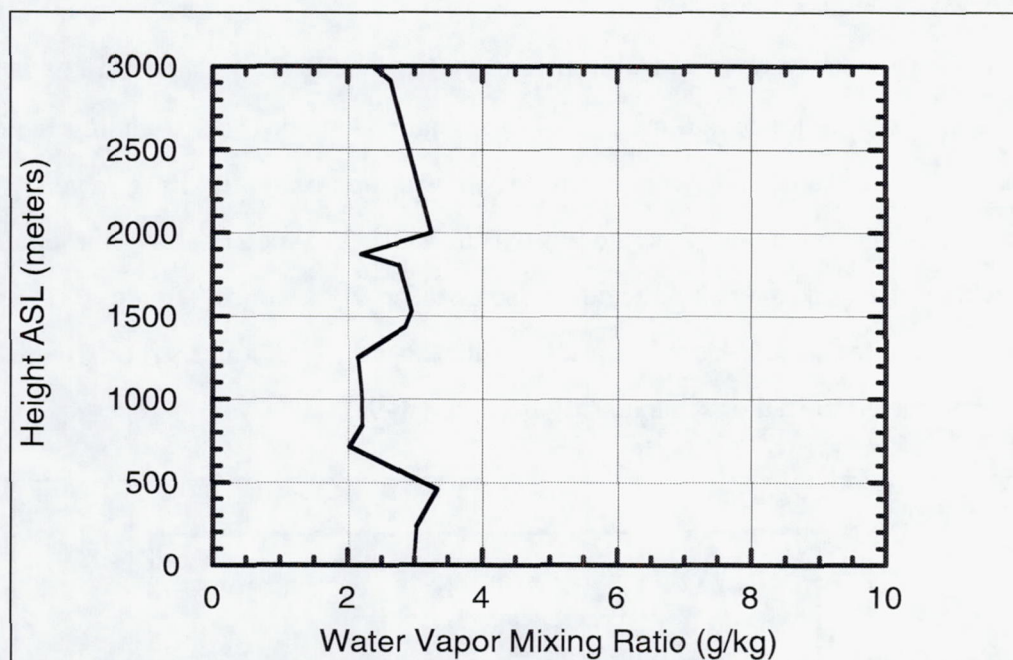


Figure 4-8. Atmospheric humidity for wake vortices at 1800 UTC on January 10, 1995.
(The wake was generated at 610 meters AGL.)

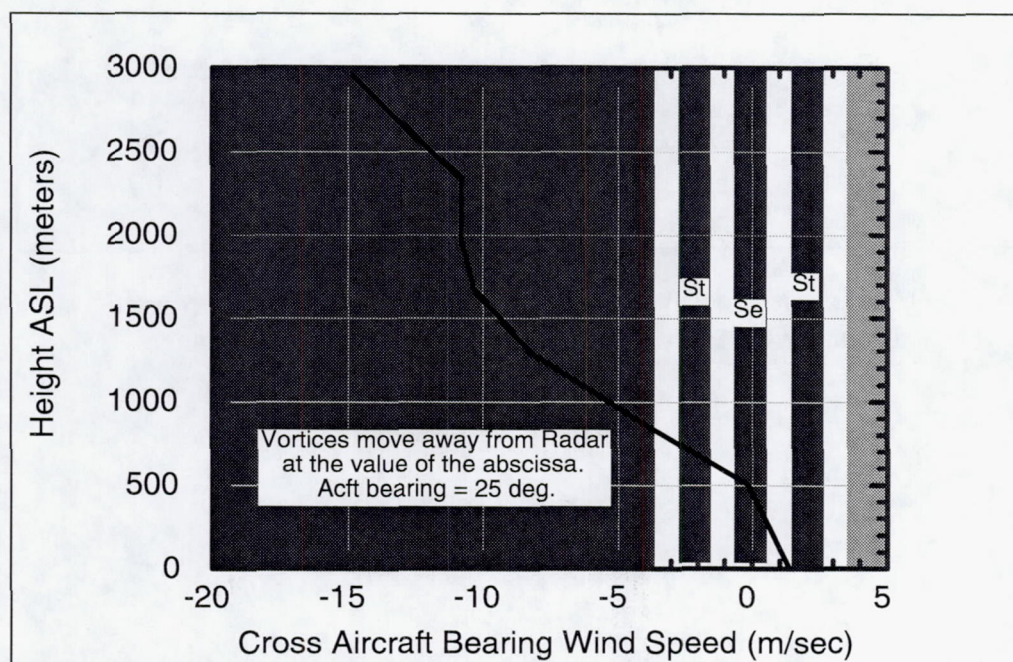


Figure 4-9. Cross aircraft bearing wind speed for wake vortices at 1800 UTC on January 10, 1995. (The wake was generated at 610 meters AGL.)

4.4 Meteorological Data for Passes 116, 122, and 124

Passes 116, 122, and 124 occurred at 1647, 1721, and 1733 UTC respectively on January 11, 1995. One sounding at 1600 UTC was used to prepare for all three passes. For Passes 116 and 122, the radar was scanned along the wake axis with a pulse width of 0.96 μ sec. Pass 124 was also an axial scan, but with a 0.48 μ sec pulse width.

The aircraft generated the wakes at 400 meters (Pass 116) and 490 meters (Passes 122 and 124). All wakes were generated below the 550 meter boundary layer height where the wakes were predicted to persist for a considerable time (figure 4-10). The water vapor mixing ratio was approximately 4.6 g kg^{-1} in this layer (figure 4-11), and the cross aircraft bearing wind speed predicted that the vortices would stall or move slowly towards the radar.

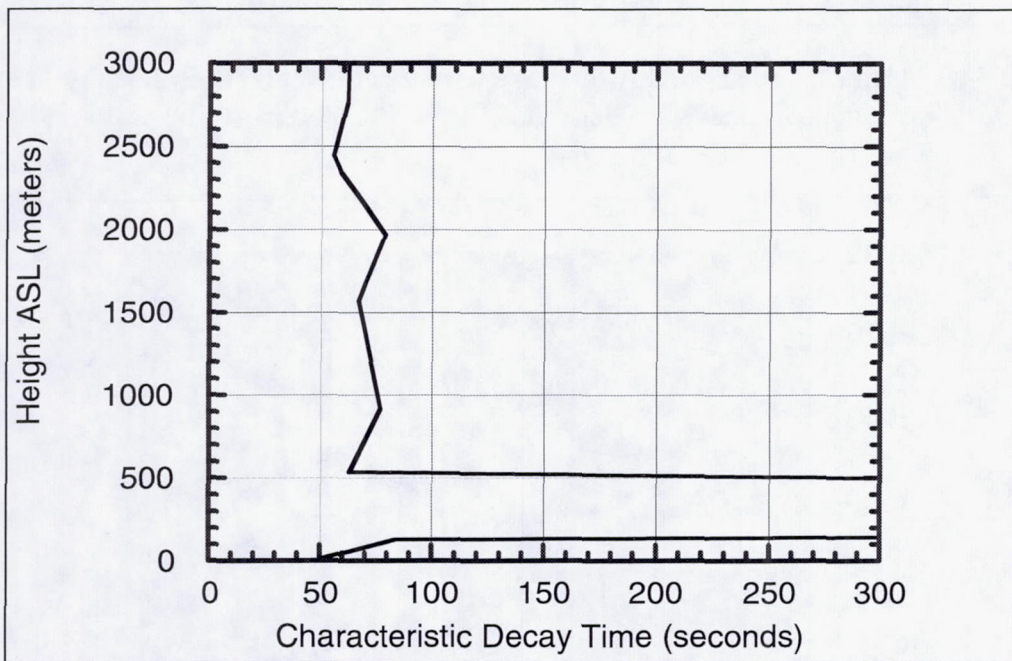


Figure 4-10. Characteristic decay time (Brunt-Vaisala Period) for wake vortices at 1600 UTC on January 11, 1995. (The wakes were generated below 500 meters where the atmosphere is near neutral.)

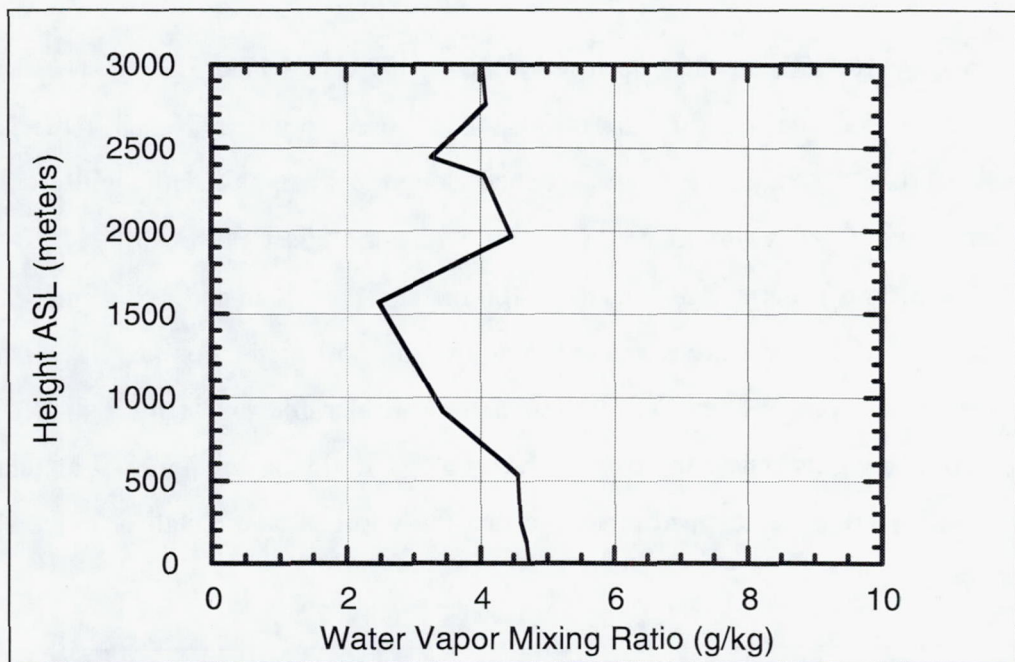


Figure 4-11. Atmospheric humidity for wake vortices at 1600 UTC on January 11, 1995.
(The wakes were generated below 500 meters AGL.)

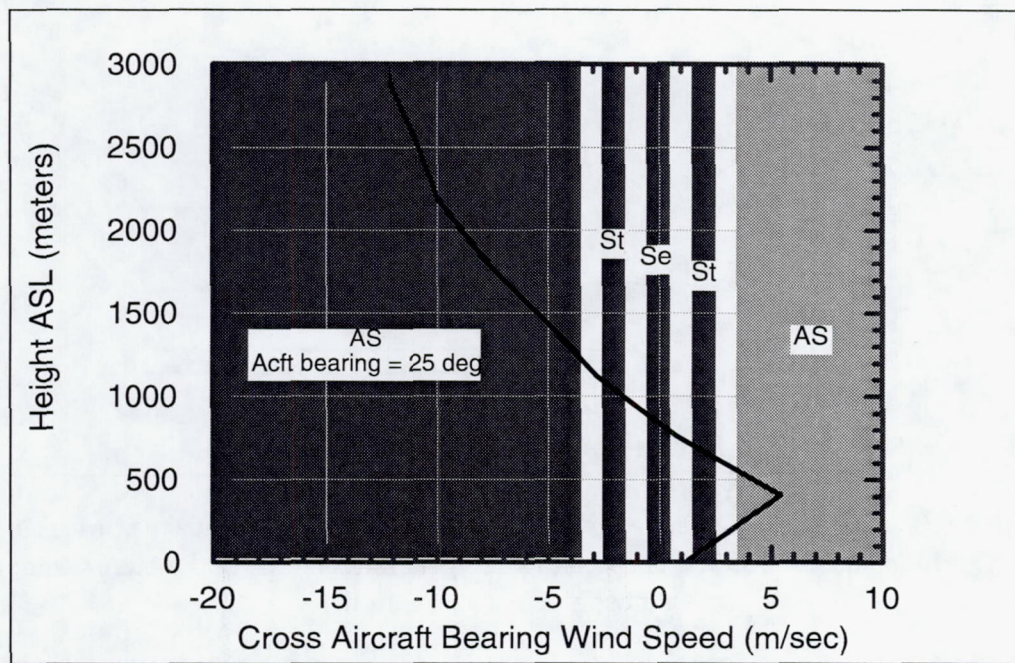


Figure 4-12. Cross aircraft bearing wind speed for wake vortices at 1600 UTC on January 11, 1995. (The wakes were generated below 500 meters AGL.)

4.5 Meteorological Data for Pass 135

Pass 135 occurred at 1856 UTC on January 11, 1995. The radar was in an across-the-wake axis staring mode and used a 0.48 μ sec pulse length. This sounding occurred two hours after the sounding described by figures 4–10 through 4–12 and indicated a significant change in the atmosphere. The boundary layer winds were similar, but the water vapor mixing ratio was no longer conserved. For pass 135, the wake was generated above the 500 meter boundary layer height at 610 meters AGL. The descending vortices were predicted to persist for 70 seconds (figure 4–13) in the layer with a water vapor content of 2.8 g kg^{-1} (figure 4–14). The descending vortices were predicted to stall or move slowly towards the radar (figure 4–15).

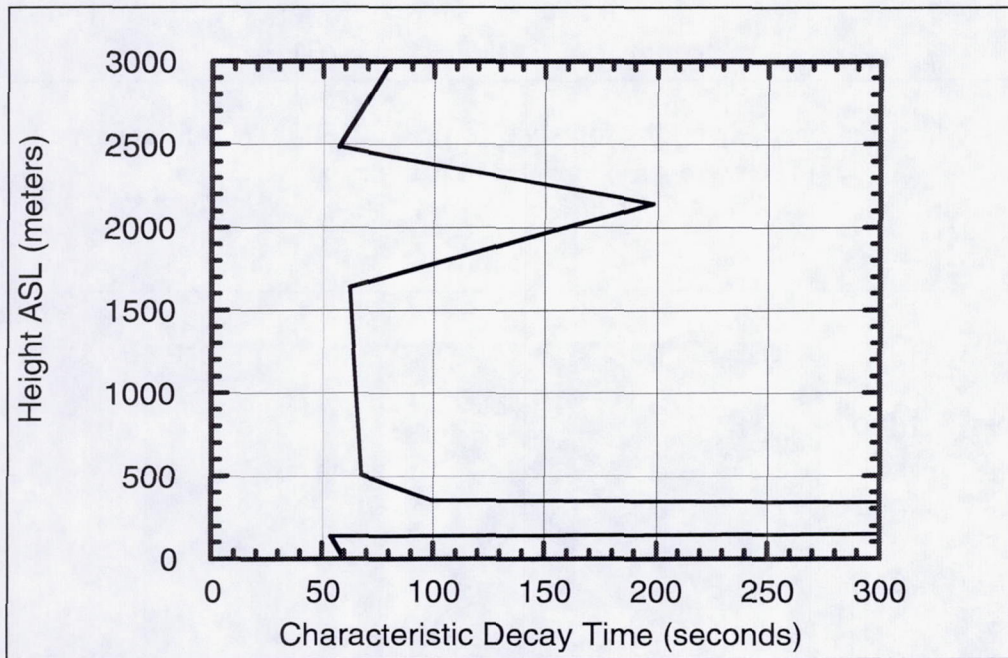


Figure 4–13. Characteristic decay time (Brunt-Vaisala Period) for wake vortices at 1800 UTC on January 11, 1995. (The wake was generated at 610 meters AGL.)

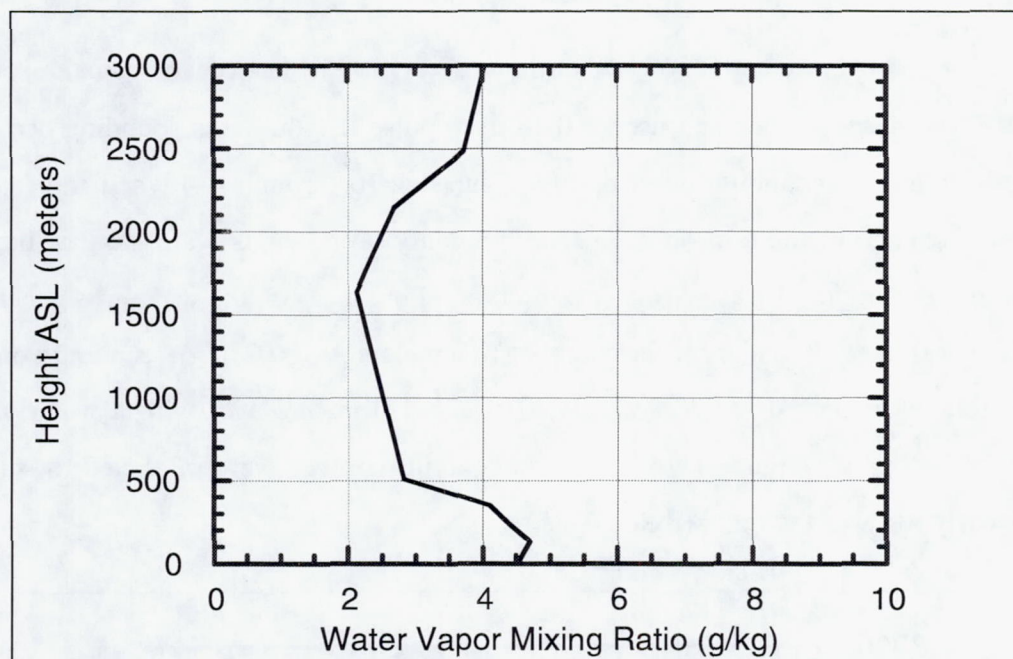


Figure 4-14. Atmospheric humidity for wake vortices at 1800 UTC on January 11, 1995.
(The wake was generated at 610 meters AGL.)

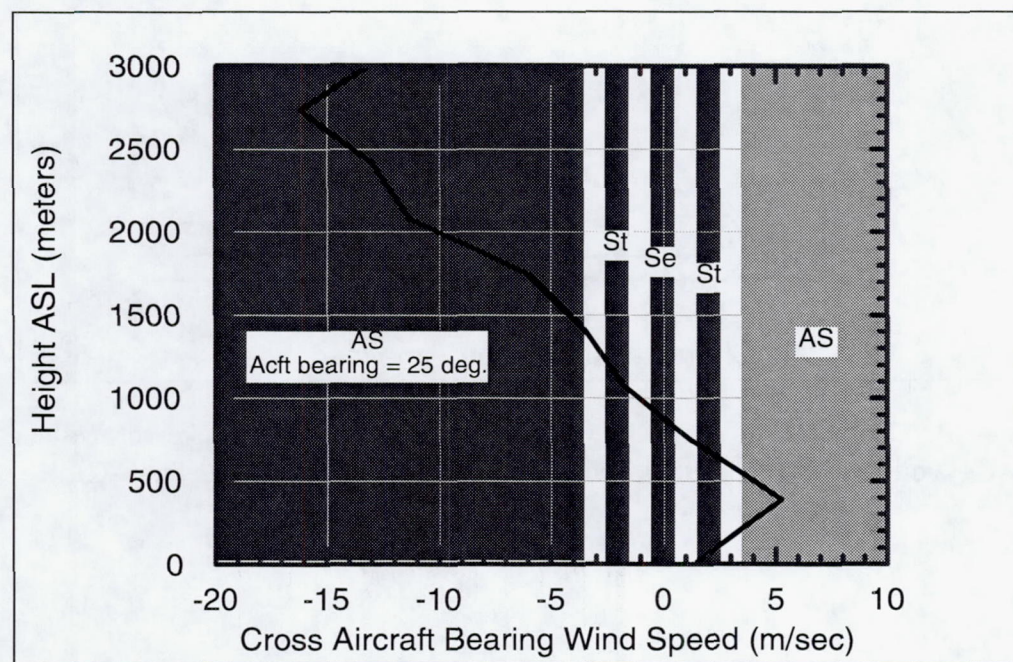


Figure 4-15. Cross aircraft bearing wind speed for wake vortices at 1800 UTC on January 11, 1995. (The wake was generated at 610 meters AGL.)

5.0 X-BAND RADAR DATA ANALYSIS

This section provides a detailed description of the procedure used to analyze the X-band radar data from the field experiments. The results of the analysis are presented, along with an explanation for the experimental outcome.

5.1 Data Analysis Procedure

The complex time series at each range bin were segmented into smaller blocks, and the power spectrum was then computed for each block. Clutter and noise suppression algorithms were applied to the power spectrum of the received signal to reduce the contribution from ground clutter targets and system noise. The zeroth-, first-, and second-moment of the spectrum corresponding to received power, mean radial velocity, and the spectrum width, respectively, were then computed from the power spectrum. In addition, the reflectivity-weighted spectrum width was also computed.

5.1.1 Estimation of Power Spectrum

The power spectrum, defined as the Discrete Fourier Transform (DFT) of the autocorrelation function, is often used to determine the frequency distribution of stationary random signals. A computationally efficient and accurate estimate of the power spectrum was obtained using Welch's averaged-periodogram method (Welch, 1967) described below:

- i. The complex time series $x[n], n = 0, \dots, N - 1$, was divided into p short segments, each of length $L = N / p$, and each segment was windowed using function $w[n]$ to yield: $x_r[n] = x[rL + n].w[n], \quad 0 \leq n \leq L - 1$. (5.1)

The windowing function chosen for analysis was a Hanning window given by:

$$w[n] = \begin{cases} 0.5 - 0.5\cos(2\pi n / L), & 0 \leq n < L \\ 0, & \text{otherwise.} \end{cases} \quad (5.2)$$

- ii. For each segment, the *modified periodogram* was obtained using:

$$P_r[k] = \frac{1}{LU} |X_r[k]|^2. \quad (5.3)$$

In eq. 3.3, $X_r[k]$ represents the DFT of $x_r[n]$ and is given by

$$X_r[k] = \sum_{n=0}^{L-1} x_r[n] \cdot e^{-j(2\pi/L)nk}. \quad (5.4)$$

The normalizing constant U is given by

$$U = \frac{1}{L} \sum_{n=0}^{L-1} w[n]^2 \quad (5.5)$$

iii. The individual periodograms corresponding to the p segments were then averaged to obtain the *modified averaged periodogram* given by:

$$\bar{P}[k] = \frac{1}{p} \sum_{r=0}^{p-1} P_r[k]. \quad (5.6)$$

Given the fact that the variance of the sum of p independent and identically distributed random variables is $1/p$ times the variance of each individual random variable, it

$$\text{follows that } \text{var}(\bar{P}[k]) = \frac{1}{p} \text{var}(P_r[k]).$$

This method of power spectrum estimation provides a convenient framework within which to trade between resolution and variance of the spectrum estimate. For the current analysis, values of $L = 256$ and $p = 4$ were used.

5.1.2 Clutter Suppression

Due to the high sidelobe levels of the radar antenna used in this experiment, the data was severely contaminated with clutter. From examining spectra from various passes at different range bins, it was observed that there was significant spillover of the clutter spectrum into frequency bins adjacent to the zero frequency line (DC). This smearing effect could be attributed to several factors, some of which are the phase noise from the exciter, transmitter, and receive system, antenna rotation, moving objects, etc. The clutter rejection scheme used here is designed based on the single slope search filter proposed by Passarelli et al. (1981), and allows for dynamically adjusting the notch-width of the filter to whatever clutter is present while attempting to preserve any overlapping signal component. It assumes that the clutter power spectrum falls off monotonically going outward from DC. This scheme is particularly well suited for the wake vortex data set because of the varying magnitude and width of the clutter spike and the embedded signal contribution. The operation of the filter is described below with the aid of Figure 5–1.

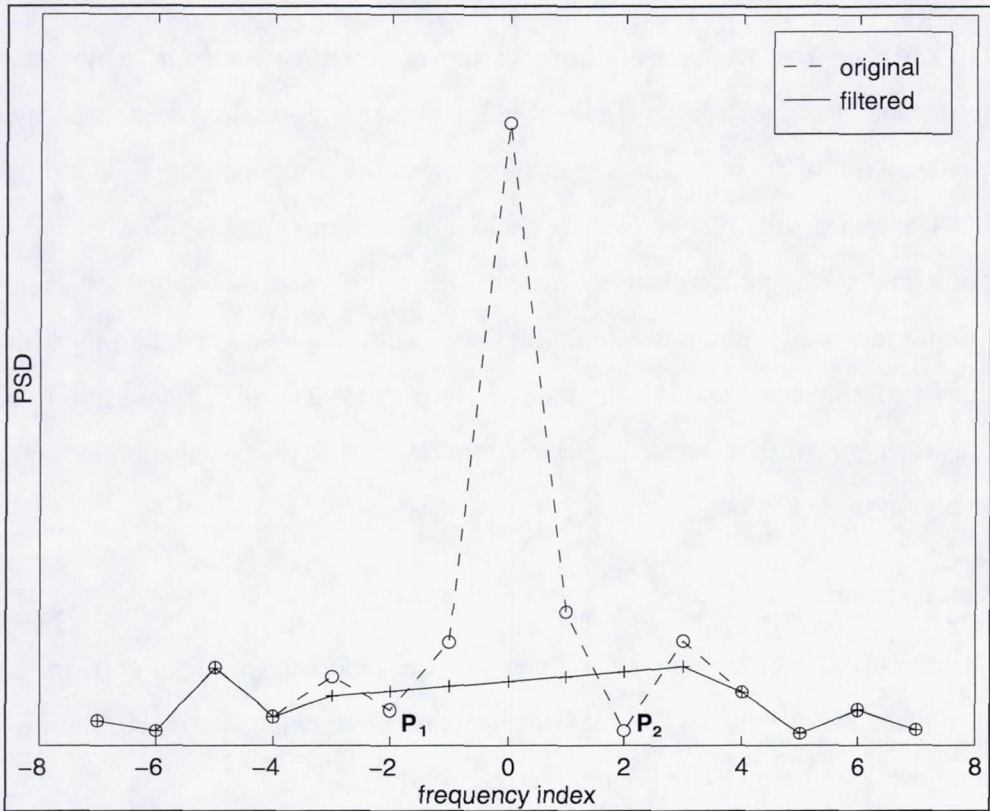


Figure 5–1. Schematic of Clutter Filtering Algorithm.

- i. Starting from the center component of the power spectrum (DC), the points where the slope of the spectrum changes sign are located in each direction (i.e., for positive and negative frequencies). These two points (P_1 and P_2) mark the extent of the clutter component in the power spectrum.
- ii. A check is made to see if P_1 and P_2 lie within the maximum limits set for the clutter spectrum (set to ± 1 m/s for current data set based on visual inspection of spectra). If P_1 and P_2 exceed the maximum limits, they are reset to span across the maximum limits.
- iii. The two points beyond P_1 and P_2 are then averaged and points in between are obtained through linear interpolation from these end points.

5.1.3 Noise Suppression

In order to remove contributions to the returned power from white noise and spectral artifacts, the spectral coefficients (after clutter suppression) were weighted with a rectangular window, centered at the strongest spectral component and extending to +/- 12.5 m/s on either side. The window-width of 25 m/s was chosen based on the assumption that the signal contribution from the wake vortices would not exceed this width. Other techniques such as estimating the mean noise-level at each range bin using the Kolmogorov-Smirnov test (Urkowitz and Nespor, 1992) did not yield good results at the close-in and far-out ranges as the spectra were dominated by clutter and noise, respectively, in these regions.

5.1.4 Moments Estimation

The zeroth, first, and second moments of the Doppler spectrum corresponding to received power, mean velocity, and spectrum width were calculated using the pulse-pair algorithm described below (Doviak and Zrnic, 1993):

- i. An estimate of the autocorrelation sequence $\hat{R}[mT_s]$ (T_s represents the pulse repetition time in seconds) is obtained through an inverse DFT of the power spectrum $\bar{P}[k]$, after correction for clutter and noise.
- ii. The received power (W) is given by;

$$\hat{P}_r = \hat{R}[0]. \quad (5.7)$$

- iii. The mean radial velocity of the target (in m/s) is given by:

$$\hat{V} = -\left[\frac{\lambda}{4\pi T_s} \right] \arg(\hat{R}[T_s]) \quad (5.8)$$

where λ is the transmit wavelength.

- iv. The spectrum width (in m/s) is given by:

$$\hat{\sigma}_v = \frac{\lambda}{2\pi T_s \sqrt{2}} \left| \ln \left(\frac{\hat{R}[0]}{\hat{R}[T_s]} \right) \right|^{\frac{1}{2}}. \quad (5.9)$$

- v. In addition, the reflectivity-weighted spectrum width is also computed using:

$$WSW = \hat{P}_r \hat{\sigma}_v. \quad (5.10)$$

5.2 Data Analysis

The top four panels of figures A-1 through A-34 in Appendix A plot the received power, mean velocity, spectrum width, and the power-weighted spectrum width, respectively, as a function of range (along y-axis) and time (along x-axis). Each plot corresponds to a 20-second time interval of data. The corresponding antenna pointing angles (elevation and azimuth) are plotted in the bottom panel. Also plotted in the bottom panel (solid-red line) is the time interval during which the radar boresight was directly looking at the wake vortex (obtained from smoke data analysis).

The objective of plotting the spectral moments as a function of time along with the smoke video data is to be able to see if a consistent pattern emerges in any of the moments at times when the antenna is pointing directly at the wake vortex target. It is also of interest to note if and how this pattern is disrupted at times when the antenna boresight is not directly pointing at the wake vortex. Passes 44 and 135, both cross-axial scans, seem to offer the best chance of detection due to the extended period of time during which the antenna was pointing at the wake vortex. The only discernible pattern observed from the data after the aircraft has passed is the presence of alternating bands of positive and negative mean velocities, ranging between -1 to +1 m sec⁻¹. This pattern is consistent with predicted behavior for a radar observing a pair of vortices side-on. However, the data does not conclusively show detection of wake vortices for the following reasons:

- Range extent of alternating bands (~ 1 km) is much larger than the expected size of the wake from a C-130 (~ 25 m).
- There does not exist an associated broadening of the spectrum as seen from spectrum width plots.
- The pattern seems to persist even at times when the antenna is not directly pointing at the wake.

5.3 X-band Radar Performance Analysis

Since the analysis of the experimental data from the Wallops X-band radar failed to locate a wake vortex, the expected performance of the system was re-evaluated using

the actual values for transmitter power, system noise temperature, and waveguide losses that were encountered during the experiments.

The system noise temperature can be calculated from equation (5.11), where $T_s \equiv$ system noise temperature; $T_A \equiv$ Antenna noise temperature; $g_L \equiv$ gain of the lossy path from antenna flange to Collins R/T unit; $T_L \equiv$ noise temperature of the lossy path from antenna flange to Collins R/T unit; and $T_R \equiv$ noise temperature of the Collins R/T unit. Values of the parameters in equation (5.11) are given in Table 5-1.

$$T_s = T_A (g_L) + T_L + T_R \quad (5.11)$$

Table 5-1. Component Noise Temperatures and Gains for Wallops X-band Radar

Parameter	Value
T_A	100 °K
g_L	0.56 dB
T_L	$T_L = 290 (1-g_L) °K = 126.9 °K$
T_R	527.2 °K

Using the values in Table 5-2, the actual system noise temperature for the Wallops X-band Radar can be evaluated as

$$T_s = 100 (0.56) + 126.9 + 527.2 = 755.1 °K.$$

The waveguide losses can be computed from the sum of the losses in the transmitter path, L_T , and the losses in the receiver path, L_R . For the Wallops experiments, the actual losses in the transmitter path were 1.8 dB, and the actual losses in the receiver path were 2.5 dB. Thus,

$$\begin{aligned} L_{wg} &= L_T + L_R \\ L_{wg} &= 4.3 \text{ dB} \end{aligned} \quad (5.12)$$

The single pulse, signal-to-noise ratio equation from Section 2 can now be evaluated for the three pulse widths that were used in the field experiments—1.0 μ sec, 0.5 μ sec, and 0.25 μ sec.

$$\frac{S}{N} = \frac{\eta P_t G^2 \lambda^2 \theta^2 \frac{c\tau}{2} B_f}{R^2 (256\pi^2) kT_s BL_{wg}} \quad (2.1)$$

$$\tau = 1.0 \text{ } \mu\text{sec}: S - N = \eta - 20\log(R) + 183.1 \text{ (dB)}$$

$$\tau = 0.5 \text{ } \mu\text{sec}: S - N = \eta - 20\log(R) + 177.1 \text{ (dB)}$$

$$\tau = 0.25 \text{ } \mu\text{sec}: S - N = \eta - 20\log(R) + 171.1 \text{ (dB)}$$

Detection of wingtip-generated wake vortices in clear air requires S-N to be greater than or equal to 0 dB. Setting S-N equal to 0 and solving for η yields equations (5.13) through (5.15), which predict the minimum volume reflectivity required for detection at the 3 pulse widths available during the experiment.

$$\tau = 1.0 \text{ } \mu\text{sec}: \eta = 20\log(R) - 183.1 \text{ (dB m}^{-1}\text{)} \quad (5.13)$$

$$\tau = 0.5 \text{ } \mu\text{sec}: \eta = 20\log(R) - 177.1 \text{ (dB m}^{-1}\text{)} \quad (5.14)$$

$$\tau = 0.25 \text{ } \mu\text{sec}: \eta = 20\log(R) - 171.1 \text{ (dB m}^{-1}\text{)} \quad (5.15)$$

Figure 5-2 shows the minimum volume reflectivity required for detection of wake vortices in clear air as a function of range for the available pulse widths. The 0.25 μ sec curve shows that wake vortices would only be detectable at ranges between 400 and 700 meters. The detectable range interval for the 0.5 μ sec pulse is between 400 and 1300 meters, while the detectable range is between 400 and 2500 meters for the longest pulse—1.0 μ sec. This analysis is optimistic because it includes the assumption that the pulse volume is full of the highest volume reflectivity values expected for wake vortices. However, the high volume reflectivity values are found in a narrow band surrounding the entire wake and are far from the vortex cores. In addition, the larger the pulse width, the more likely the pulse volume will not be filled; this requires a beam fill correction which will further reduce the maximum range. A more realistic assumption is that the average reflectivity in a pulse volume observing wake vortices is approximately -130 dB m^{-1} . Under these circumstances, figure 5-2 indicates that wake vortex detection in clear air is highly improbable with the Wallops Island X-band Doppler radar.

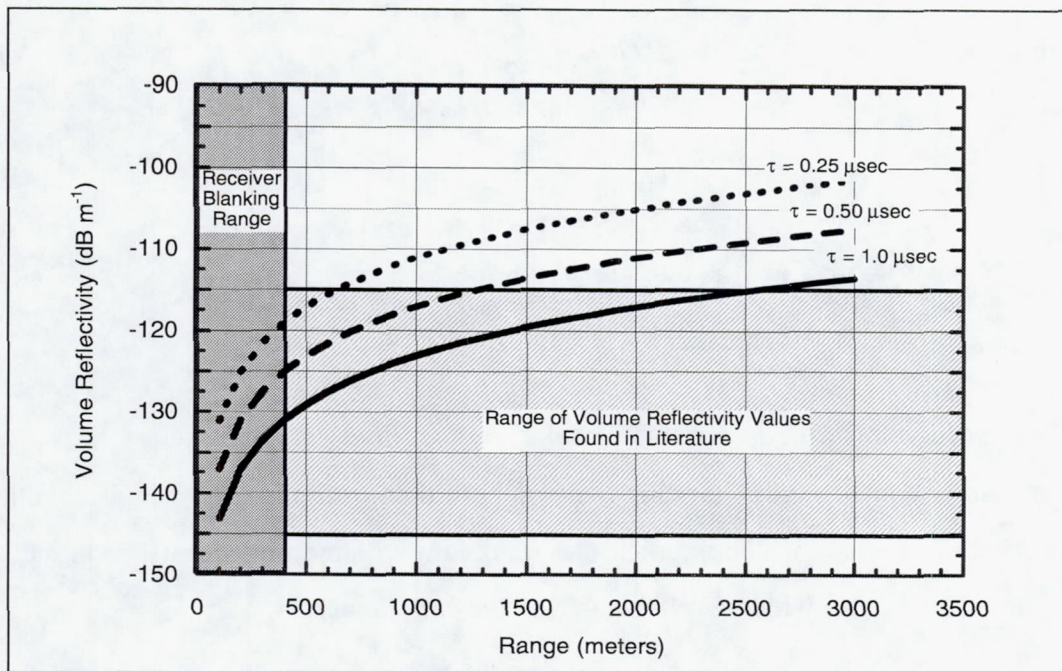


Figure 5-2. Minimum Volume Reflectivity Required for Detection of Wake Vortices in Clear Air for the Wallops Island X-band Doppler Radar. ($\tau \equiv$ pulse width)

In Table 5-2, some of the relevant data obtained from the meteorological measurements are placed side-by-side with some of the radar transmitter parameters. The meteorological measurements include the altitude at which the wake vortices were generated by the C-130 and the characteristic decay times. The radar parameters include the measurement mode of the radar, which was either Along-the-Track (ATT) or Cross-the-Track (CTT) of the flight path. The pulse duration of the transmitted pulse and the maximum range of the radar measurement—derived from the pulse duration—is also shown.

Due to the paucity of the data set (7 passes), it is not possible to draw any definitive conclusions concerning the ability of an X-band radar (9.3 GHz) to detect the presence of wake vortices in clear air. However, a few observations are offered with regards to these results. In six of the seven passes selected for post-processing, the radar was using the longer pulse widths, which corresponds to a maximum range of more than 1300 meters. The altitudes at which the vortices were released for these six passes were between 490 and 610 meters AGL, and the decay times were reasonably long—ranging from 70 seconds to several minutes. These conditions should have presented a reasonable

measurement "window" for the X-band radar if the signal-to-noise ratio had been as expected and if the radar had been truly aligned with the vortex core.

Table 5-2. Correlation of Meteorological Data with Radar Parameters

Date	Time (UTC)	Pass	Rollup Altitude (m)	Decay Time (sec)	Mode	Max Range (m)	Pulse Duration (τ)
1-10-95	1842	44	490	120	CTT	2500	0.96
1-10-95	2005	55	400	120	ATT	700	0.22
1-10-95	1932	97	610	70	ATT	1300	0.48
1-11-95	1647	116	<550	>300	ATT	2500	0.96
1-11-95	1721	122	<550	>300	ATT	2500	0.96
1-11-95	1733	124	<550	>300	ATT	1300	0.48
1-11-95	1856	135	610	70	ATT	1400	0.48

CTT = Cross – the – Track Measurement
ATT = Along – the – Track Measurement

Prior to the radar measurement, the pulse duration was set to one of three values: 0.25 (0.22) μ sec, 0.5 (0.48) μ sec , or 1.0 (0.96) μ sec. The pulse duration was varied in an attempt to optimize the interaction between the sampling volume of the radar pulse and the optimal values of the volume radar reflectivity within the core of the wake vortex. However, because of the paucity of data selected for post-processing, varying the pulse length added another level of uncertainty to the results of the data analysis.

6.0 CONCLUSIONS

Previously conducted simulation studies predicted that a high frequency cut-off for radar detection of wingtip-generated wake vortices existed in clear air. At the time this experiment was planned in 1994, the maximum frequency was predicted to be between 6 and 35 GHz. Three field experiments, which had been conducted prior to 1994, demonstrated that radars with wavelengths up to 5 cm (6 GHz) successfully detected wake vortices in clear air.

Since radars at X-band are Commercial-off-the-shelf (COTS) systems and X-band radars are in operation in most airports, it was intriguing to plan an experiment to demonstrate for the first time that an X-band radar could detect the presence of wake vortices in clear air. Therefore, the high risk, high payoff field experiment described in this report was conceived, planned and implemented. Despite extensive analysis of the relevant radar data, the presence of wake vortices was not detected during the experiment with the X-band (9.3 GHz) radar.

However, it would be inadvisable to conclude that an X-band radar is not capable of detecting wake vortices in clear air because the high frequency cut-off is lower than 9.3 GHz. Although the experiment was well conceived, planned, and executed, it was determined that several conditions existed which made the measurement not feasible. The primary factors which contributed to the lack of results are summarized below:

1. The single pulse signal-to-noise ratio (SNR) calculated for the actual field measurements with the X-band radar at Wallops Island for the three values of pulse duration was sufficiently degraded from the SNR estimated when the experiment was planned. Therefore, the detection of wake vortices in clear air was highly improbable with the X-band radar finally assembled at Wallops. The primary causes of the degradation of the SNR were the lower than expected peak power, the high sidelobe levels, the high clutter, a higher than expected noise temperature of the receiver, and greater than expected losses.
2. Although 200 passes of the C-130 were carried out, only seven of the passes were evaluated based upon the criteria developed in planning the experiment. In post data processing of the data, the criteria required that the range of the wake vortex

from the X-band radar measured by the smoke video analysis be correlated with the range of the volume resolution cell of the radar within the core of the vortex. The latter was estimated analytically. No real time data processing was available to guide the experimenters to assess the sensitivity of the measurement. The paucity of data which could be analyzed was discovered in the post processing of the data. Other anomalies with some of the ground-based instruments also obviated analysis of certain data sets. However, the seven data passes which were analyzed were insufficient to draw definitive conclusions for such a sensitive measurement.

However, the experiment procedure which was developed could have succeeded if the SNR with the X-band radar had met the original performance specifications. From this experiment, several conclusions were also derived on the measurement process.

- The meteorological measurements which were taken were adequate to provide the information to an experiment director to set an appropriate flight path and altitude of a large transport aircraft.
- The smoke analysis and video camera techniques used to measure the range of the wake vortices from generation to decay had sufficient precision to point the radar at the location of the wake vortices. In general, the procedures planned and implemented had the potential to provide a successful measurement if the SNR was sufficiently high.

In summary, the seven passes that were analyzed accounted for less than 3 percent of the data which was collected. However, this was part of the high risk undertaken by the researchers; this plan minimized cost and schedule by utilizing existing instruments and a methodology to detect vortices in post-processing analysis. Because X-band radars are Commercial-Off-The-Shelf (COTS) systems used at all major airports, the high payoff would have occurred if the results could have conclusively shown that an X-band radar could detect wake vortices in clear air.

Finally, some “Lessons Learned” can be derived from this field experiment:

1. Although the experiment was well conceived and well planned, a “dry run” should have been conducted prior to launching the major campaign. The results from the

“dry run” should have been analyzed to verify the calibration, transmitter power, and SNR of the X-band (9.3 GHz) radar.

2. Real-time processing can be invaluable in assisting the experimenters in making appropriate changes in the experiment to optimize success of the experiment. In lieu of real-time processing, intervals of time should be provided to analyze the available data in detail prior to taking the next step in the experiment.
3. In this type of experiment, automated alignment of the radar antenna is extremely important. Every attempt should be made in future experiments to ensure precise alignment of the antenna boresight in the core of the wake vortex.

REFERENCES

- Chadwick, R. B., J. Jordan, and T. Detman, 1983. Radar Detection of Wingtip Vortices. Ninth Conference on Aerospace and Aeronautical Meteorology, AMS.
- Cohn, S. A., 1994. Investigations of the Wavelength Dependence of Radar Backscatter from Atmospheric Turbulence. *Journal of Atmospheric and Oceanic Technology*, **11**:2, pp.225-238.
- Cohn, S. A., 1991. Near Simultaneous Observations of Clear Air Turbulence with UHF, L-band, and X-band Radars at Millstone Hill. 25th International Conference on Radar Meteorology, June 24-28, Paris, France.
- Doviak, R. J., and D. S. Zrnic, 1984. Doppler Radar and Weather Observations. Academic Press. pp. 58-59.
- Doviak, R. J. and D.S. Zrnic, 1993. Doppler Radar and Weather Observations, Chapter 6. Academic Press.
- Gilson, W. H., 1992. Radar Measurements of Aircraft Wakes. Project Report AAW-11, Lincoln Laboratory.
- Hinton, D. A., 1995. Aircraft Vortex Spacing System (AVOSS) Conceptual Design. NASA Technical Memorandum 110184, NASA Langley Research Center.
- Lenschow, D. H., 1986. Probing the Atmospheric Boundary Layer. AMS. pp. 179-180.
- Mackenzie, A., 1997. Measured Changes in C-band Radar Reflectivity of Clear Air Due to Aircraft Wake Vortices. NASA Technical Paper 3671. NASA Langley Research Center.
- Marshall, R. E., W. Scales, and T. Myers, 1997. Wake Vortex Radar Reflectivity. Technical Memorandum RTI/4500/041-03S-R, Research Triangle Institute.
- Nespor, J. D., B. Hudson, R. L. Stegall, and J. E. Freedman, 1991. Doppler Radar Detection of Vortex Hazard Indicators. Proceedings of the Aircraft Wake Vortices Conference, DOT, Washington, D. C.
- Passarelli, R. E., P. Romanik, S. G. Geotis, and A. D. Siggia, 1981. Ground Clutter Rejection in Frequency Domain. Preprints, 20th Conf. Radar Meteorology, Boston. pp. 295-300.

Schaffner, P., M. Richards., W. Jones, and L. Crittenden, 1992. NASA Experimental Airborne Doppler Radar and Real Time Processor for Wind Shear Detection. Proceedings of the Fourth Combined Manufacturers' and Technologists' Conference on Airborne Wind Shear Detection and Warning Systems. NASA Conference Publication 10105, DOT/FAA/RD-92/19-II.

Sorjan, Z., 1989. Structure of the Atmospheric Boundary Layer. Prentice Hall, p.35.

Urkowitz, H. and J. D. Nespor, 1992. Obtaining Spectral Moments by Discrete Fourier Transform with Noise Removal in Radar Meteorology. IGARSS92, pp. 12-14.

Welch, P. D., 1967. The Use of Fast Fourier Transforms for the Estimation of Power Spectra: A Method Based on Time Averaging Over Short, Modified Periodograms. IEEE Trans. Audio Electroacoust. AU-15, pp. 70-73.

GLOSSARY

AGL	Above Ground Level
ASL	Above Sea Level
AS	Vortices Move At Value of Abscissa
azm	azimuth angle (deg)
C_n^2	Refractive Index Structure Constant ($m^{-2/3}$) $10 \times \log[Cn2]$ (dB $m^{-2/3}$)
C-band	4 to 8 GHz
C/N	Clutter Power to Noise Power Ratio
dB	decibel = $10 \times \log$ (power ratio)
DFT	Discrete Fourier Transform
elev	elevation angle (deg)
g	grams
GHz	1×10^9 Hz
η	Volume Reflectivity (m^2/m^3) $10 \times \log[h]$ (dB m^{-1})
I	Inphase Component of Received Signal
kg	kilograms
km	kilometers
kW	kilowatt
λ	Wavelength (meters)
M	Length of Segment of Time Series
μ sec	microsecond
N	Length of Time Series
p	Number of Time Series Segments
PRF	pulse repetition frequency
Q	Quadrature Phase Component of Received Signal
R	Range
Se	Vortices Separate
smk	smoke detected in antenna boresight camera
S/N	Signal Power to Noise Power Ratio
St	Upwind Vortex Stall
τ	Transmitter Pulse Width
T_s	Pulse Repetition Period (sec)
TV	Television
VCR	Video cassette recorder
W	Water Vapor Mixing Ratio ($kg \ kg^{-1}$)
W	Watts
WSW	Weighted Spectrum Width
X-band	8 to 12 GHz

APPENDIX

The following table correlates the contents of the figures in this appendix with the seven aircraft passes that were analyzed in this report.

Table A-1. Index to Figures in Appendix A

Pass Number	44	55	97	116	122	124	135
Fig. Number	A-1 - A-6	A-7 - A-11	A-12 - A-14	A-15 - A-20	A-21 - A-24	A-25 - A-28	A-29 - A-34

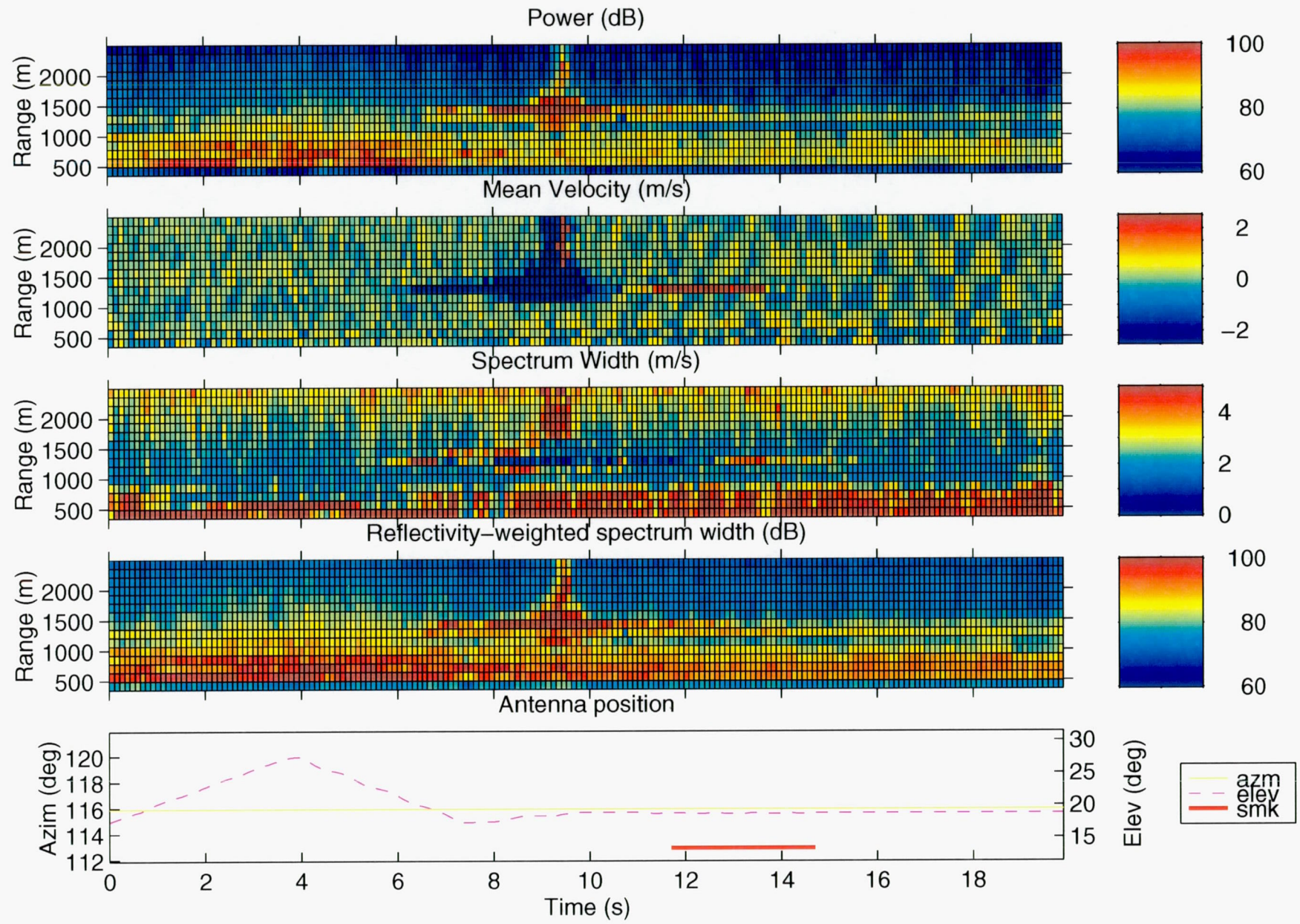


Figure A-1. Pass 44, start time: 18:42:30.

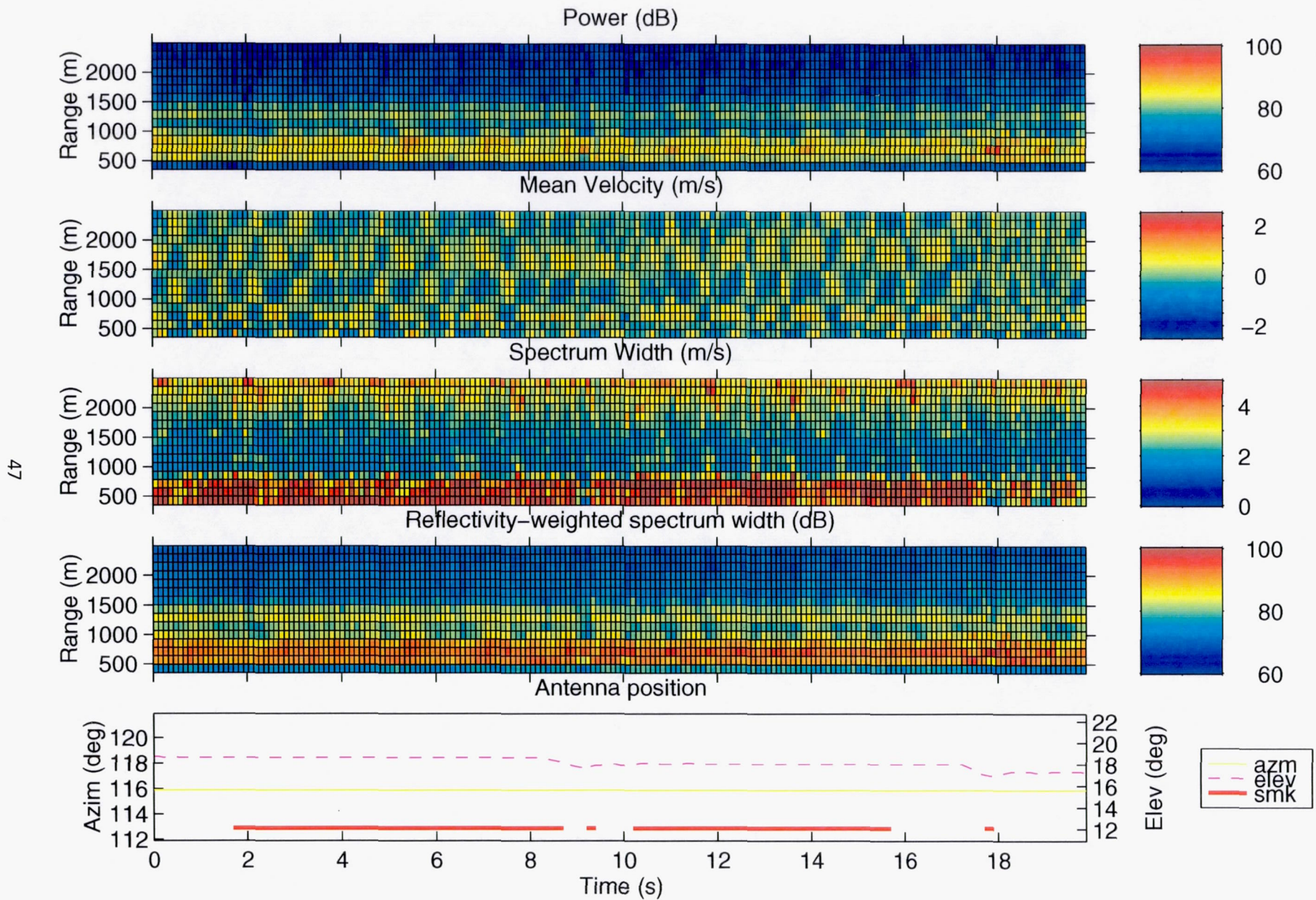


Figure A-2. Pass 44, start time: 18:42:50.

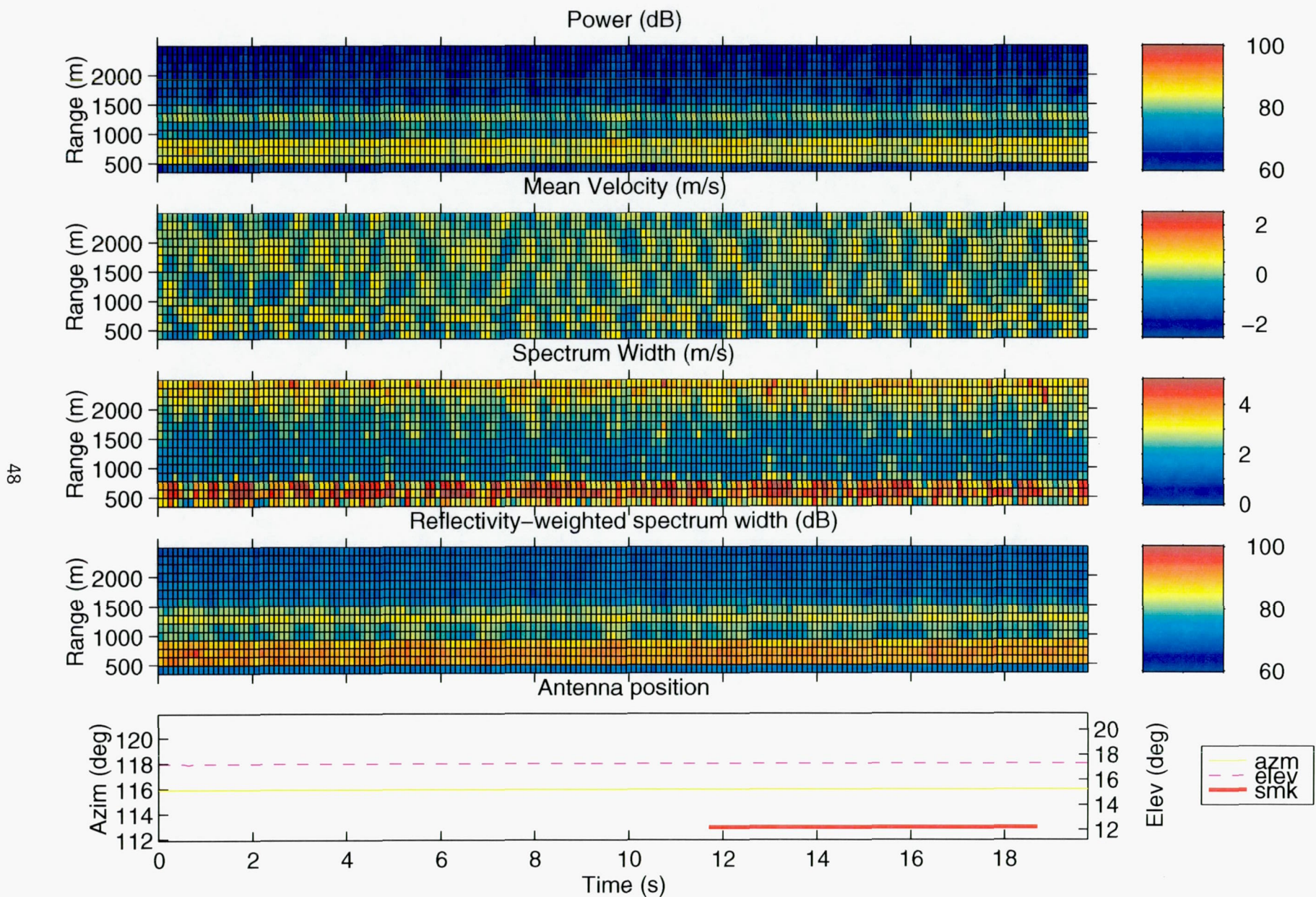


Figure A-3. Pass 44, start time: 18:43:10

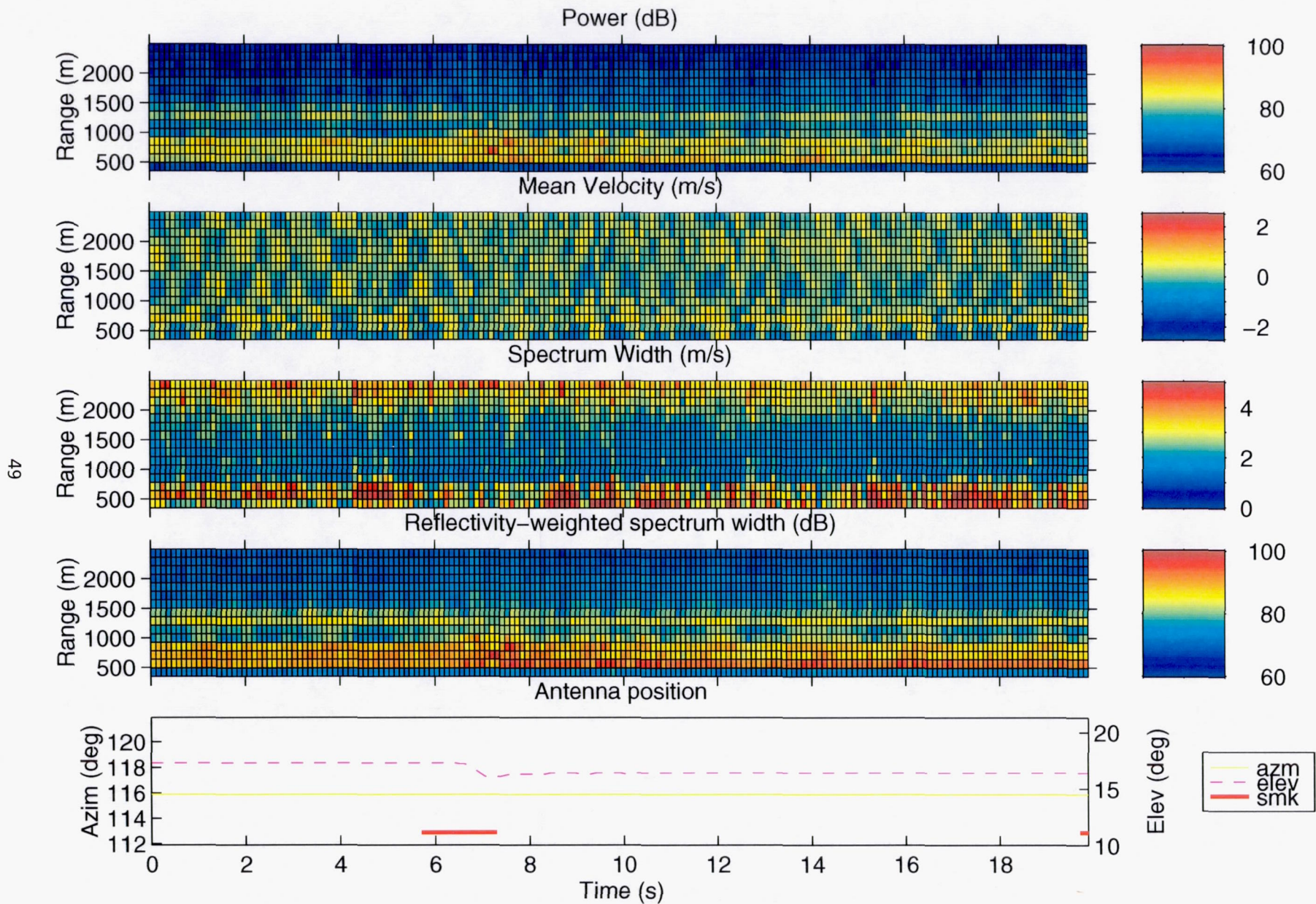


Figure: A-4. Pass 44, start time: 18:43:30.

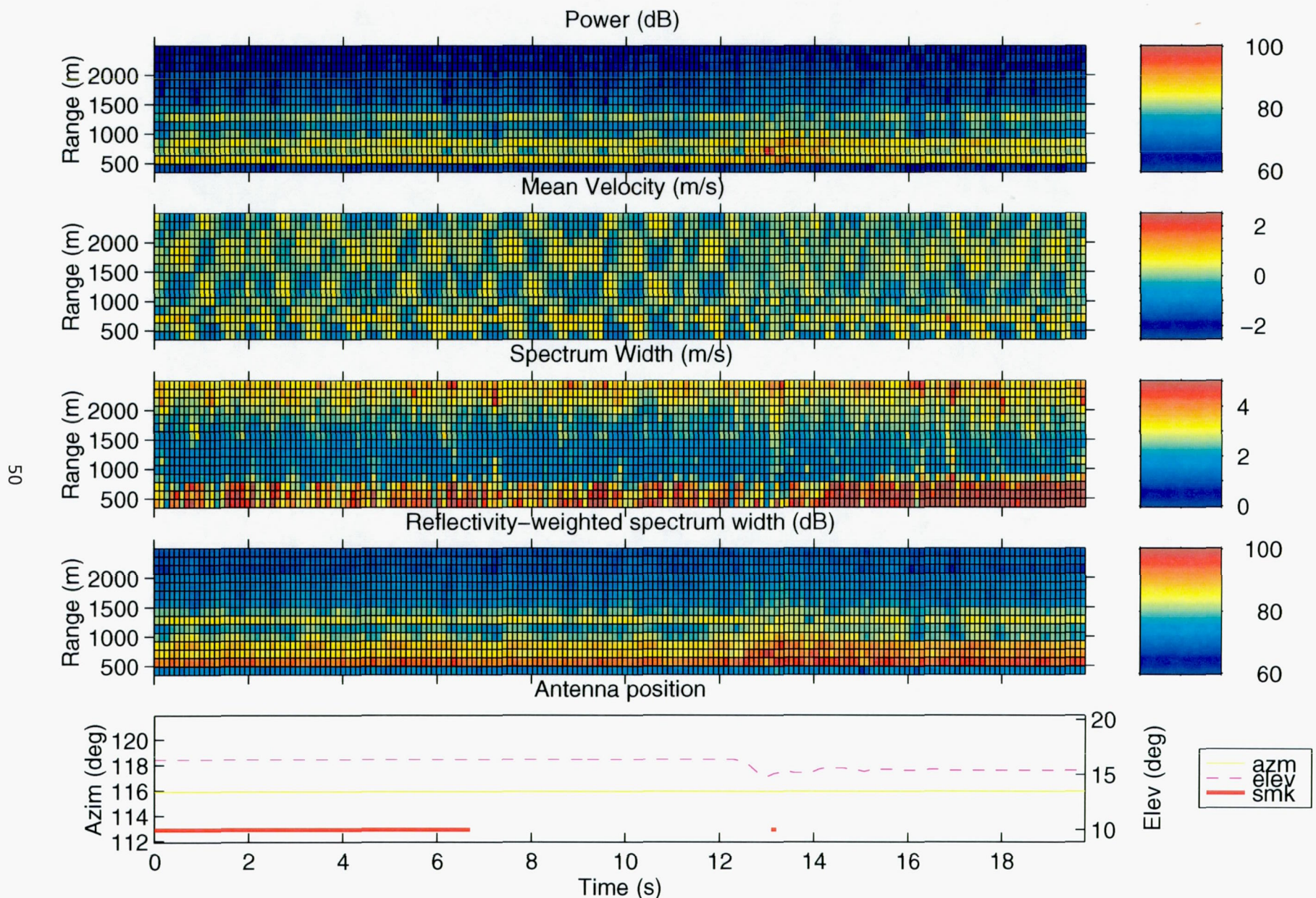


Figure A-5. Pass 44, start time: 18:43:50.

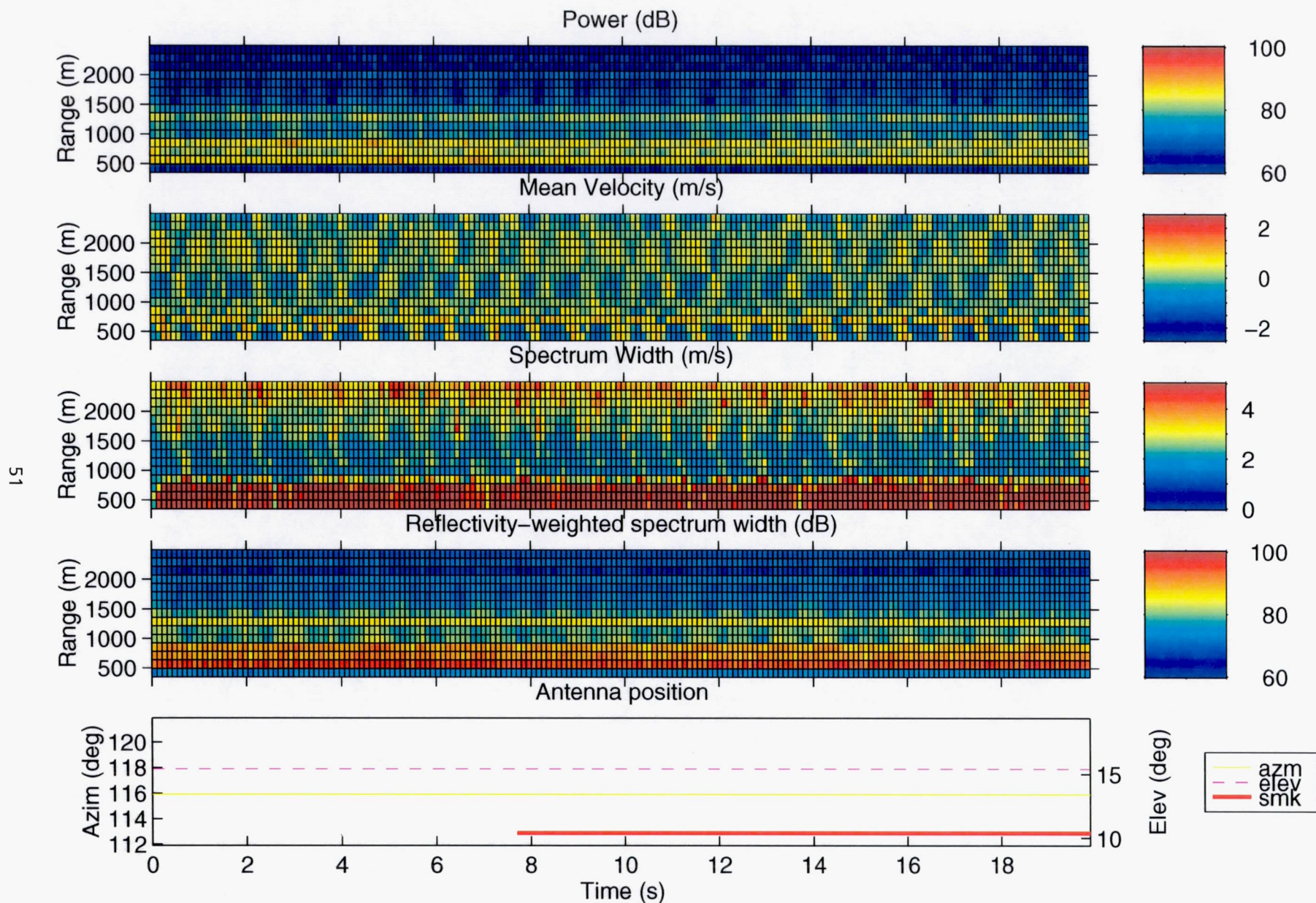


Figure A–6. Pass 44, start time: 18:44:10.

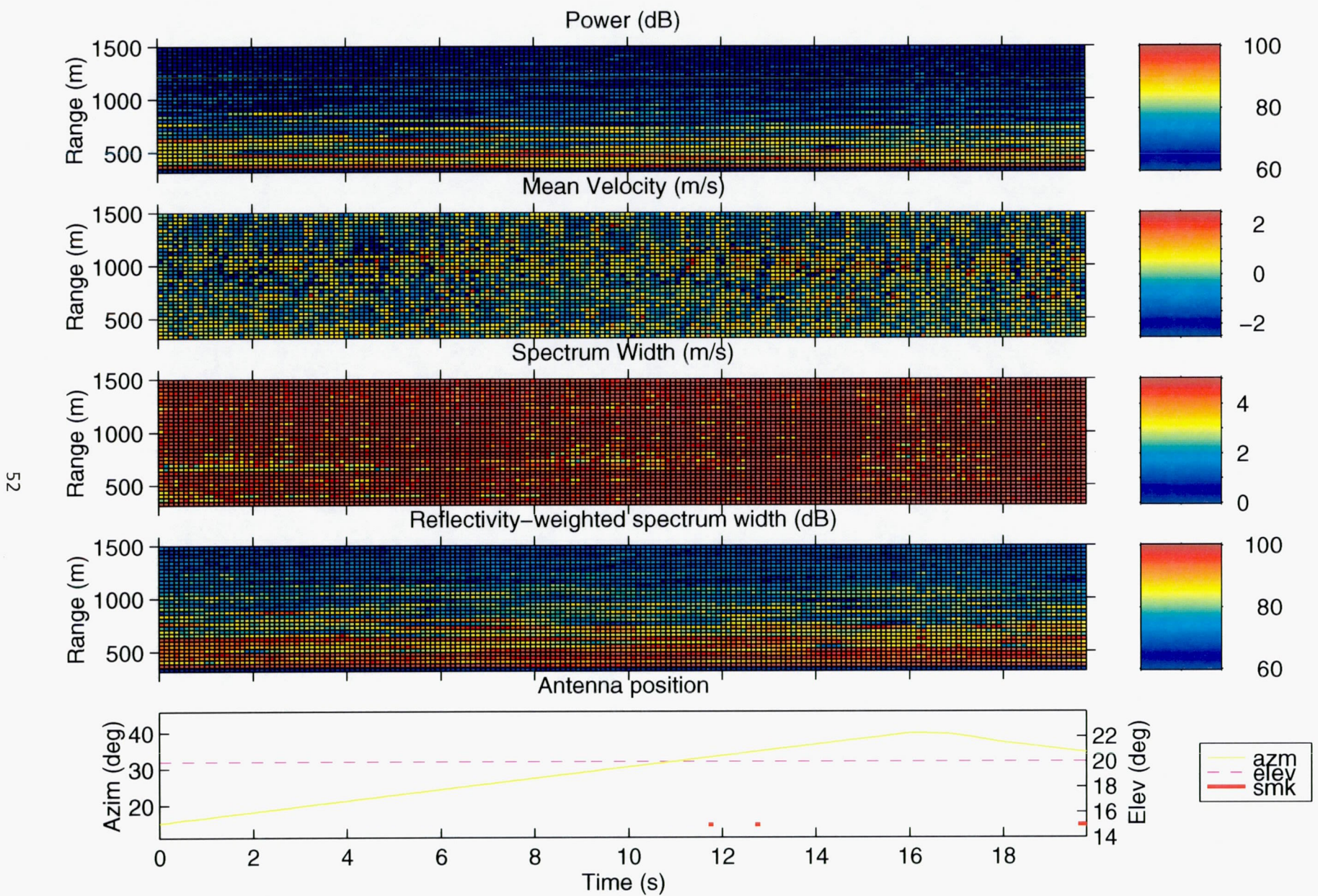


Figure A-7. Pass 55, start time: 20:05:00.

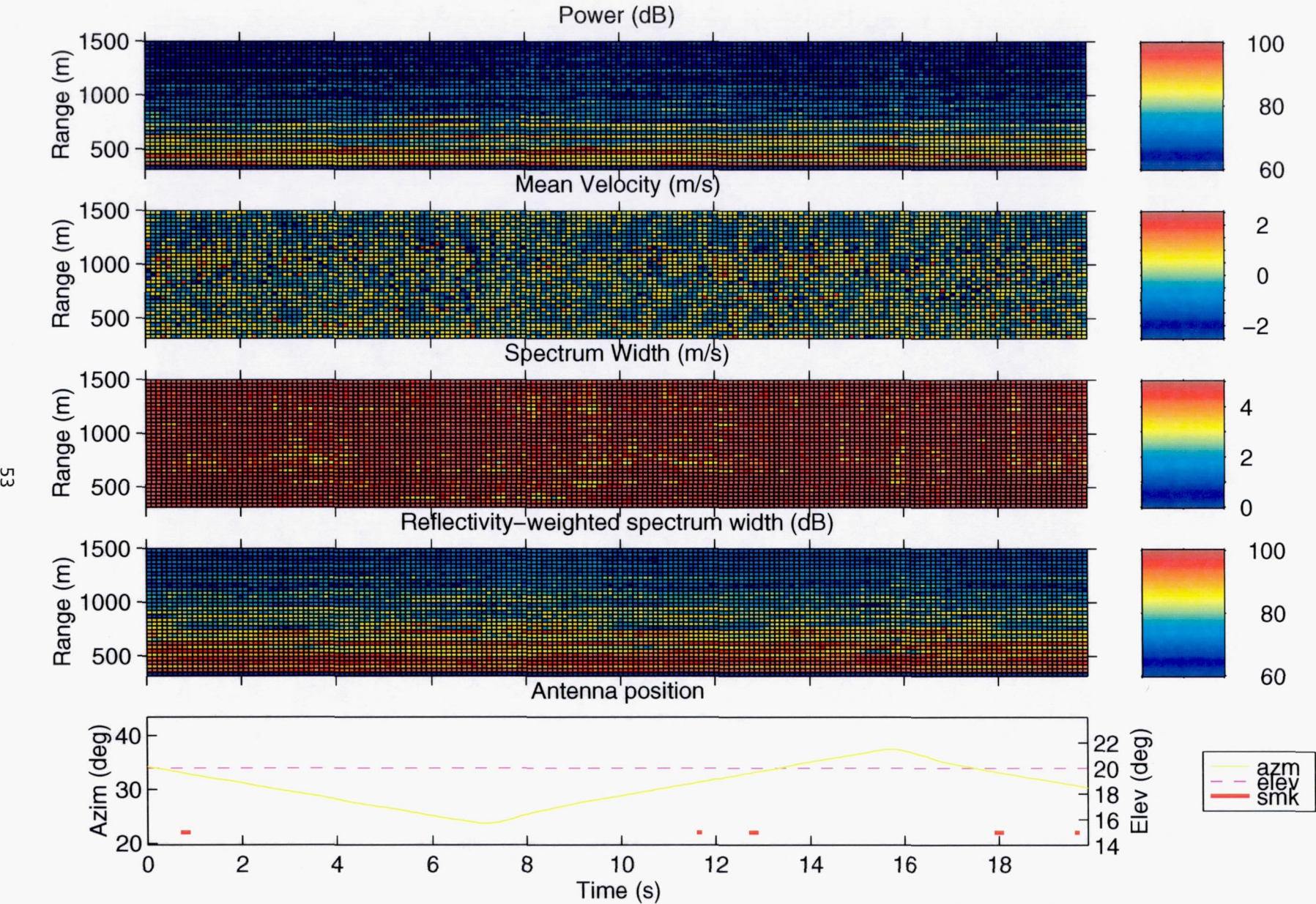


Figure A-8. Pass 55, start time: 20:05:20.

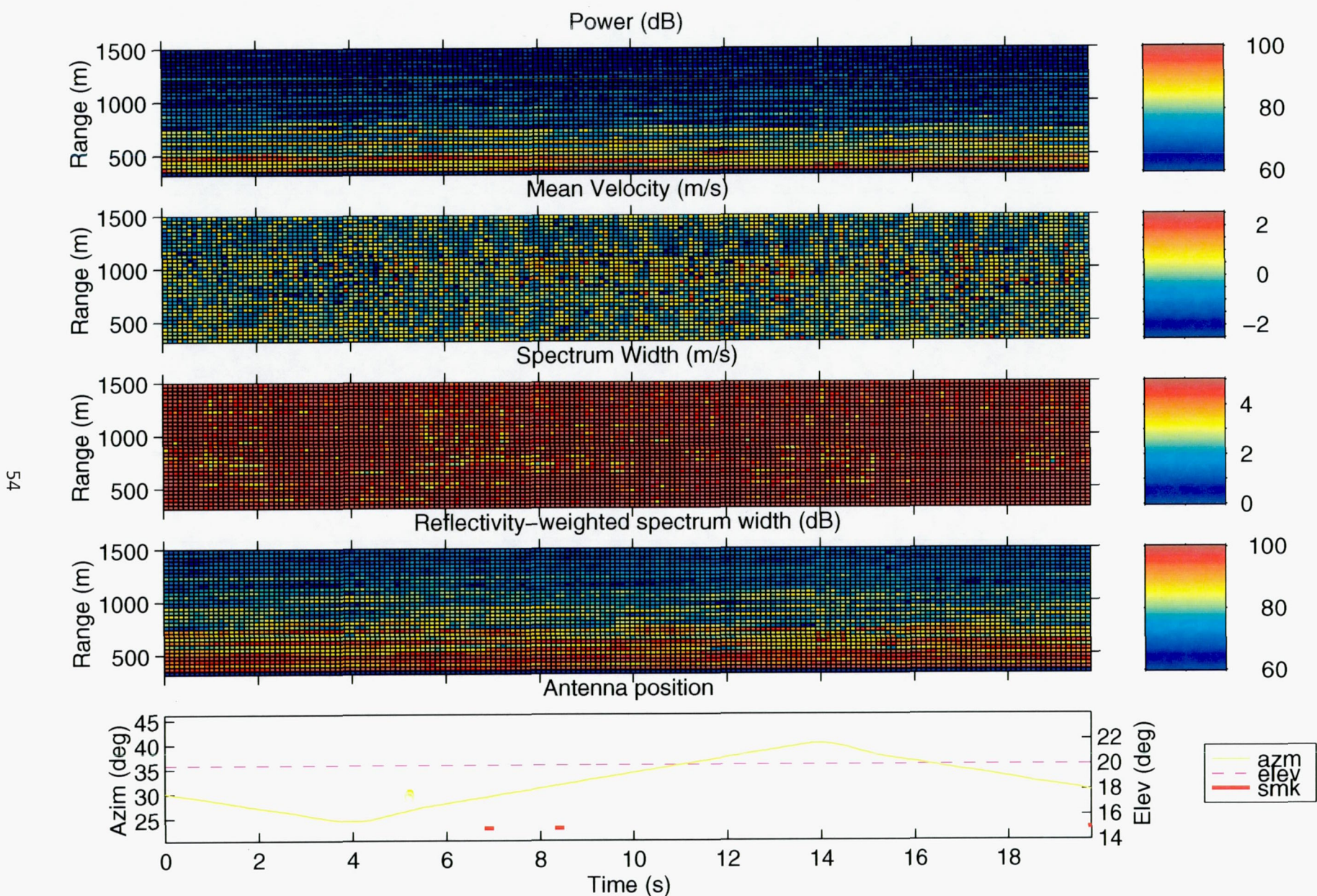


Figure A-9. Pass 55, start time: 20:05:40.

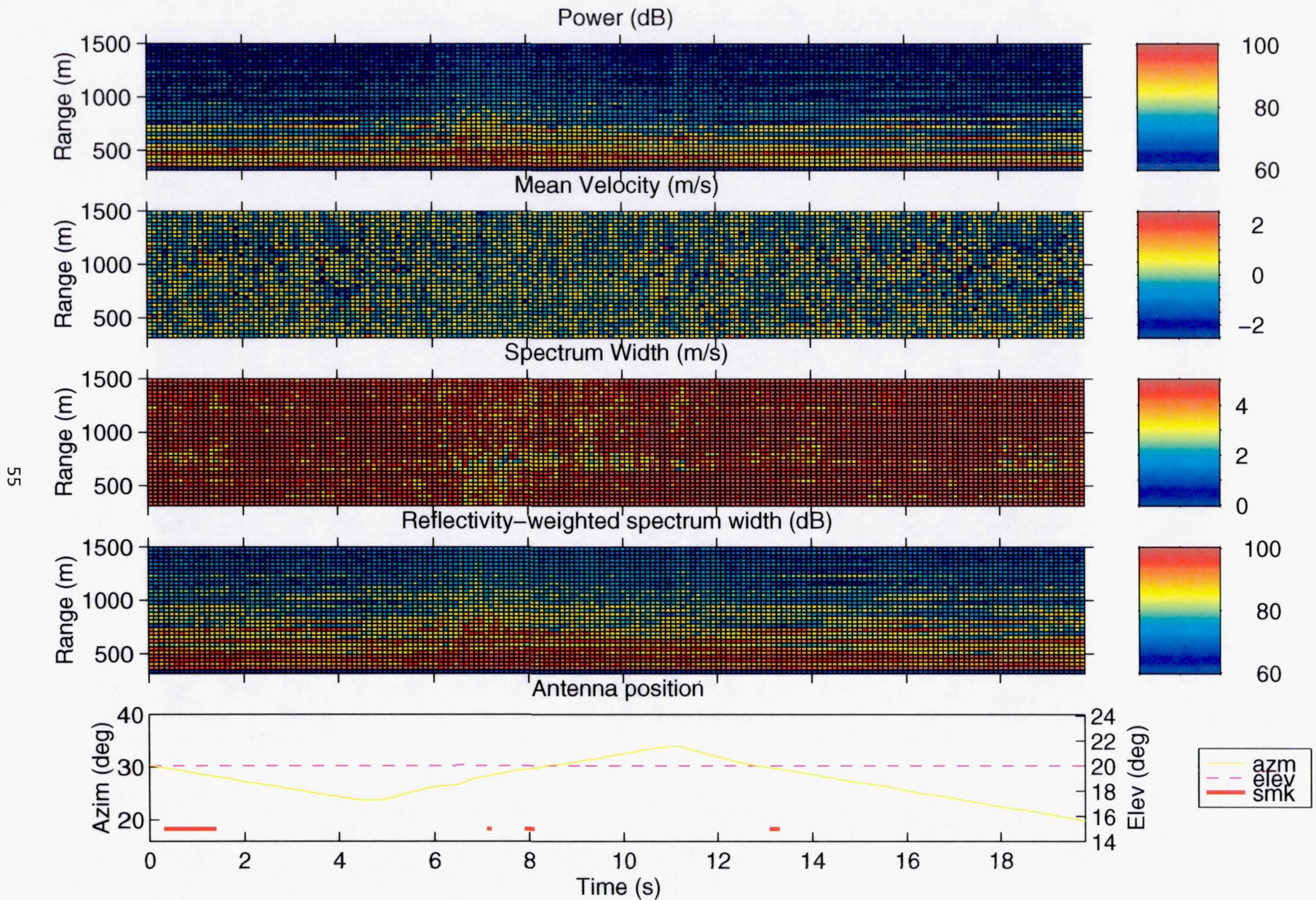


Figure A-10. Pass 55, start time: 20:06:00.

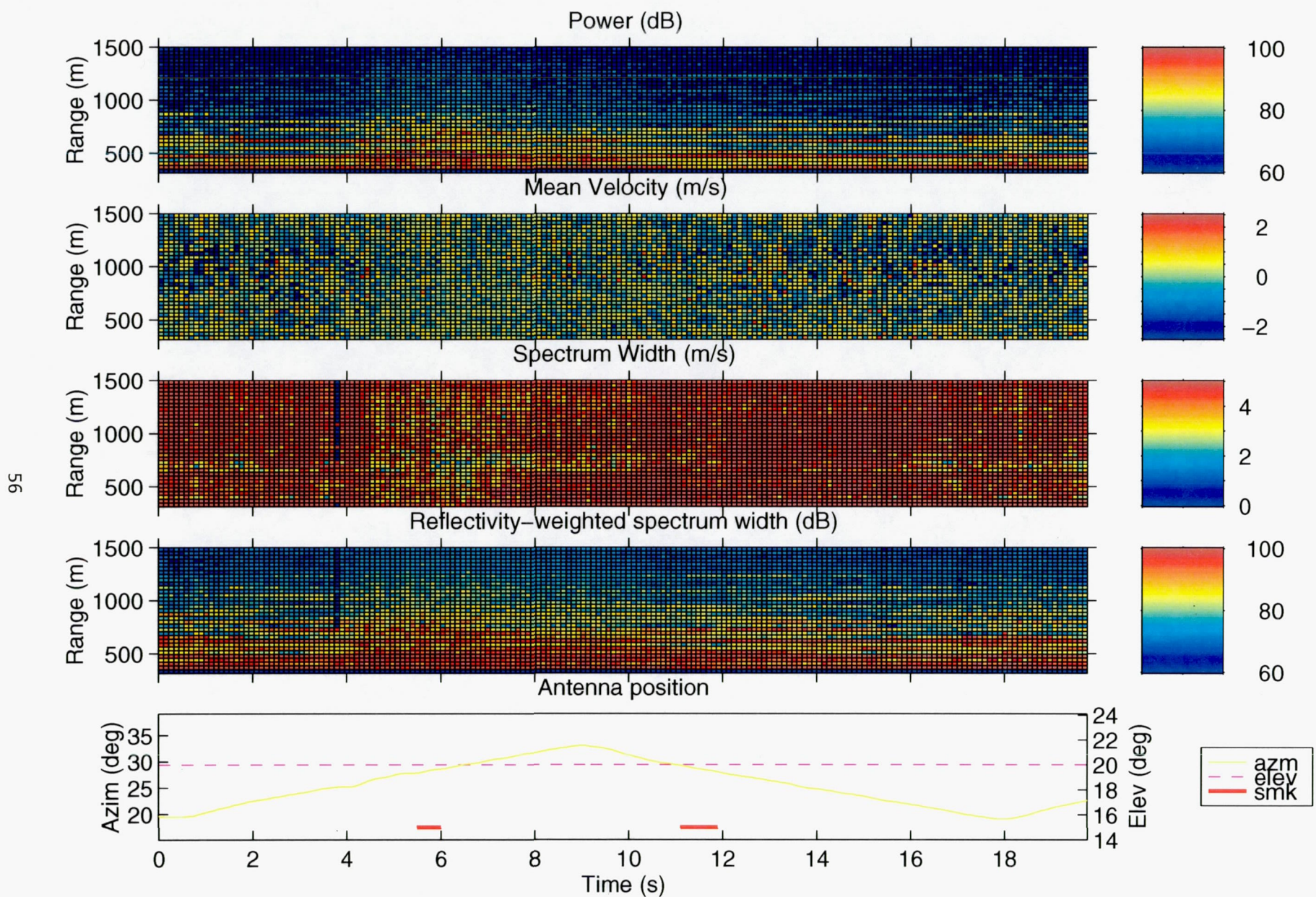


Figure A-11. Pass 55, start time: 20:06:20.

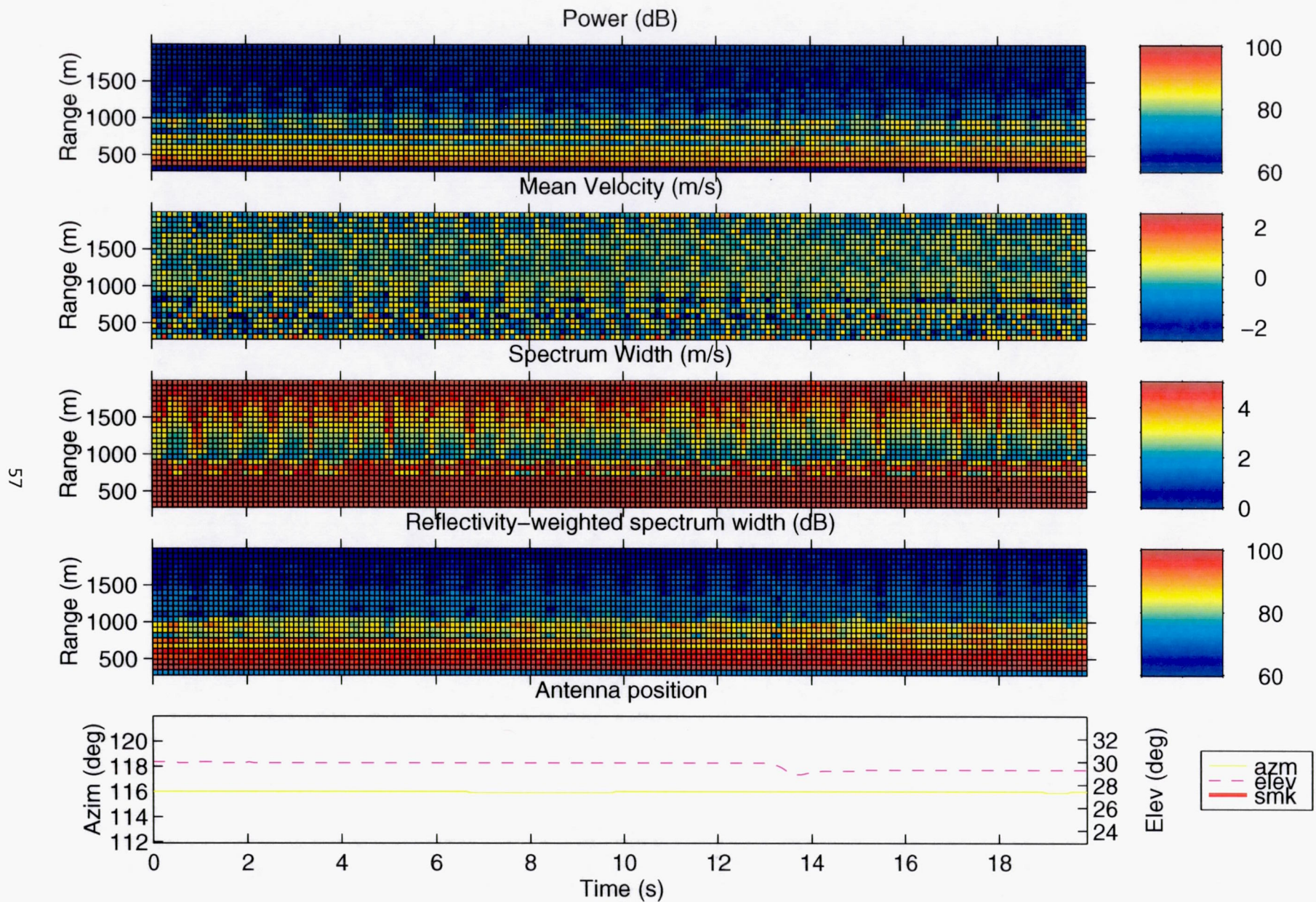


Figure A-12. Pass 97, start time: 19:32:00.

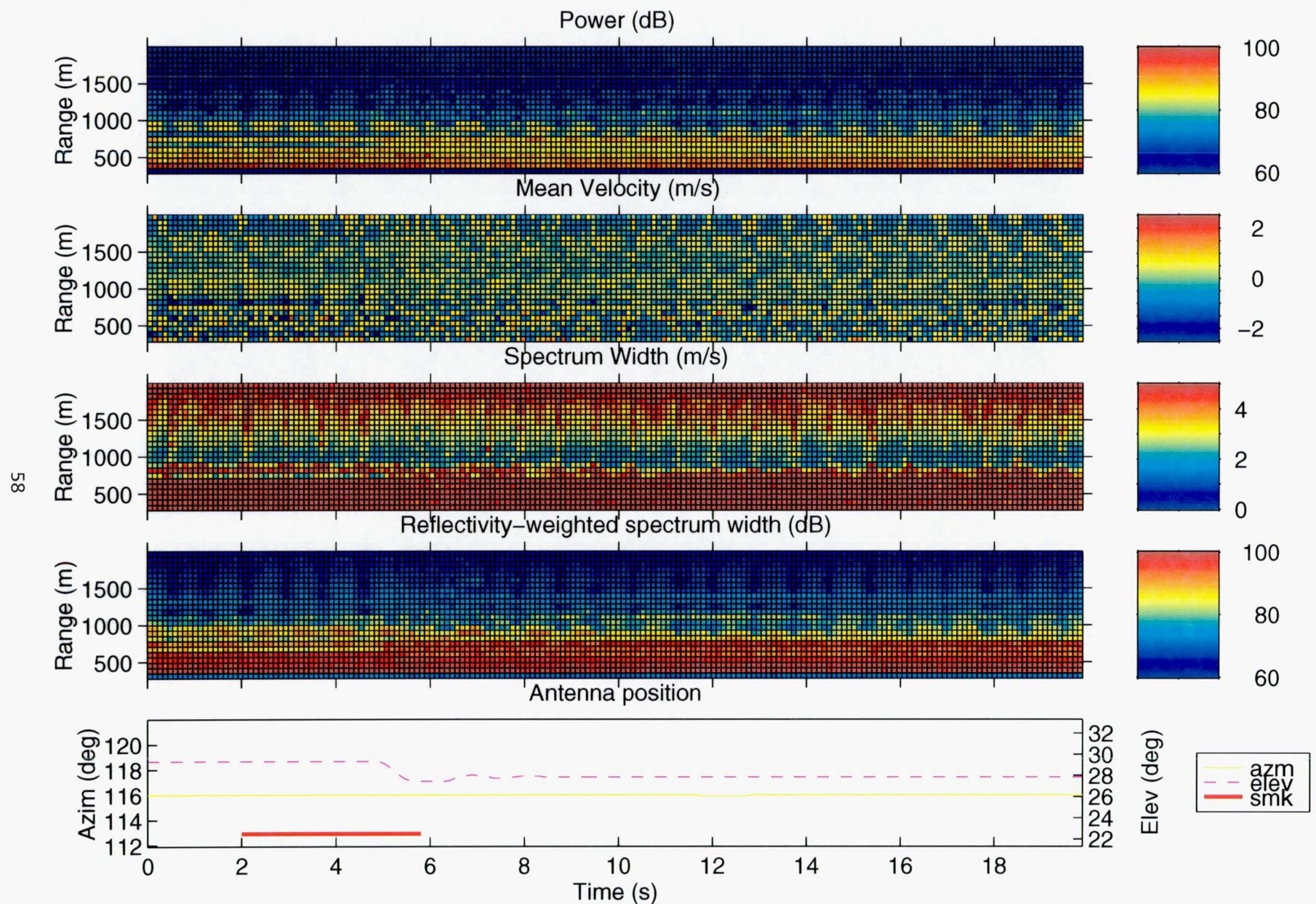


Figure A-13. Pass 97, start time: 19:32:20.

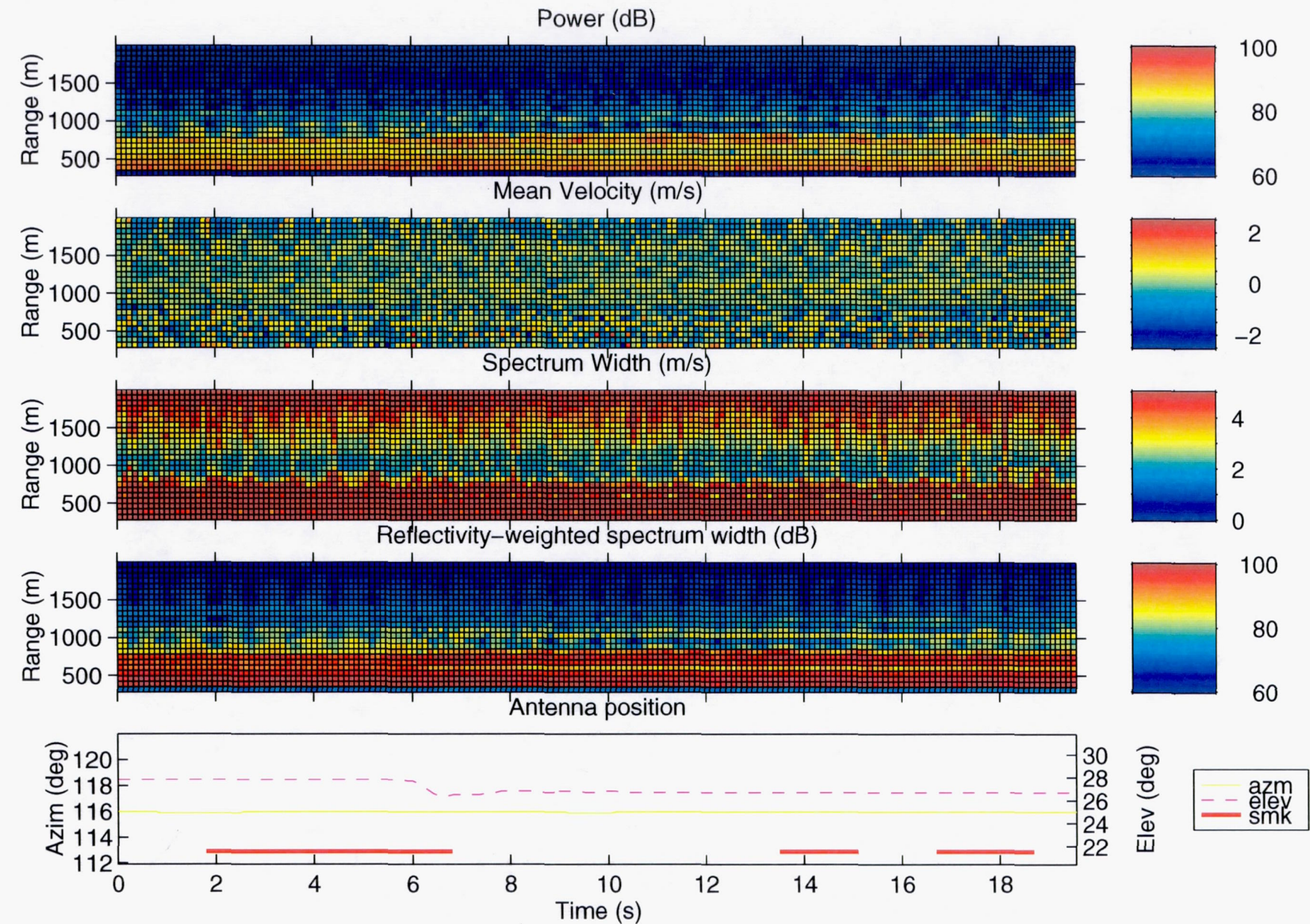


Figure A-14. Pass 97, start time: 19:32:40.

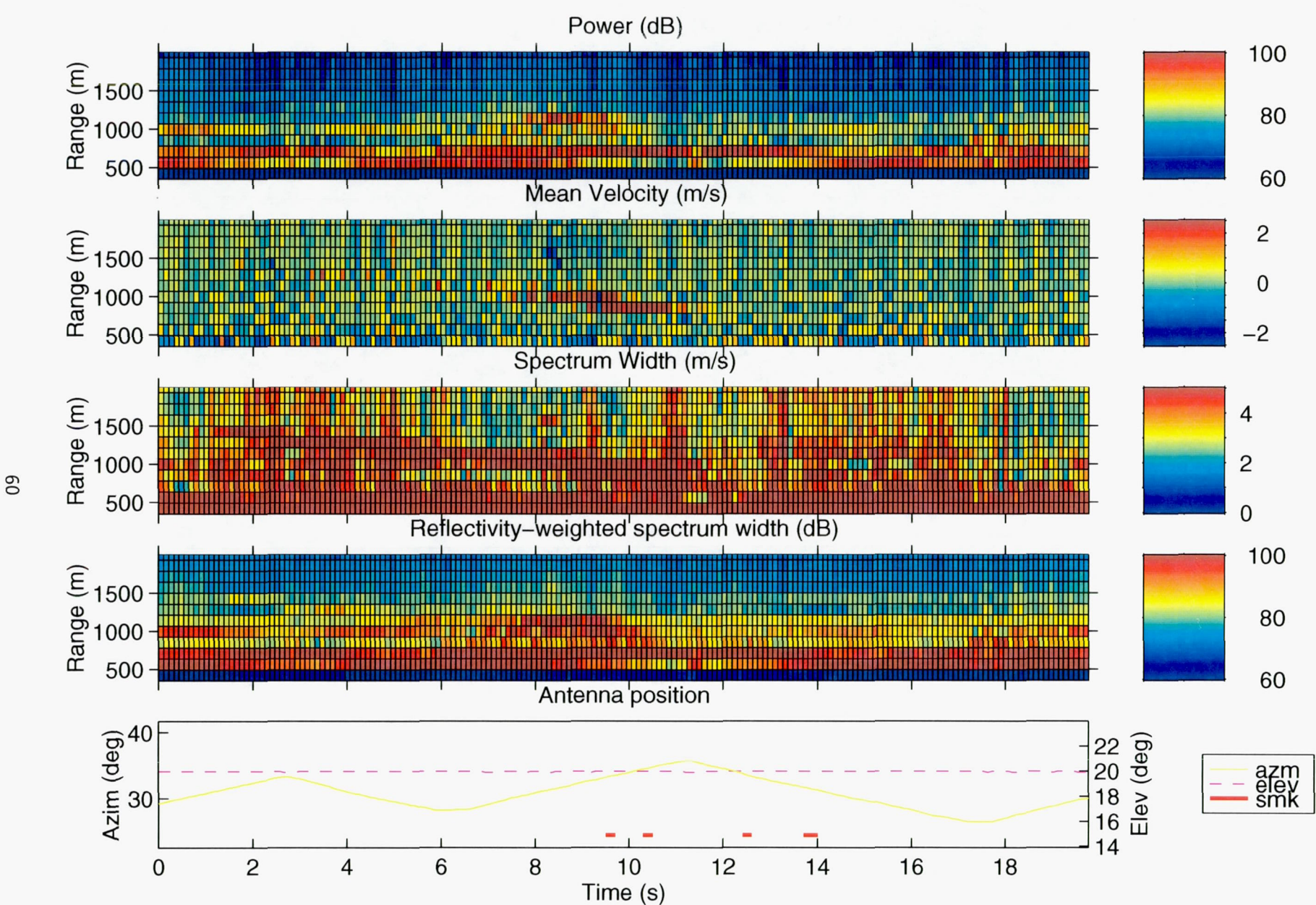


Figure A-15. Pass 116, start time: 16:47:40.

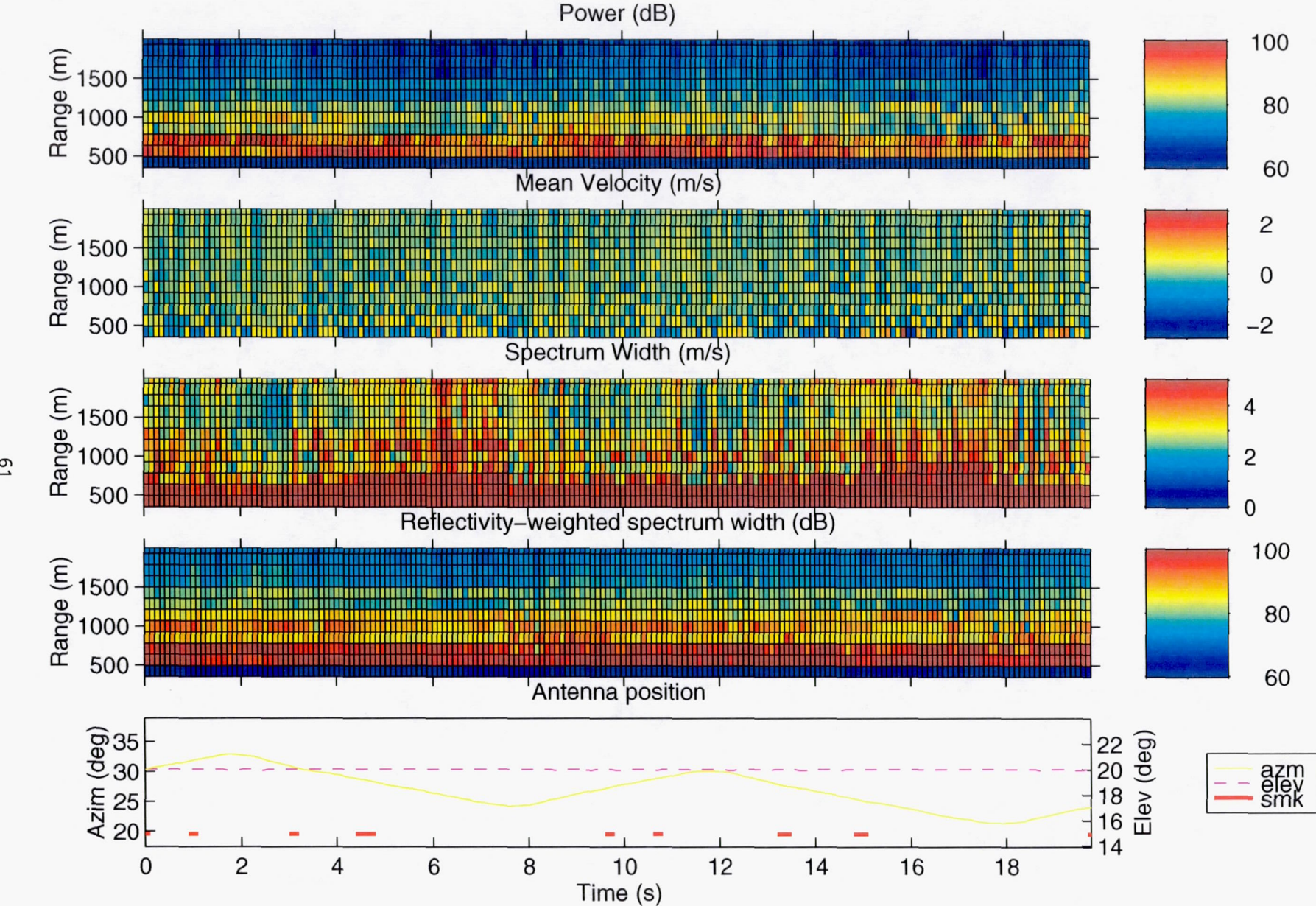


Figure A-16. Pass 116, start time: 16:48:00.

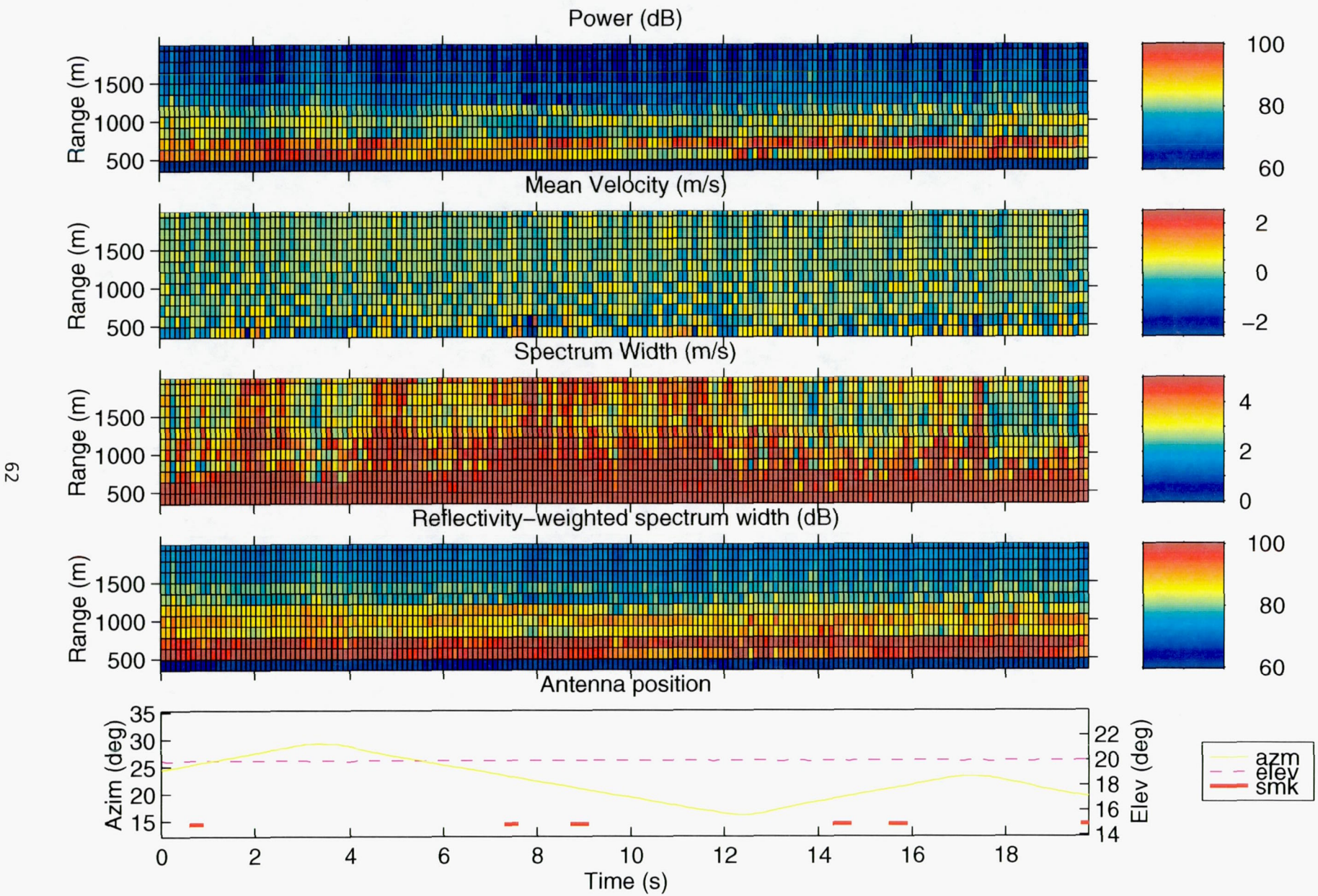


Figure A-17. Pass 116, start time: 16:48:20.

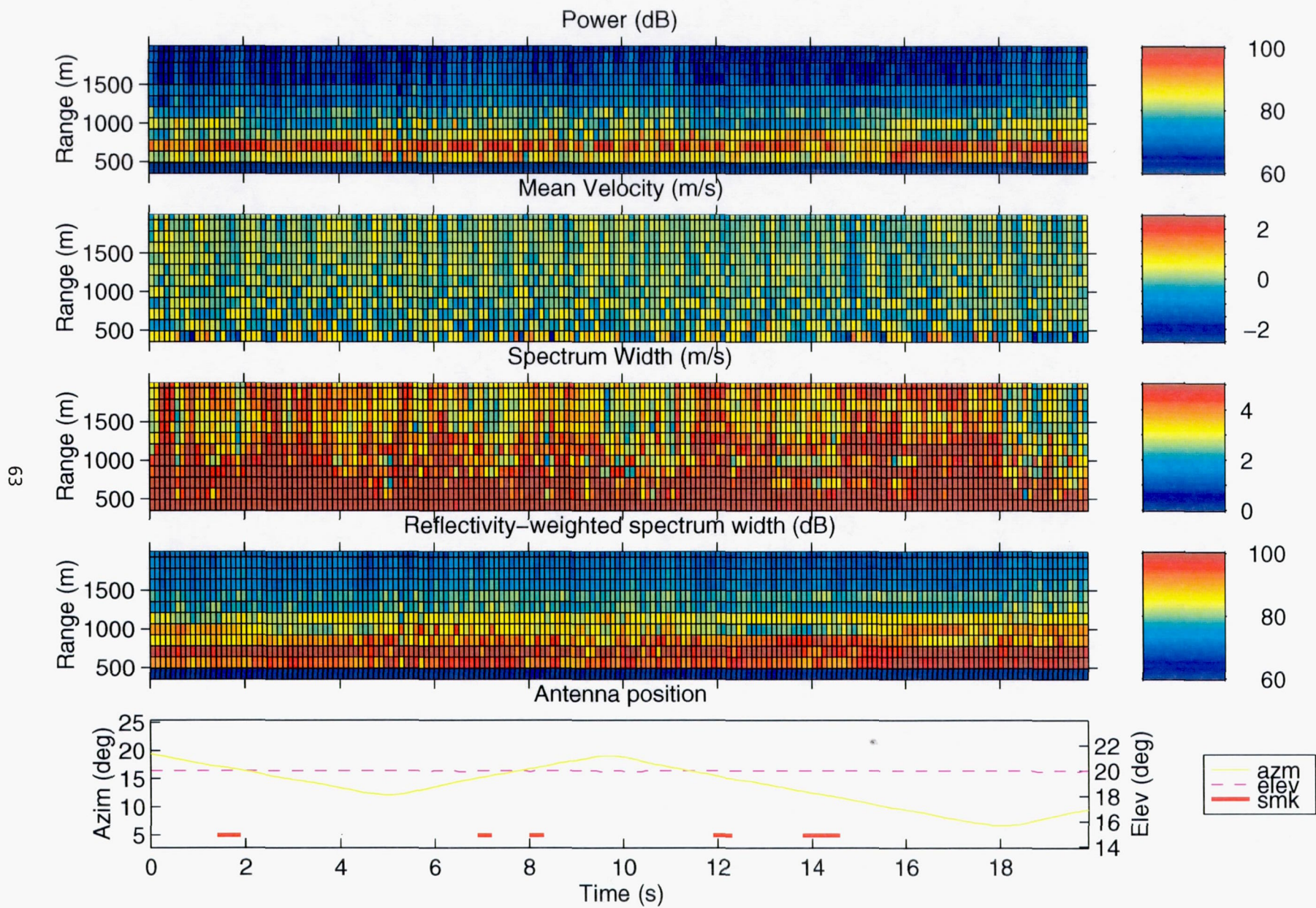


Figure A-18. Pass 116, start time: 16:48:40.

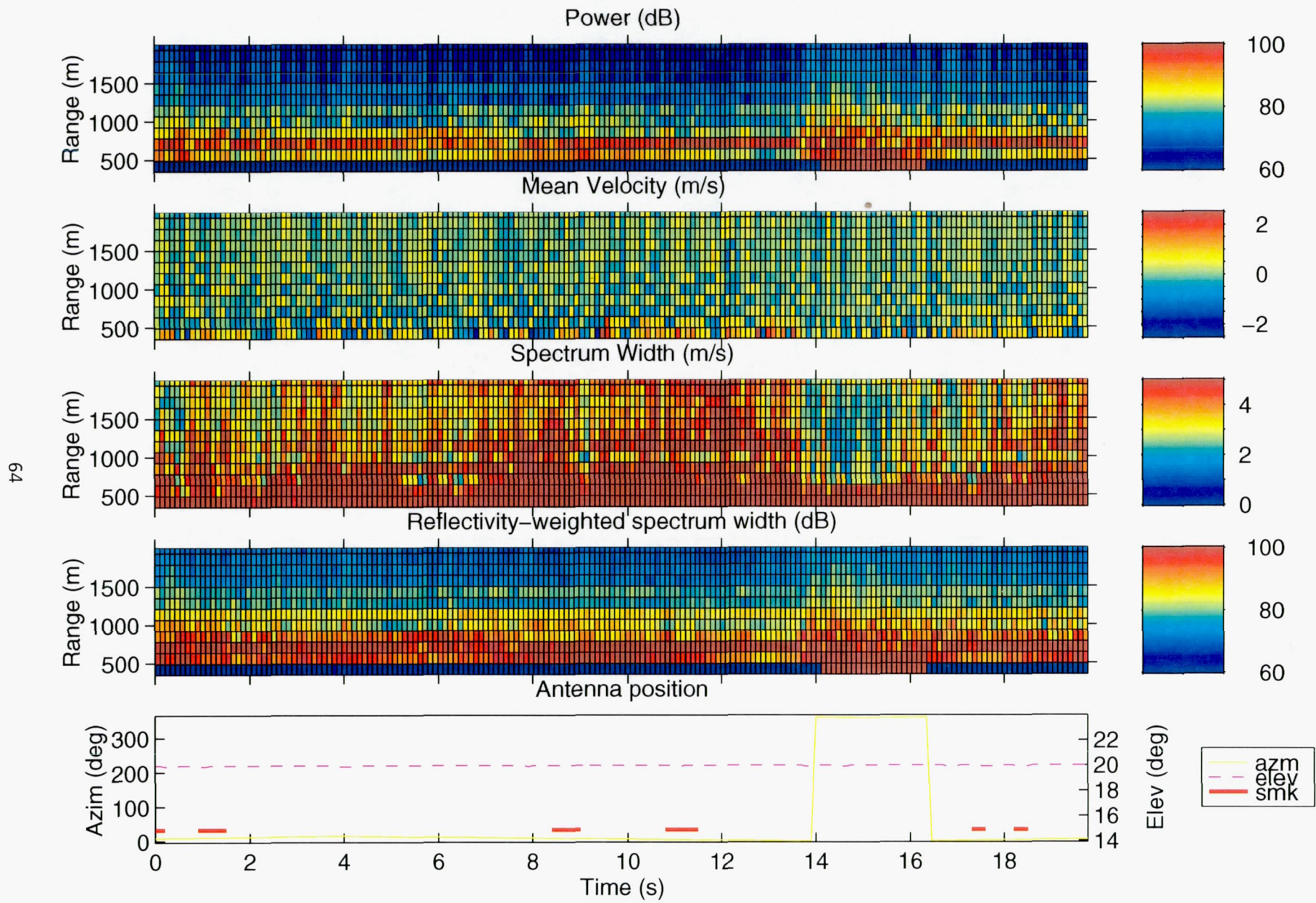


Figure A-19. Pass 116, start time: 16:49:00.

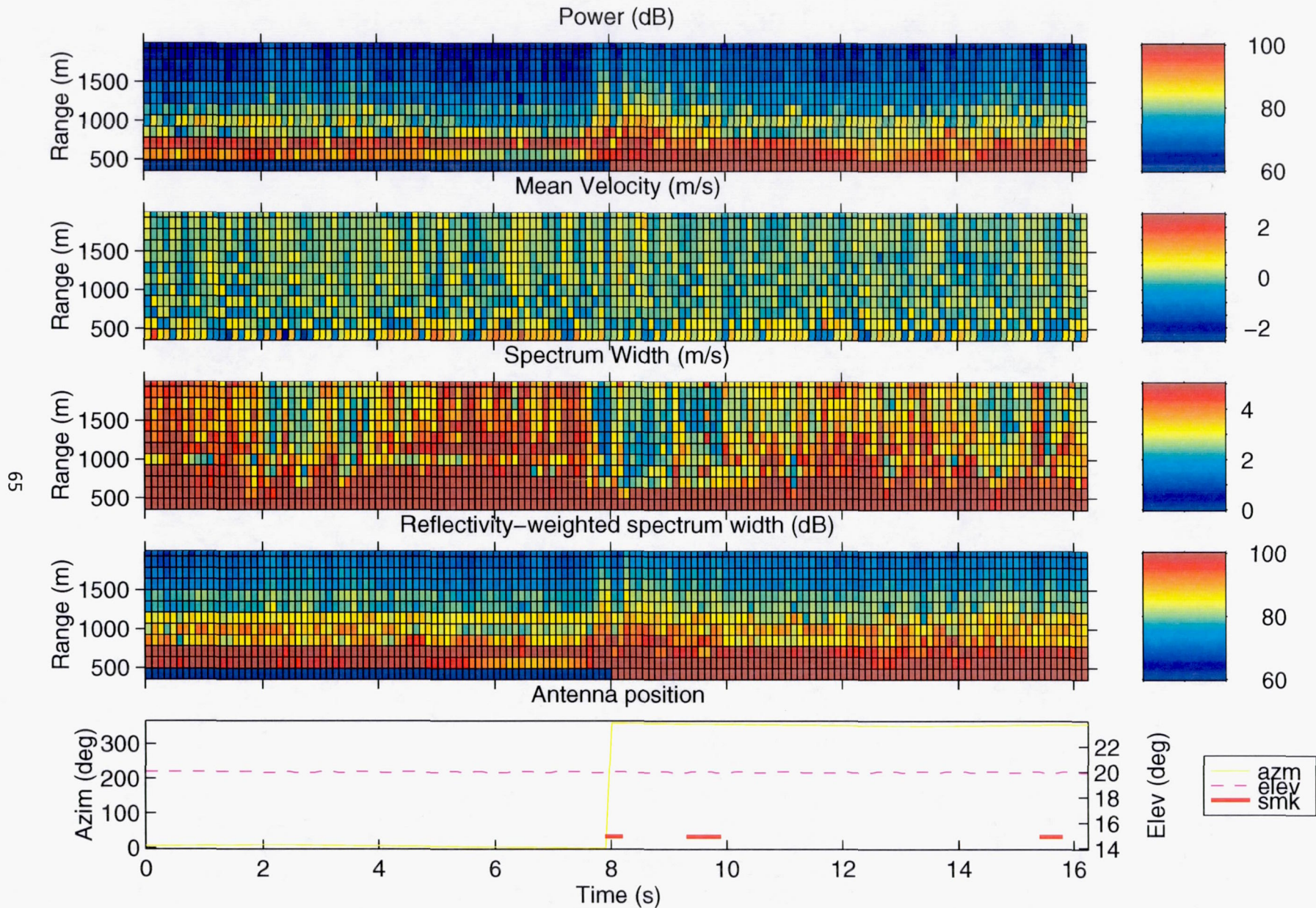


Figure A–20. Pass 116, start time: 16:49:20.

99

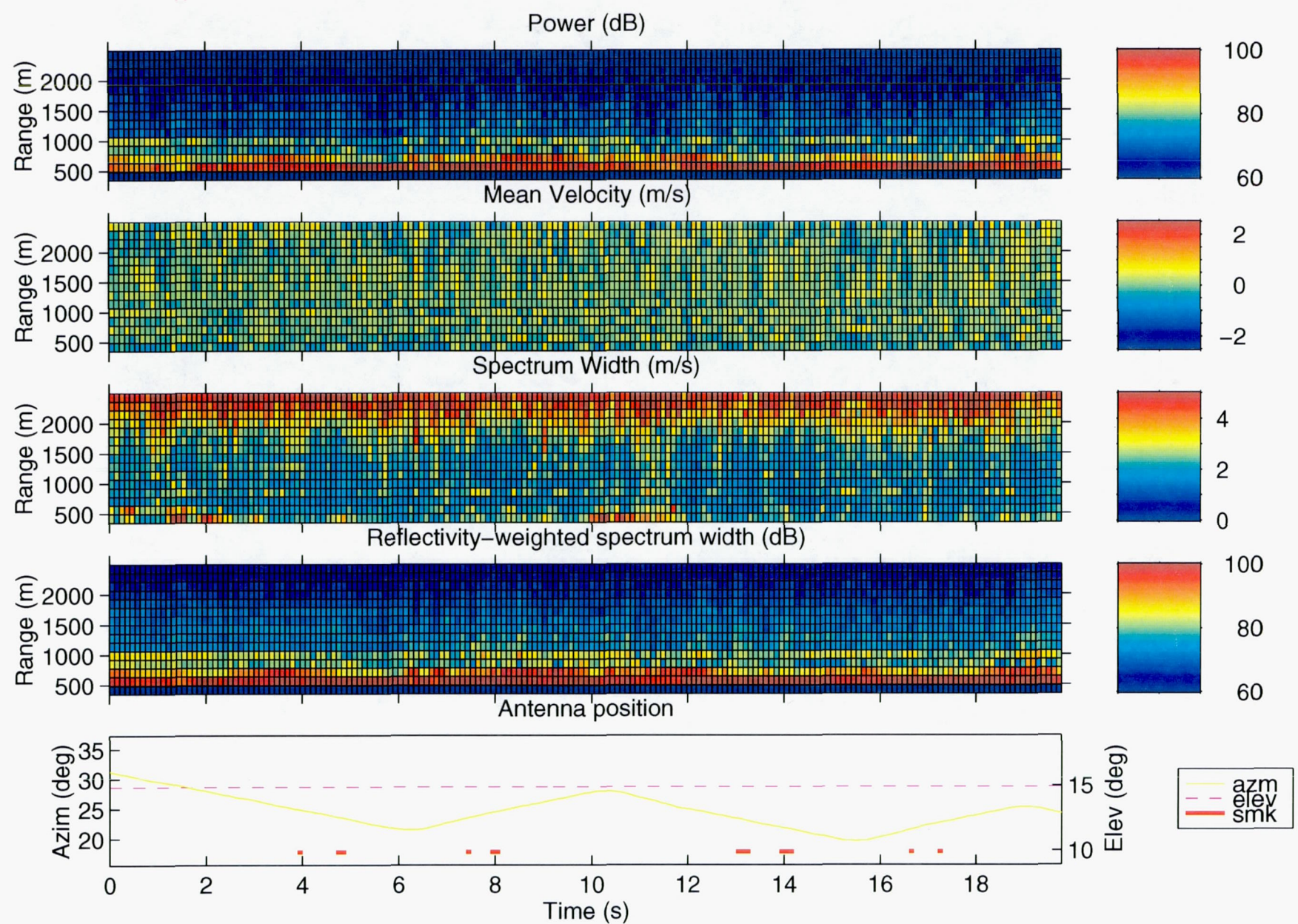


Figure A-21. Pass 122, start time: 17:21:45.

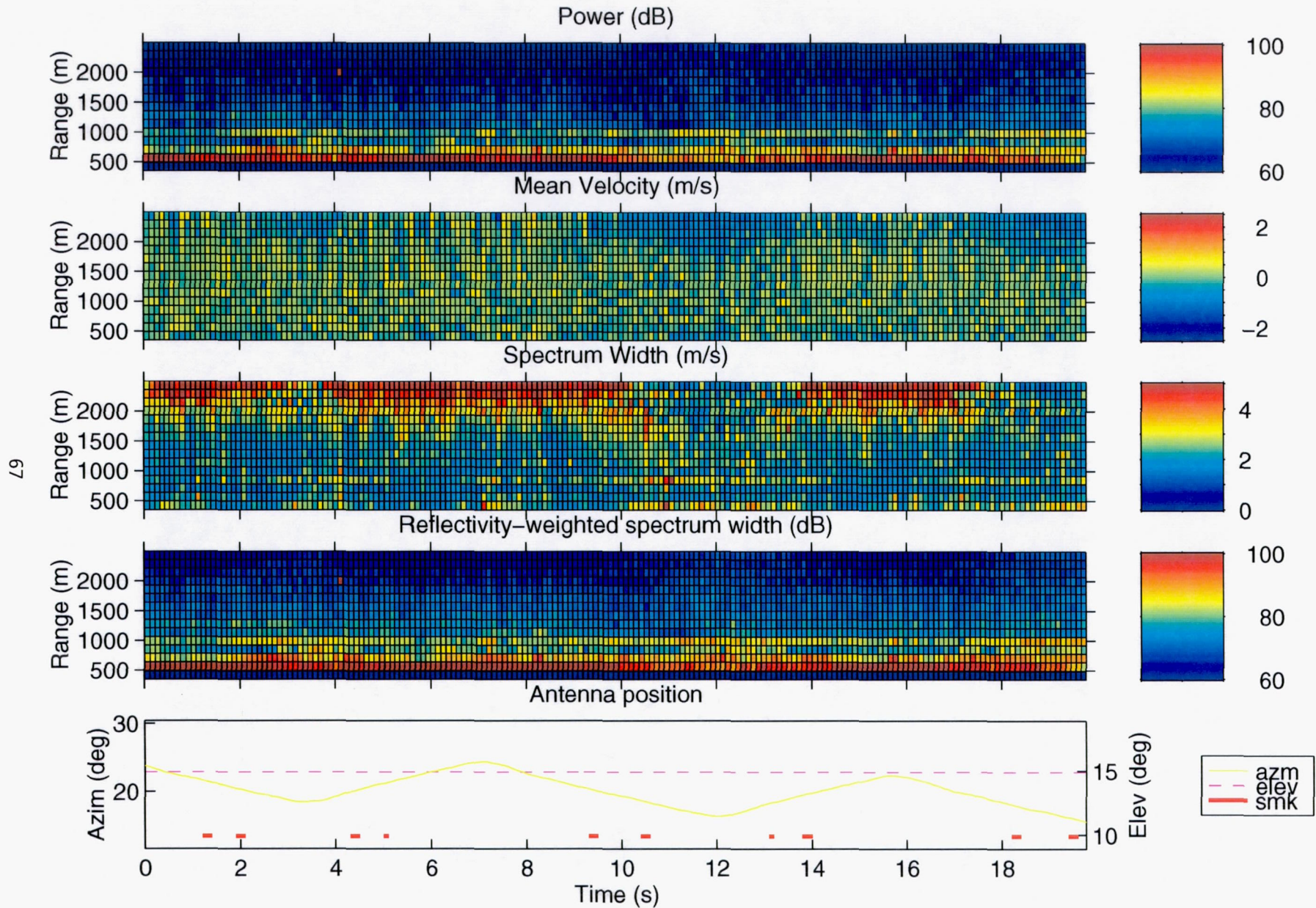


Figure A-22. Pass 122, start time: 17:22:05.

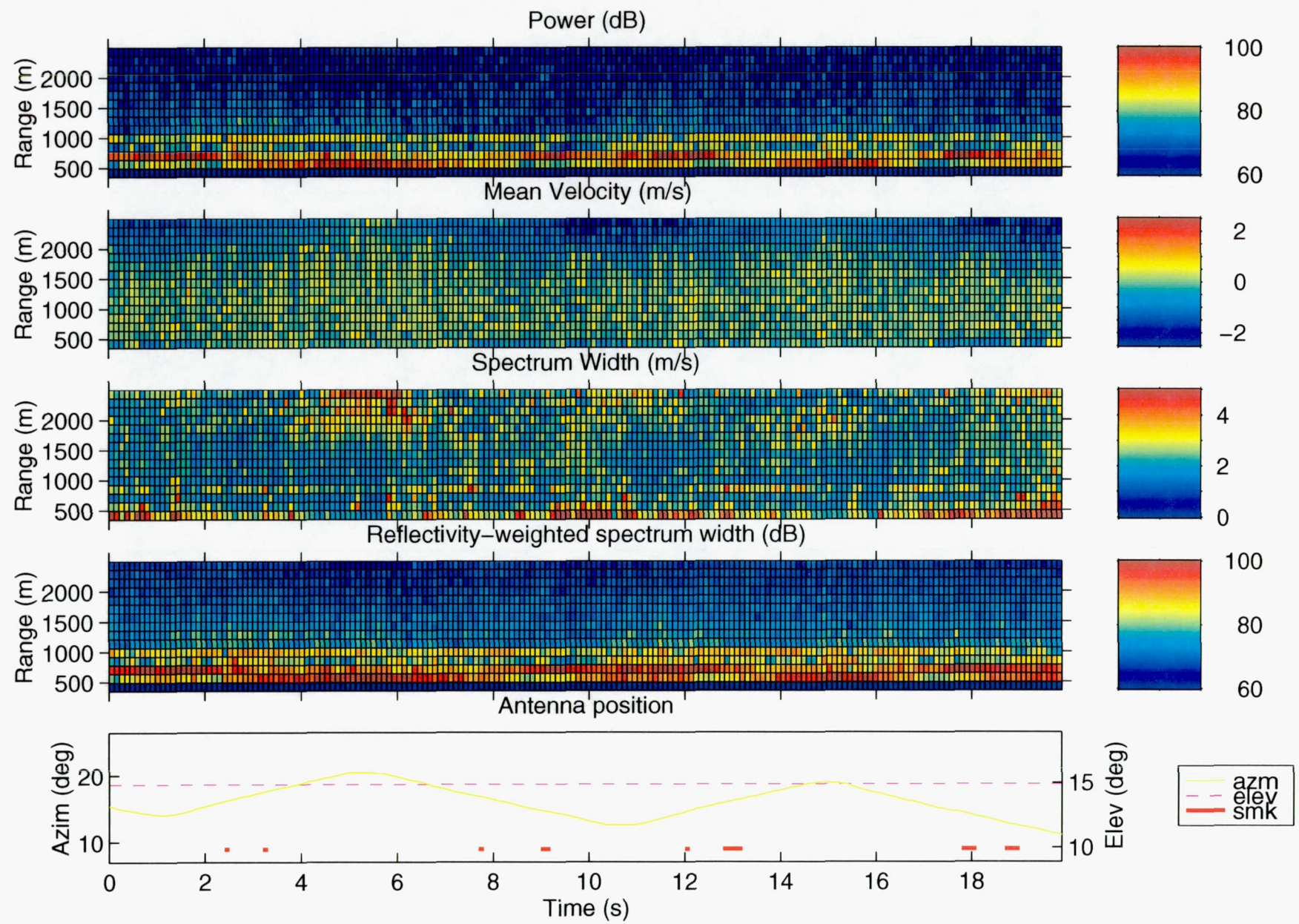


Figure A-23. Pass 122, start time: 17:22:25.

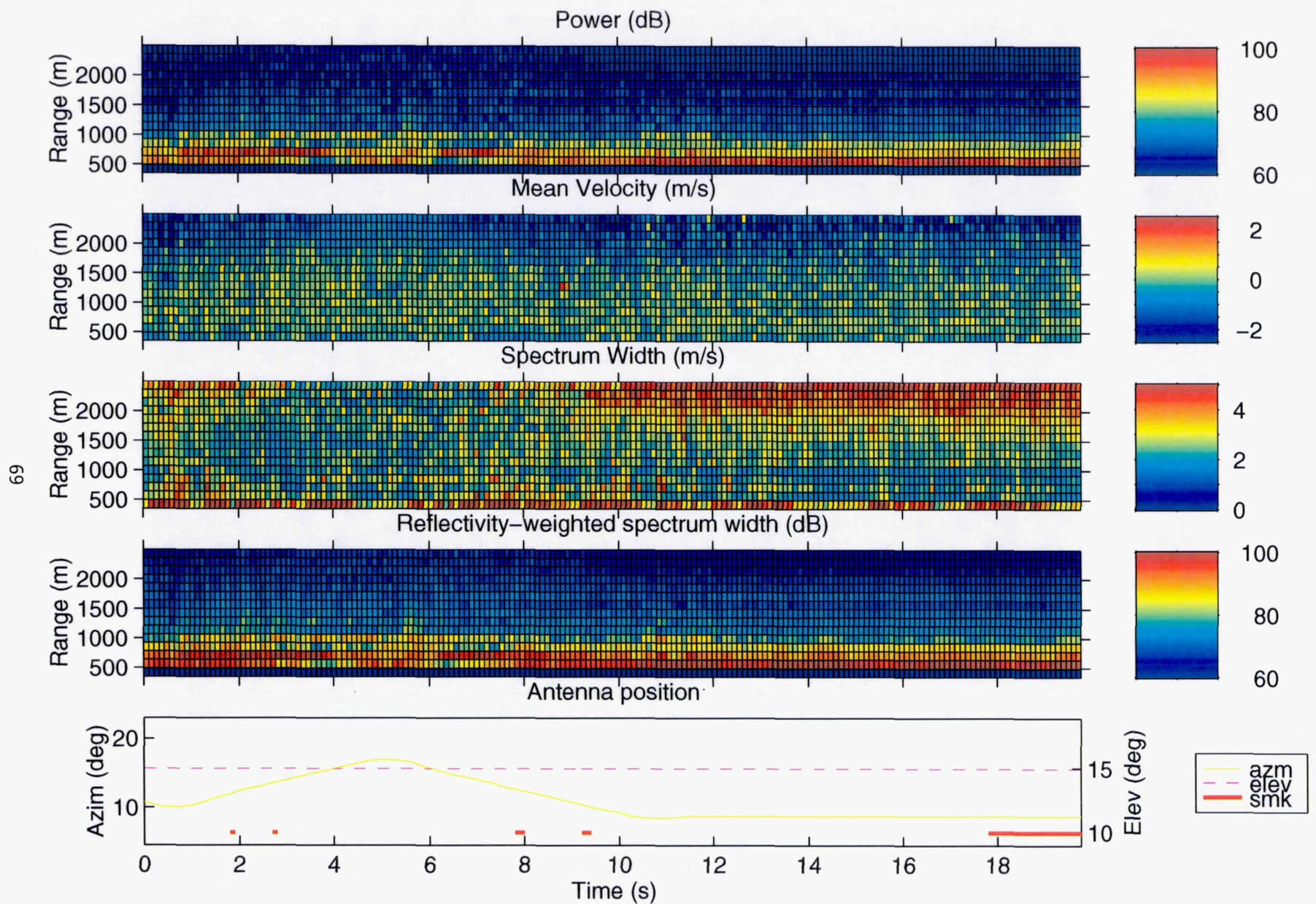


Figure A-24. Pass 122, start time: 17:22:45.

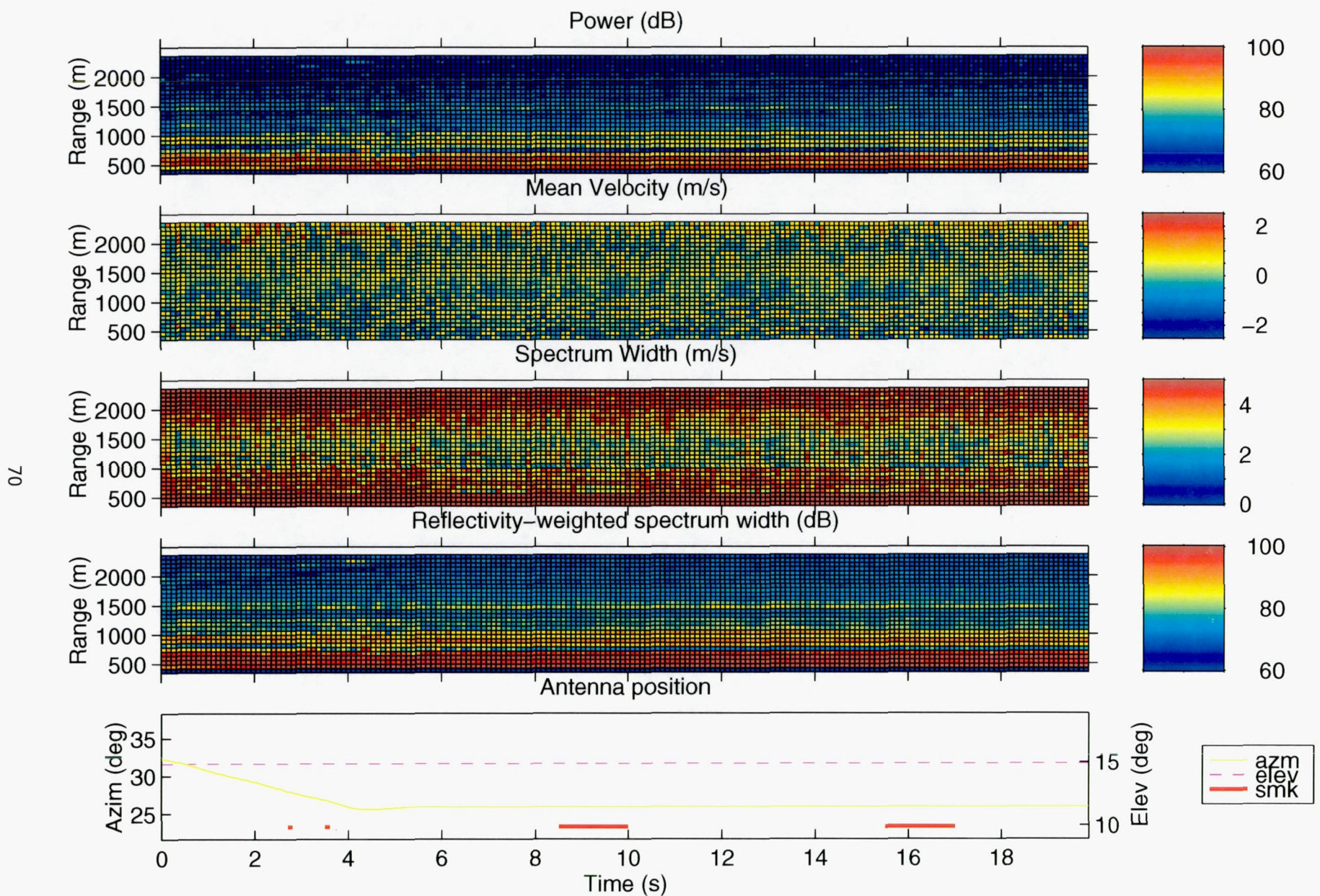


Figure A-25. Pass 124, start time: 17:33:40.

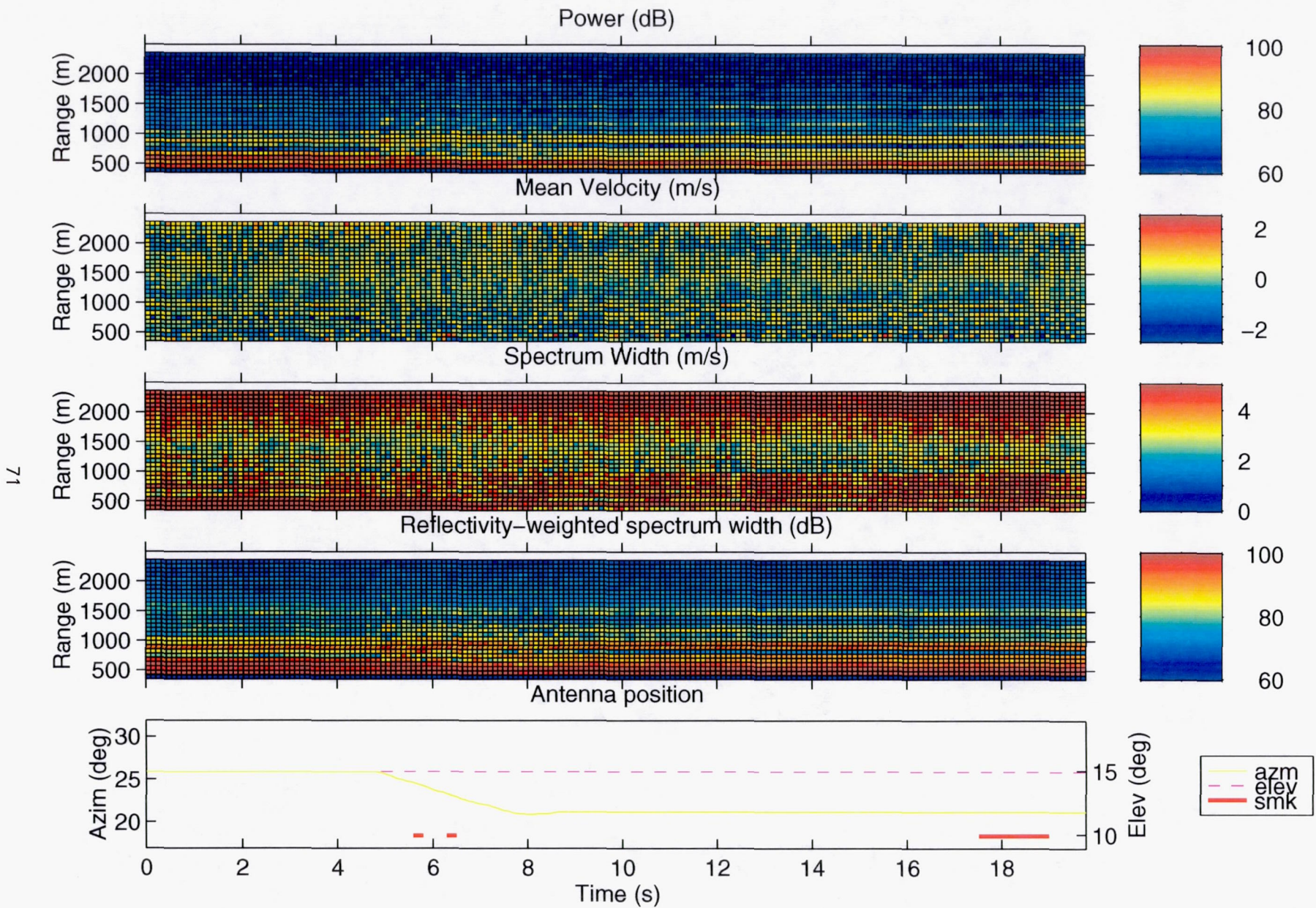


Figure A-26. Pass 124, start time: 17:34:00.

72

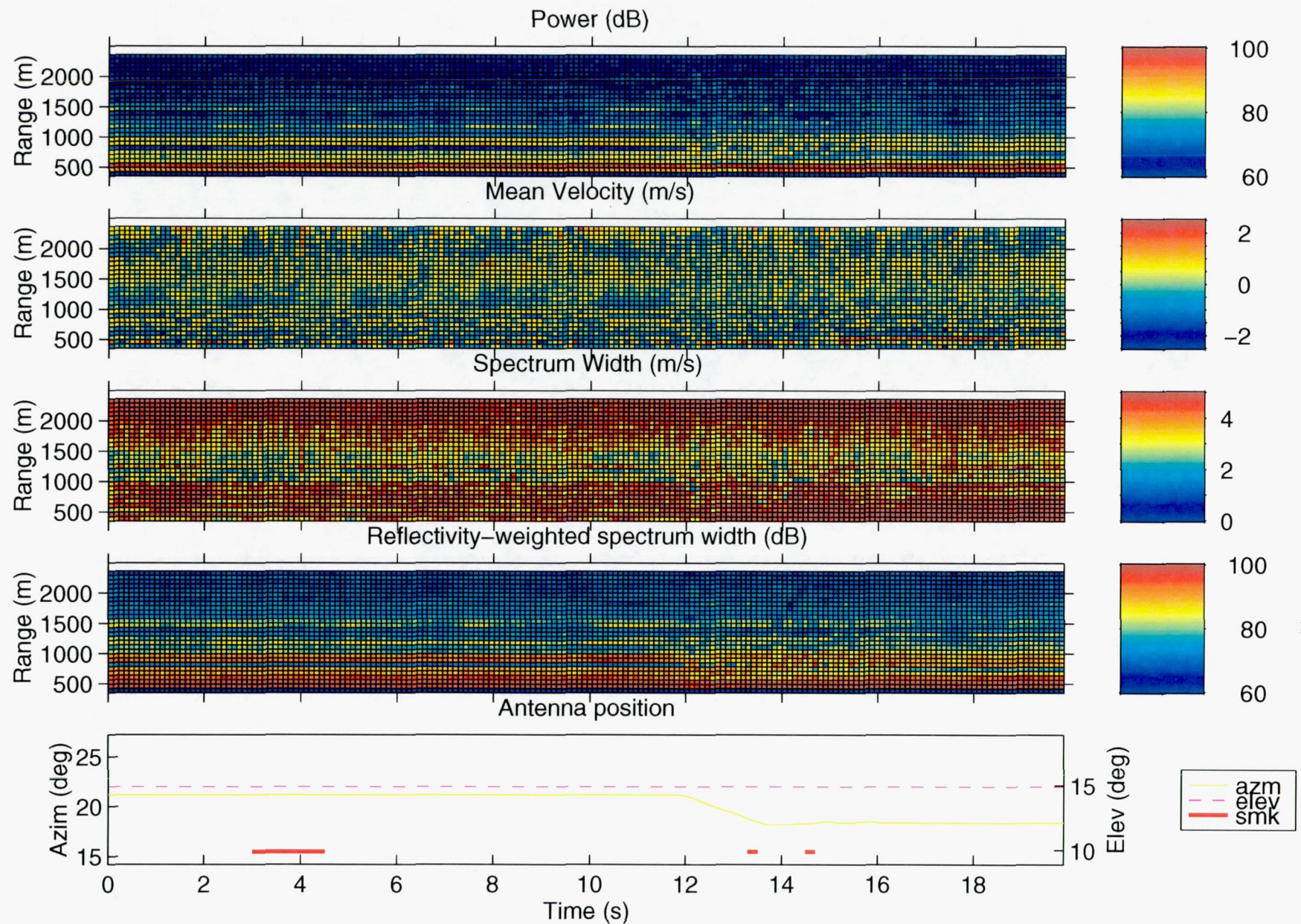


Figure A-27. Pass 124, start time: 17:34:20.

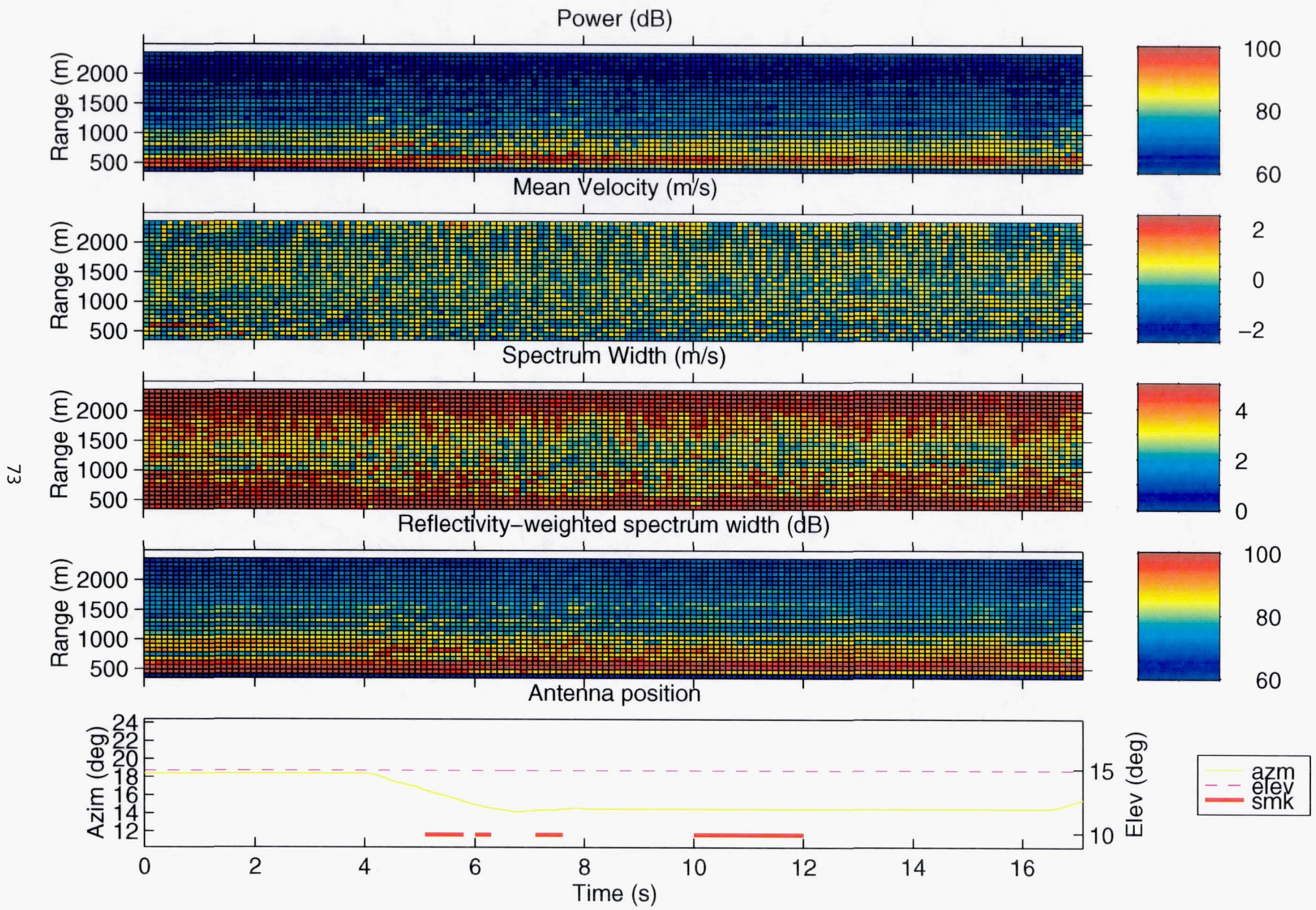


Figure A-28. Pass 124, start time: 17:34:40.

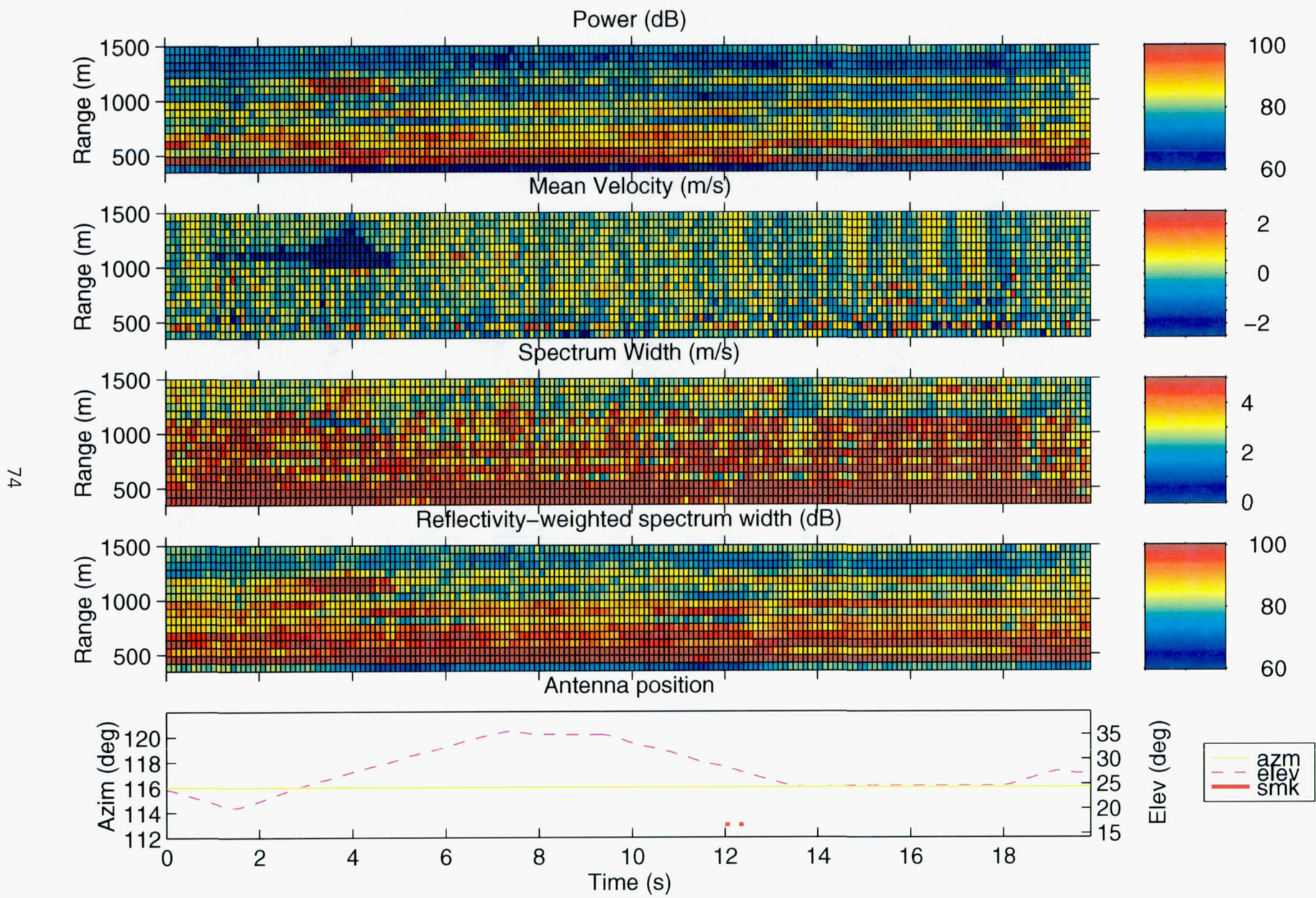


Figure A-29. Pass 135, start time: 18:55:50.

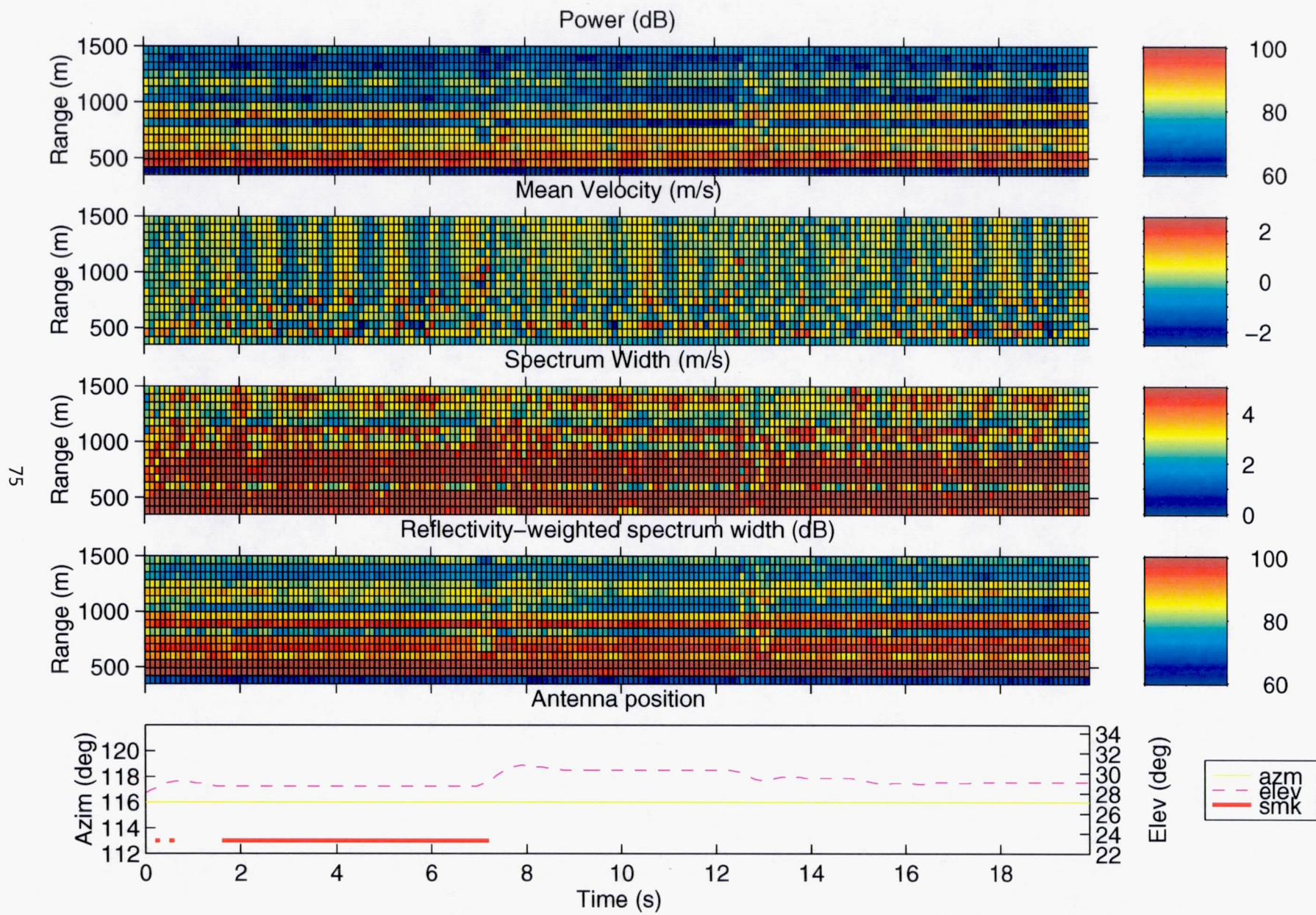


Figure A-30. Pass 135, start time: 18:56:10.

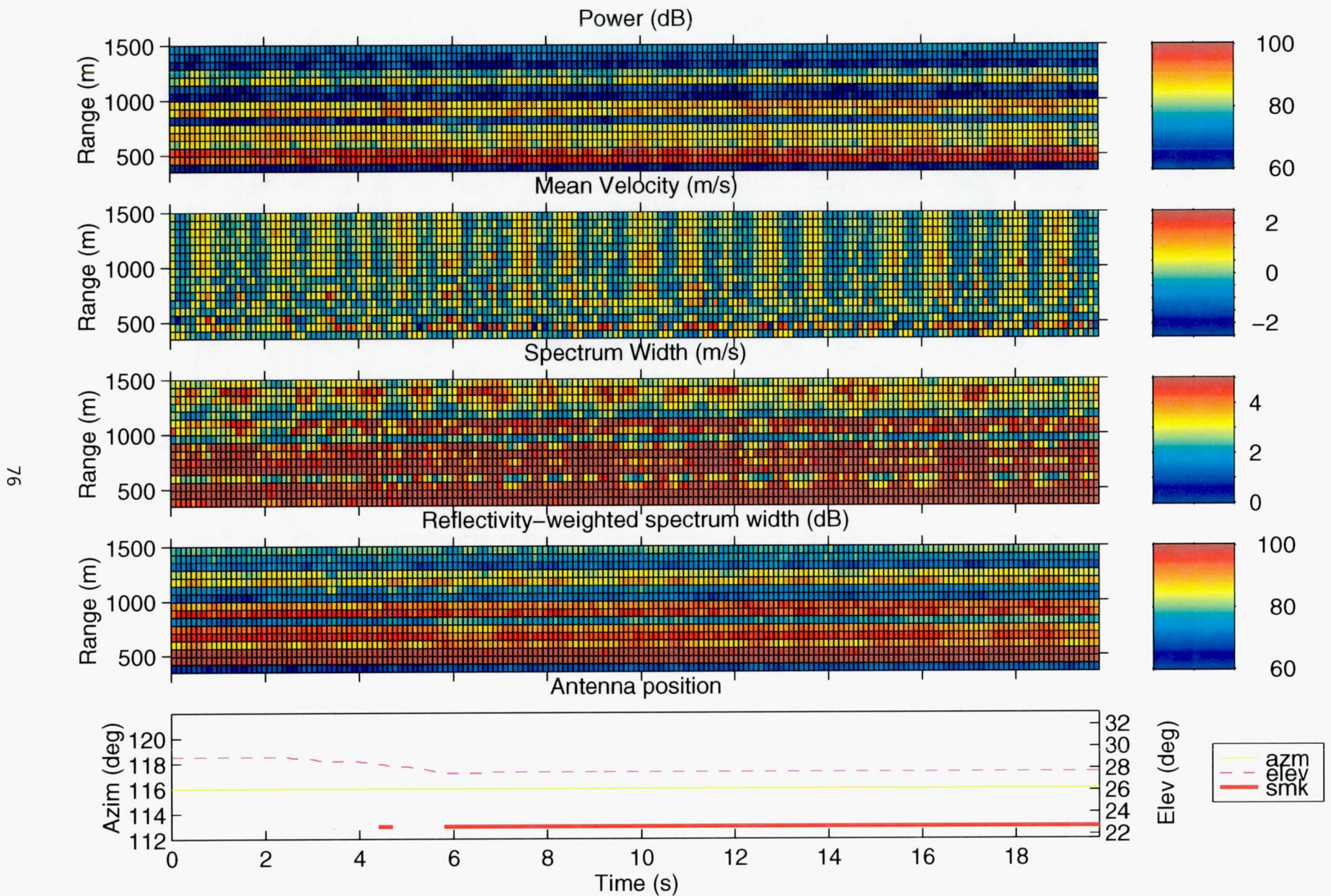


Figure A-31. Pass 135, start time: 18:56:30.

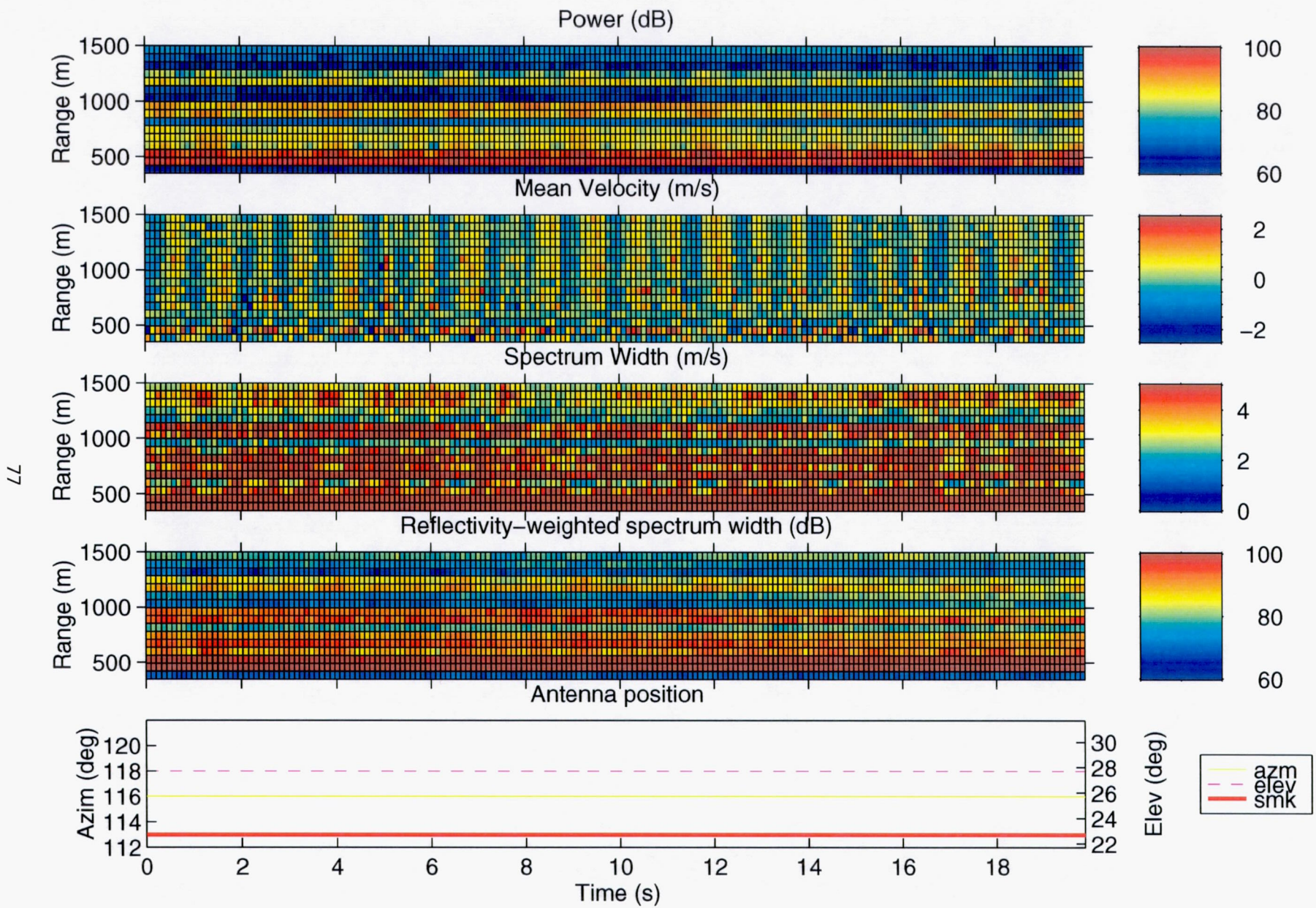


Figure A-32. Pass 135, start time: 18:56:50.

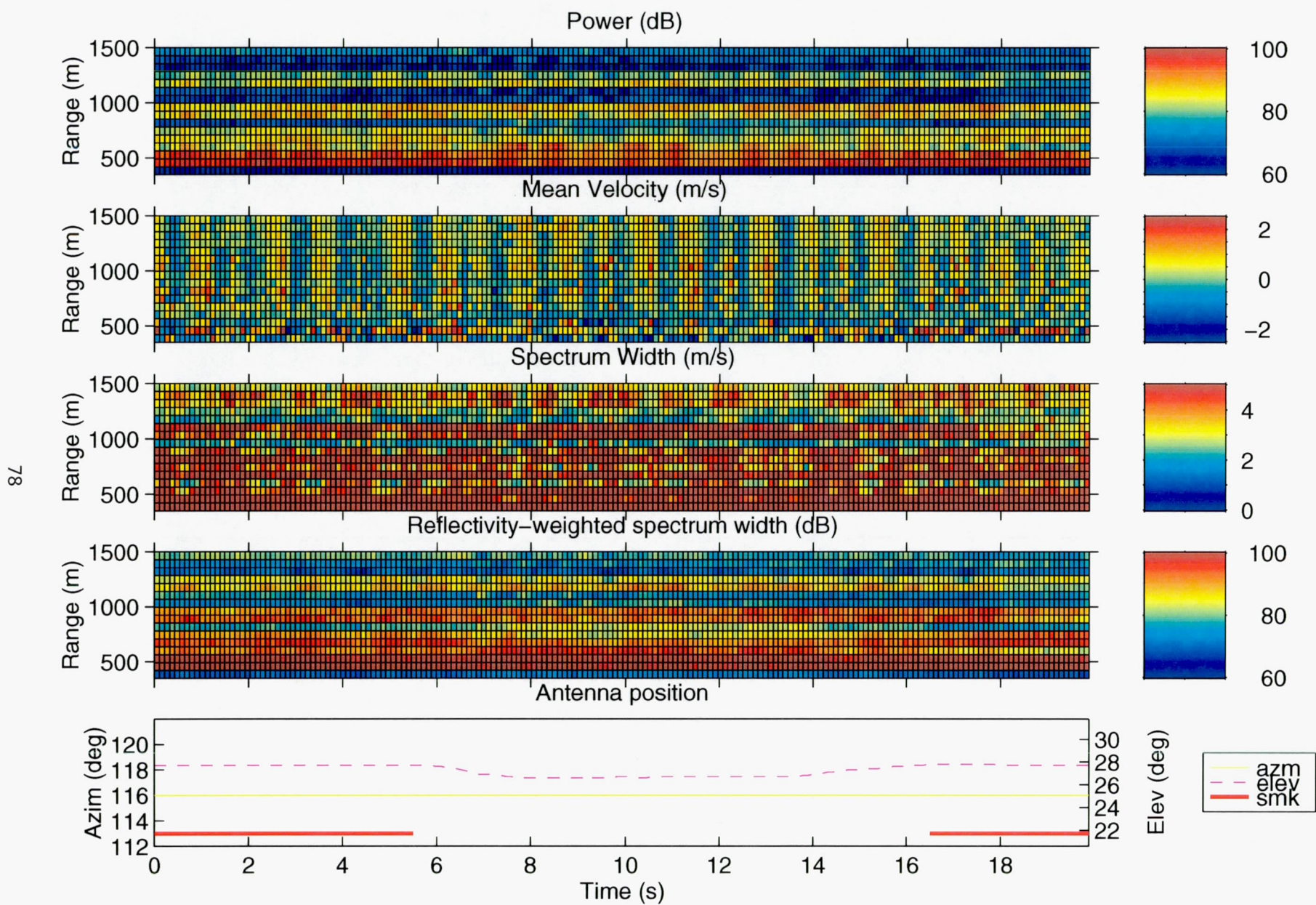


Figure A-33. Pass 135, start time: 18:57:10.

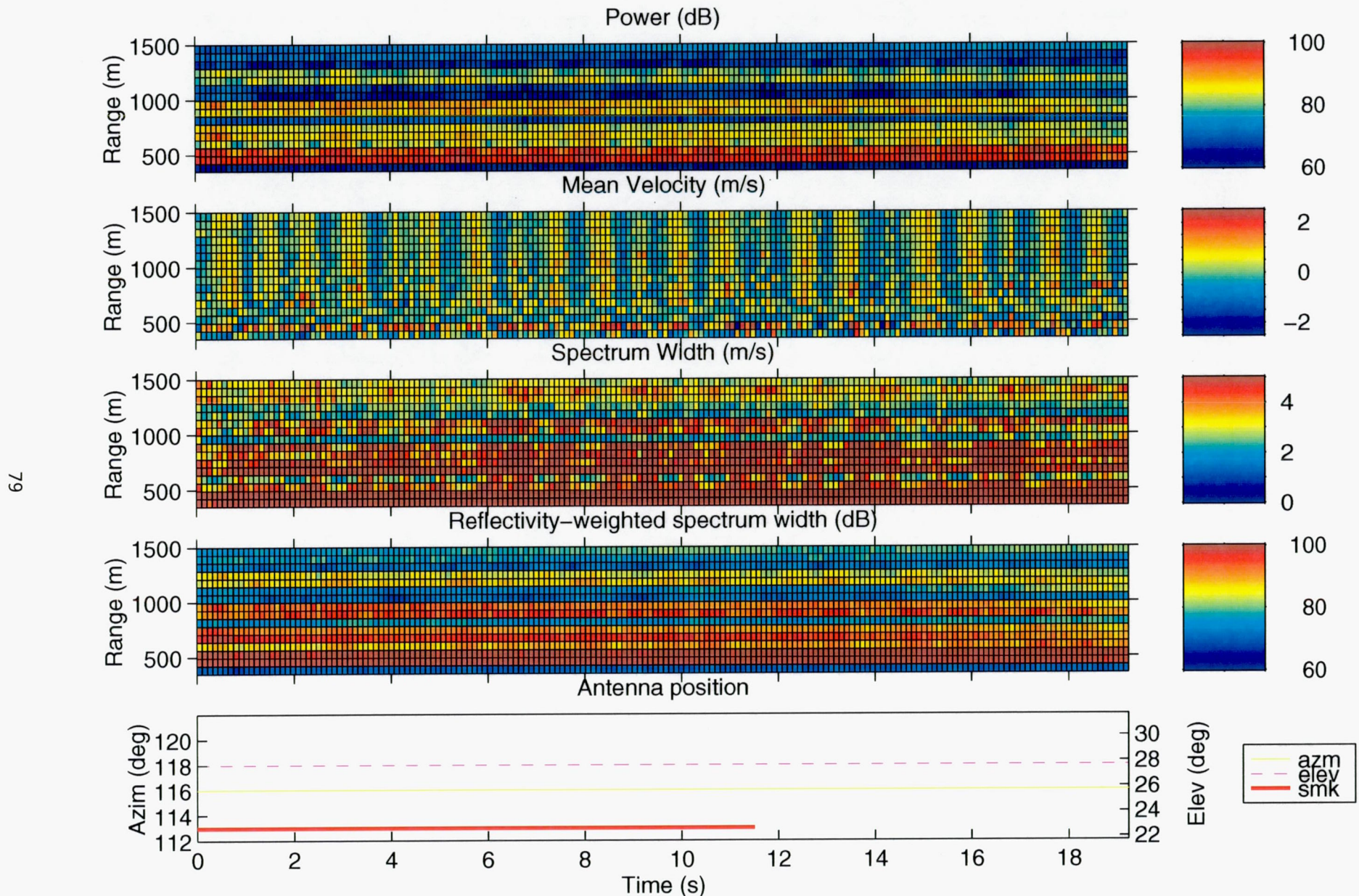


Figure A-34. Pass 135, start time: 18:57:30.

REPORT DOCUMENTATION PAGE			Form Approved OMB No. 0704-0188
<p>Public reporting burden for this collection of information is estimated to average 1 hour per response, including the time for reviewing instructions, searching existing data sources, gathering and maintaining the data needed, and completing and reviewing the collection of information. Send comments regarding this burden estimate or any other aspect of this collection of information, including suggestions for reducing this burden, to Washington Headquarters Services, Directorate for Information Operations and Reports, 1215 Jefferson Davis Highway, Suite 1204, Arlington, VA 22202-4302, and to the Office of Management and Budget, Paperwork Reduction Project (0704-0188), Washington, DC 20503.</p>			
1. AGENCY USE ONLY (Leave blank)	2. REPORT DATE	3. REPORT TYPE AND DATES COVERED	
	December 1997	Contractor Report	
4. TITLE AND SUBTITLE	Three-Centimeter Doppler Radar Observations of Wingtip-Generated Wake Vortices in Clear Air		5. FUNDING NUMBERS
6. AUTHOR(S)	Robert E. Marshall, Ashok Mudukutore, Vicki L. H. Wissel, and Theodore Myers		C NAS1-18925 TA 55 WU 538-04-11-15
7. PERFORMING ORGANIZATION NAME(S) AND ADDRESS(ES)	Center for Aerospace Technology, Research Triangle Institute, Hampton, VA Virginia Polytechnic Institute and State University, Blacksburg, VA		8. PERFORMING ORGANIZATION REPORT NUMBER
9. SPONSORING/MONITORING AGENCY NAME(S) AND ADDRESS(ES)	National Aeronautics and Space Administration NASA Langley Research Center Hampton, VA 23681-2199		10. SPONSORING/MONITORING AGENCY REPORT NUMBER
11. SUPPLEMENTARY NOTES	Langley Contract Monitor: Anne I. Mackenzie, Langley Technical Task Monitor: Robert T. Neece		
12a. DISTRIBUTION/AVAILABILITY STATEMENT	Unclassified-Unlimited Subject Category 33 Distribution: Standard Availability: NASA CASI (301) 621-0390		12b. DISTRIBUTION CODE
13. ABSTRACT (Maximum 200 words)	<p>This report documents a high risk, high pay-off experiment with the objective of detecting, for the first time, the presence of aircraft wake vortices in clear air using X-band Doppler radar. Field experiments were conducted in January 1995 at the Wallops Flight Facility (WFF) to demonstrate the capability of the 9.33 GHz ($\lambda=3$ cm) radar, which was assembled using an existing nine-meter parabolic antenna reflector at WFF and the receiver/transmitter from the NASA Airborne Windshear Radar Program. A C-130 aircraft, equipped with wingtip smoke generators, created visually marked wake vortices, which were recorded by video cameras. A C-band radar also observed the wake vortices during detection attempts with the X-band radar. Rawinsonde data was used to calculate vertical soundings of wake vortex decay time, cross aircraft bearing wind speed, and water vapor mixing ratio for aircraft passes over the radar measurement range. This experiment was a pathfinder in predicting, in real time, the location and persistence of C-130 vortices, and in setting the flight path of the aircraft to optimize X-band radar measurement of the wake vortex core in real time. This experiment was conducted in support of the NASA Aircraft Vortex Spacing System (AVOSS).</p>		
14. SUBJECT TERMS	Wake Vortex, Wake Vortices, Doppler Radar, Radar Meteorology, Aircraft Safety, Terminal Area Productivity, AVOSS, X-Band Radar		15. NUMBER OF PAGES 90
17. SECURITY CLASSIFICATION OF REPORT	18. SECURITY CLASSIFICATION OF THIS PAGE	19. SECURITY CLASSIFICATION OF ABSTRACT	16. PRICE CODE A05
Unclassified	Unclassified	Unclassified	20. LIMITATION OF ABSTRACT